Machine-induced background of the ATLAS, CMS and FASER experiments

Helena Lefebvre

Department of Physics
Royal Holloway, University of London

A thesis submitted to the University of London for the degree of Doctor of Philosophy

March 6, 2023

Declaration

I confirm that the work presented in this thesis is my own. Where information has been derived from other sources, I confirm that this has been indicated in the document.

Signed: 

Date: 6.3.2023

Abstract

The Large Hadron Collider (LHC) at CERN is the largest particle accelerator currently operating, achieving proton-proton collisions with a centre-of-mass energy of 13.6 TeV. The ATLAS experiment, one of the general-purpose detectors at the LHC along with the CMS experiment, undertakes a broad physics program including Higgs boson studies, dark matter searches and Beyond Standard Model (BSM) searches. The FASER experiment, located 480 m downstream of ATLAS, uses a compact detector to search for evidence of BSM, light and weakly-interacting particles produced at the ATLAS interaction point. In 2026, the LHC will be upgraded to the High Luminosity LHC (HL-LHC), a project aimed at increasing the instantaneous collision rate at the existing LHC interaction points up to fivefold compared to the nominal value. The upgrade is expected to increase the currently available dataset collected by the LHC experiments by one order of magnitude by 2038. The increase in luminosity and the related structural and optics changes will affect the background radiation levels in the particle experiments region, causing an increase in the statistical background for physics analyses and detector occupancy. The growth of background levels must be estimated to quantify the impact on the performance of these LHC experiments. Monte Carlo techniques are used to simulate the propagation of accelerator-induced background radiation to the sensitive areas of the experiments. Studies are performed using the BDSIM simulation software. Beam halo and beam-gas background levels are scored at the ATLAS interface plane, a virtual plane forming the interface between the accelerator and detector simulations, and evaluated for the HL-LHC settings. Comparisons with previous settings, as well as with the CMS detector, are shown. The FASER studies aim to characterise particle propagation and evaluate the fluences in the detector region. A study of systematic uncertainties in the propagation model is also presented.

Acknowledgements

This thesis marks the end of my five years as a doctoral student at RHUL. It was a tremendous and fulfilling opportunity, from taking accelerator courses at RHUL and Oxford, and attending many workshops and conferences, to working at CERN, the largest accelerator laboratory in the world. Many people helped me along the way to become a better scientist, and I owe them a big thanks.

First, I would like to thank my supervisor, Stephen Gibson, who took me on as a student and welcomed me to the high energy accelerator society. His guidance and support throughout the years have been invaluable. His optimistic and encouraging approach to any challenge has inspired me throughout my PhD journey.

Furthermore, none of this work would be possible without the help and guidance from Laurie Nevay. He introduced me to BDSIM and welcomed me at CERN. He helped me with every aspect of my work, from improving my presentation skills, answering technical and general questions every day and challenging all my results.

I would also like to thank my colleagues from RHUL and CERN. My colleague and friend Stuart Walker for teaching me everything about the non-collision background and challenging me in squash matches. I am grateful for the weekly meetings at RHUL, which gave me new ideas and often helped me when I encountered technical and thesis issues. A big thank you to Helmut Burkhart for guiding me around the beam background groups at CERN. The LBS meetings were an excellent place for discussion and suggestions for additional studies to be performed. I am grateful to Bjorn Lindstrom and Veronica Olsen for their help with SixTrack simulations and enriching work discussions.

Finally, I want to thank my parents, Lenka and Pavel and my sister Monika for their unconditional support throughout and beyond my studies. I thank my husband Benoit for supporting me through everything, moving countries with me many times and always believing in me.

Contents

List of Figures

List of Tables

1 Introduction

1.1 Motivation

An accelerator is a device capable of propelling charged particles at high speeds to keep them in well-defined beams and deliver them to a collision point for various purposes, such as industrial and medical applications and fundamental research. Charged particles (e.g. electrons or protons) are accelerated by electric fields while being steered by magnetic fields in order to reach the target parameters desired by the specific user. This work focuses on particles in synchrotrons - accelerators where particles travel along the same circular path for many turns, specifically the LHC and its successor, the HL-LHC. Other types of high energy physics accelerators not discussed in this thesis include linear accelerators, cyclotrons and others. The LHC is currently the largest and most powerful particle accelerator in the world and the HL-LHC is its future upgrade. They are designed to collide protons in order to study the fundamental laws governing the interactions and forces among elementary particles. The HE-LHC is a studied upgrade of the HL-LHC, possibly doubling the beam energy. However, accelerated particles do not always follow the nominal path. Many are lost inside the machine due to accelerator design, beam conditions and operation settings. This process is called beam-induced background (BIB). These lost particles can potentially cause issues such as fake exotic physics signatures and increased detector occupancy. Some BIB can originate near the experimental sites and create showers of particles entering the particle detectors.

This work refines simulation efforts of the beam background study to understand and quantify the effects of background on the machine and detector of the LHC. We use a Beam Delivery Simulation (BDSIM) model, described in Chapter 2, to calculate the background rates for the HL-LHC, updating earlier background studies with the most up-to-date accelerator parameters [1], and comparing to previous versions. Most of the

HL-LHC design is completed, and an overview study of the beam-induced background must be performed to check the expected background levels. However, a few components intended to protect the machine are still not manufactured, and their design could change based on how they affect the background. The detailed geometry is then applied to build a model of a particle transfer between the ATLAS collision point and the FASER experiment.

Chapter 1 presents an overview of basic accelerator concepts and real-life examples relevant to this thesis and reviews the experimental sites at these machines. Beam-induced backgrounds, one of the main topics of this thesis, are introduced. Chapter 2 presents the software tools used for this work, provides a detailed description of the geometry model preparation and gives an overview of the simulation setup. Chapter 3 focuses on accelerator backgrounds reaching the ATLAS detector [2]. The background radiation simulation results are analysed at a simulated plane just in front of the detector that forms the interface between the accelerator and detector simulations. The work presented here is an updated version of previous machine-induced background studies [3] with updated and more accurate accelerator settings, which will be used in real runs. Chapter 4 examines the accelerator background reaching the CMS detector and compares it to the ATLAS detector simulation results for the HL-LHC era. Chapter 5 expands on Chapter 3 and analyses the effects of beam background inside the ATLAS detector. Chapter 6 presents the FASER experiment and shows the particle propagation model between the ATLAS collision point and the FASER detector and also the model used for evaluating the effects of accelerator background from the LHC on FASER. FASER is a new project, and this work has been part of the simulation preparation since the early design stages [4], providing estimates of particle fluences at the detector. Chapter 7 concludes this thesis.

1.2 Accelerator principles

The first particle accelerators built in the 1930s were intended for research in nuclear physics [5]. Since then, accelerators have evolved and are used in multiple applications. Accelerators are used in particle physics for studies of the characteristics of elementary particles. Particle physics accelerators demand the highest energy per particle of all accelerating machines built up to the present time and include the accelerator used in this thesis, the LHC. Other applications include: synchrotron radiation sources for a wide variety of applications of ultraviolet [6], and x-ray beams in materials science [7]; accelerators

for medical applications from x-ray sources to hadron beam radiation therapy [8]; nuclear physics research studying nuclear energy levels and quark-gluon plasma [9], and electron linacs used for oil and natural gas exploration in flue gas treatment [10]. All of these use some accelerator technology and are concerned about beam quality, focusing and stability, which will be discussed in detail in this section.

1.2.1 Types of accelerators

Conventional accelerating machines use a combination of radio-frequency (RF) cavities for acceleration and electromagnets for bending and focusing. Other technologies are used for novel types of accelerators such as plasma and wakefield accelerators, which are not presented here.

Electrostatic accelerators propel charged particles to high energy by subjecting them to a static high voltage potential difference. Two main types of electrostatic accelerators are used for nuclear research: the Van de Graaff generator [11], and the Cockcroft-Walton accelerator [12]. The maximum beam energy produced by these accelerators is a few megavolts, which is limited by electrical insulation breakdown.

Linear accelerators increase the kinetic energy of charged particles using a series of oscillating electric potentials. There are various types going from a cathode ray tube producing few keV electrons [13] to the 3 km long Stanford Linear Accelerator that was capable of accelerating electrons to energies of 50 GeV [14] until its shutdown in 2006.

A betatron uses the change in the magnetic field to accelerate electrons in a circular path inside a cylindrical vacuum chamber [15]. Betatrons were used in particle physics experiments providing up to 300 MeV energy electrons. However, they are limited by the magnetic field strength and the size of the magnet.

Cyclotrons accelerate charged particles outwards from the centre of a cylindrical vacuum chamber along a spiral path created by a static magnetic field and accelerated by a varying electric field [16]. They are still used in nuclear research, radioisotope production and particle therapy. The largest still used cyclotron is the RIKEN Superconducting Ring Cyclotron in Japan with a diameter of 18 m and accelerating heavy ions at energies of up to 400 MeV/u [17].

A synchrocyclotron is a type of cyclotron for which the frequency of the electric field is varied to compensate for relativistic effects [18]. The Synchro-Cyclotron at European Organization for Nuclear Research (CERN) was the largest machine (operational from

1957 to 1990) with circumference of 15.7 m and achieved 600 MeV proton acceleration [19].

Synchrotrons accelerate particles in cyclic paths on a fixed closed-loop path [20]. The magnetic field bending the particles is synchronized to the increasing kinetic energy of the particles by increasing the frequency of the applied electric field. In synchrotrons, different accelerator sections are divided by their purpose - accelerating, bending, cleaning, and other manipulations. Synchrotrons are used in high energy physics research but also in life sciences, particle therapy, material analysis and other applications. The largest synchrotron is the LHC with a circumference of 27 km and accelerating protons up to the design energy of 7 TeV [21].

1.2.2 Longitudinal dynamics

Charged particles are accelerated by the electric force, either by an electrostatic or a time-varying electric field, using single or multiple cell accelerating structures to achieve an increase in beam energy. The structures are called electrostatic or radio-frequency electric cavities.

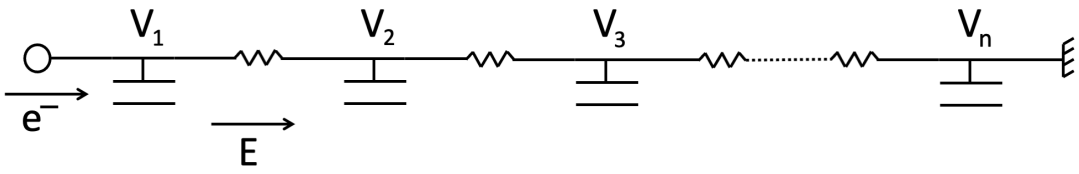

Figure 1.1: Principle of an electrostatic accelerator. An electron (e^-) passes through a series of cells. The electric field (E) propels the electron in the gaps between conductor tubes to which constant voltage (V) is applied.

As shown in Figure 1.1, electrostatic accelerators apply a constant voltage across a gap between which the particles are accelerated. Energy gain (W) is proportional to the voltage of the generator (V_{gen}):

$$W = q \sum V_n = n\, q\, V_{\mathrm{gen}} \tag{1.1}$$

where q is the charge of the accelerated particles and n is the number of accelerating electrodes. The breakdown voltage of the system limits the maximum energy gain.

In radio-frequency acceleration, shown in Figure 1.2, charged particles traverse a

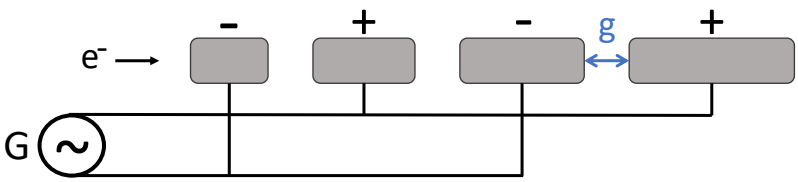

Figure 1.2: Principle of a drift tube linac with a generator G and gap length g. The electrons (e^-) are accelerated by electric field between conductor tubes. During the passage through each tube, the tube's polarity changes in order to provide positive force on the particle in the gap.

series of accelerating regions driven by a voltage source. The voltage changes its sign during the time the particle is inside a cylindrical drift tube so that the particle always feels a positive force in the gaps (g) between conductors. The length of the drift tube increases throughout the machine as the velocity of the particle increases due to the acceleration, while the length of the gap stays the same to remain synchronised with a constant applied frequency. RF fields allow for an arbitrary number of accelerating steps in gaps and electrodes fed by an RF generator. The electric field generates sinusoidal alternating half-periods of acceleration and deceleration. Assuming an electric field in the middle of a gap:

$$E_z = E_0 \cos(\omega_{\mathrm{RF}} t + \phi_S), \tag{1.2}$$

where E_0 is the maximum amplitude of the electric field, ω_{RF} is the angular frequency of the RF generator and ϕ_S is the phase of arrival of the ideal particle (the "synchronous" phase), the energy is:

$$W = q \int E_z dz = q \int_{-g/2}^{g/2} E_0 \cos(\omega_{\mathrm{RF}} \frac{z}{v} + \phi_S) dz \tag{1.3}$$

and the energy gain becomes:

$$\Delta W = qV \frac{\sin(\omega g/2v)}{\omega g/2v} = qVT, \tag{1.4}$$

where T is the transit time factor (the length of a cavity required to secure a constant electric field throughout a passage, $T = \frac{\sin(\omega g/2v)}{\omega g/2v}$) with v the velocity of the traversing

particle.

Synchrotrons can reuse a single accelerating structure by synchronising the electric field with the circulating frequency of the beam. To this day, accelerators reaching the largest beam energies are synchrotrons. The LHC uses 8 RF cavities per beam, each providing an accelerating field of 5 MV/m at 400 MHz, giving an energy gain of 16 MeV per passing (approximately 1.8×10^5 MeV/s) [22]. For the LHC, it takes about 30 s to increase the energy from 450 GeV (injection energy) to 7 TeV (collision energy). However, it takes about 20 min to ramp up the magnetic field of the superconducting magnets, which limits the acceleration time.

It is relatively easy for a single particle in an accelerator to achieve the optimal trajectory and desired energy gain. However, accelerators must deal with a large number of particles to provide valuable or statistically significant results. Particles surrounding the optimal path can vary slightly in location or momentum. The size of this variation depends on the window in which the oscillating field propels them forward. These particles are contained in "bunches". Inside an accelerating cavity, particles that arrive earlier experience a smaller accelerating field and slow down. Similarly, particles arriving late will be accelerated more. This mechanism provides a restoring force, which keeps particles oscillating around a stable phase.

In synchrotrons, particles travel around a circular orbit, and the revolution frequency ($f = v/r$) depends on the particle's momentum. Taking the logarithmic derivation of f, the change in frequency is:

$$\frac{df}{f} = \frac{dv}{v} - \frac{dr}{r}, \tag{1.5}$$

where $\frac{dv}{v}$ represents the change in velocity and $\frac{dr}{r}$ represents the change in orbit radius. After introducing the momentum compaction factor $\alpha_c = \frac{dr/r}{dp/p}$, the frequency shift becomes:

$$\frac{df}{f} = \frac{dv}{v} - \alpha_c \frac{dp}{p}. \tag{1.6}$$

If we apply the equations of the theory of relativity, the frequency change can be expressed as:

$$\frac{df}{f} = \left(\frac{1}{\gamma^2} - \alpha_c\right) \frac{dp}{p}. \tag{1.7}$$

For particles with low momentum ($\frac{1}{\gamma^2} > \alpha_c$), the revolution frequency increases as momentum increases, while for particles with high momentum ($\frac{1}{\gamma^2} < \alpha_c$), the revolution frequency decreases with momentum. The special case of $\frac{1}{\gamma^2} = \alpha_c$ is called the transition (and $\gamma = \frac{1}{\sqrt{\alpha_c}}$ is the transition energy).

In summary, particles that arrive earlier at an accelerating cavity experience a smaller accelerating field and slow down, while particles arriving late will be accelerated more. The restoring force which keeps particles oscillating around a stable phase is called the synchronous phase ϕ_S.

Particles passing through the cavity at the same phase ϕ_S are called "synchronous particles". Each synchronous particle has the nominal energy and follows the nominal trajectory. These particles are uniformly spaced around the circumference.

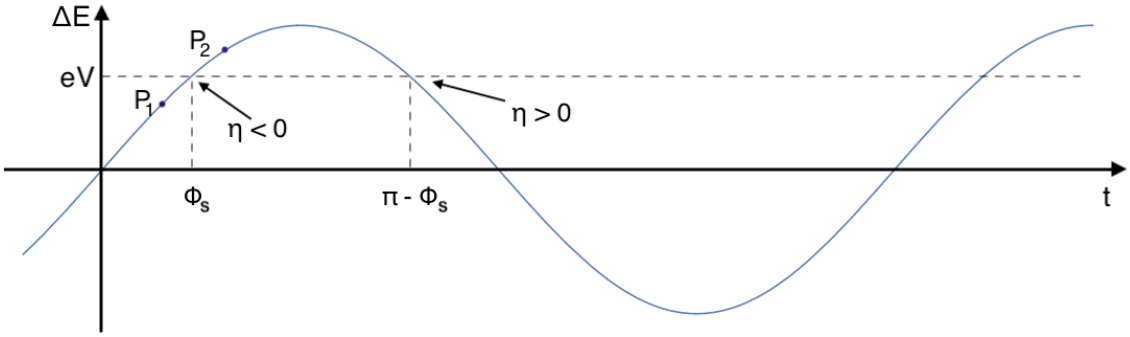

Figure 1.3: Phase stability diagram for a particle in a synchrotron showing the different energy gain for particles with different phases (ϕ). eV is the energy gain of the synchronous particle and η is the slip factor.

A diagram of the phase stability is shown in Fig. 1.3. A particle arriving early (P_1) will get a lower energy kick, while a particle arriving late (P_2) will get a higher energy kick. Above transition, energy growth is followed by a lower revolution frequency. A particle delayed with respect to the synchronous one will get closer to it, and phase stability occurs at $\pi - \phi_S$. The slip factor η is the relative change in revolution frequency f for a particle with non-ideal momentum ($\Delta f/f = \eta \Delta p/p$). The energy gain per turn with respect to the energy gain of the synchronous particle is:

$$(\Delta E)_{\text{turn}} = eV(\sin\phi - \sin\phi_S). \tag{1.8}$$

In the longitudinal phase space shown in Fig. 1.4, the motion is described by distorted circles in the vicinity of the ϕ_S (stable fixed point). The motion is unbounded in the phase

variable for phases beyond $\pi - \phi_S$ (unstable fixed point). The curve passing through $\pi - \phi_S$ is called the separatrix and encloses the area called a bucket.

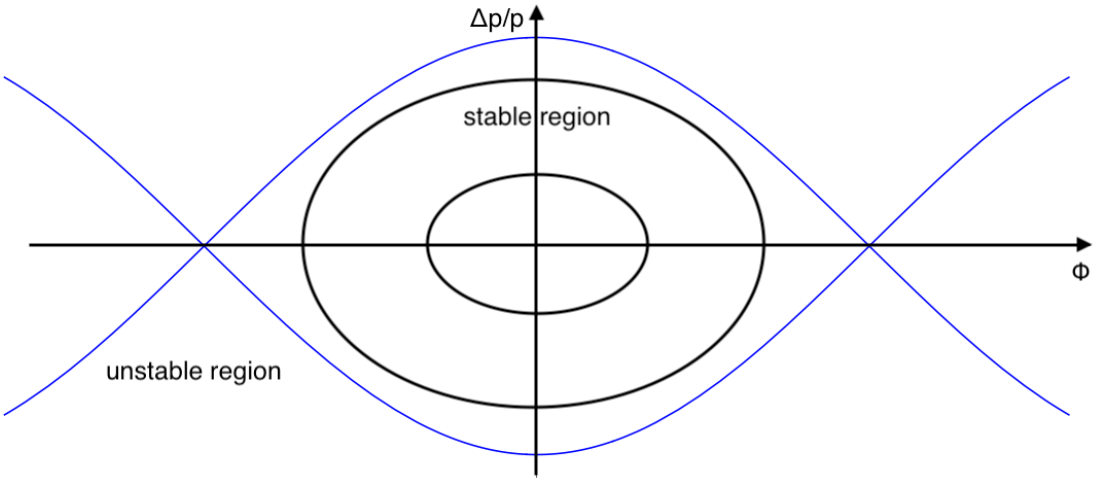

Figure 1.4: Phase space diagram for a synchrotron without acceleration. Stable particles inside the separatrix move on ellipses in the longitudinal phase space. Particles in the unstable region (outside the separatrix) are ejected from the bunch.

1.2.3 Transverse dynamics

In synchrotrons, particles must also be bent in the transverse plane in order to follow a circular orbit. The bending is achieved by using magnetic fields. The force acting on a charged particle in a pure magnetic field is given by the Lorentz force:

$$\vec{F} = q\vec{v} \times \vec{B}, \tag{1.9}$$

where $\vec{v}$ is the particle's velocity and $\vec{B}$ is the magnetic field. In the presence of a perpendicular magnetic field, the force becomes:

$$F = q|\vec{v} \times \vec{B}| = q\frac{ds}{dt}B, \tag{1.10}$$

where $\frac{ds}{dt}$ is the change in path length ds in time dt.
Using the diagram in Figure 1.5, the change in momentum ($\vec{p}$) can be expressed as:

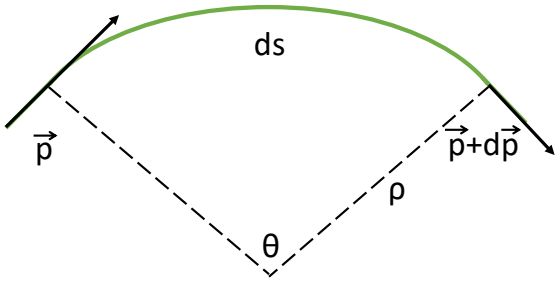

Figure 1.5: Vector diagram showing differential changes in momentum $\vec{p}$ for a particle trajectory ds.

$$\begin{aligned} \frac{d\vec{p}}{dt} &= |\vec{p}|\frac{d\theta}{dt} \\ &= p\frac{d\theta}{ds}\frac{ds}{dt} \\ &= \frac{p}{\rho}\frac{ds}{dt}. \end{aligned} \tag{1.11}$$

Using eq. 1.10 and 1.11, we obtain:

$$\begin{aligned} q\frac{ds}{dt}B &= \frac{p}{\rho}\frac{ds}{dt} \\ B\rho &= \frac{p}{q} \end{aligned} \tag{1.12}$$

The quantity $B\rho$ is called the magnetic rigidity and measures how hard it is to bend particles of a certain momentum.

The bending dipole magnets are placed symmetrically about the arc of the particle's path (Figure 1.6). The bending angle in a dipole magnet is (assuming $\theta \ll \pi/2$):

$$\sin(\theta/2) = \frac{BL}{2(B\rho)} \rightarrow \theta \approx \frac{BL}{p/q}. \tag{1.13}$$

Dipole magnets also provide weak focusing in the vertical direction. For this type of focusing, a component of the magnetic field in the horizontal plane which decreases with distance from the centre of the magnet is required:

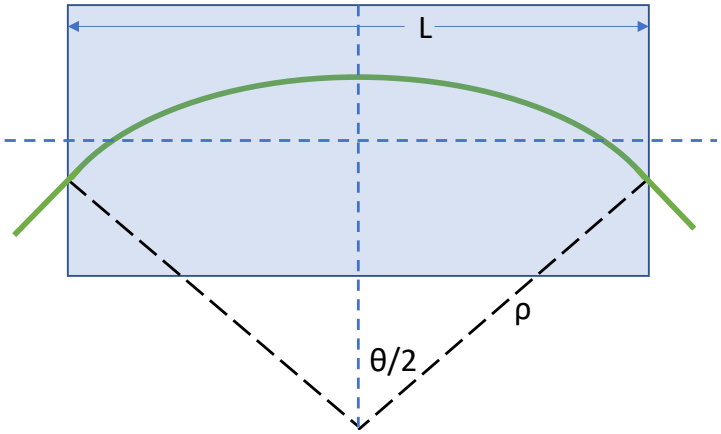

Figure 1.6: The geometry of a particle trajectory in a dipole magnet of length L (magnet outlined in blue).

$$\frac{\delta B_x}{\delta z} = \frac{\delta B_z}{\delta r} < 0. \tag{1.14}$$

The principal focusing in synchrotrons comes from quadrupole magnets. Figure 1.7 shows the fields and forces inside a quadrupole. The field is zero on the axis of the quadrupole, and its strength rises linearly with distance from the axis. The strength of the quadrupole is characterised by its gradient ($\frac{dB_z}{dx}$) normalised with respect to the magnetic rigidity:

$$k = \frac{1}{B\rho}\frac{dB_z}{dx}. \tag{1.15}$$

The angular deflection given to a particle passing through a short quadrupole of length l and strength k at a displacement x is, therefore:

$$\Delta x' = \theta = \frac{lB}{B\rho} = \frac{l(dB_y/dy)x}{B\rho} = lkx. \tag{1.16}$$

This type of quadrupole focuses particles in the horizontal plane but deflects particles with a vertical displacement away from the axis. For vertical focusing, the quadrupole should be rotated by 90°.

For the basic operation of circular accelerators, the dipoles providing bending and weak focusing and quadrupoles providing strong focusing are sufficient to keep beam par-

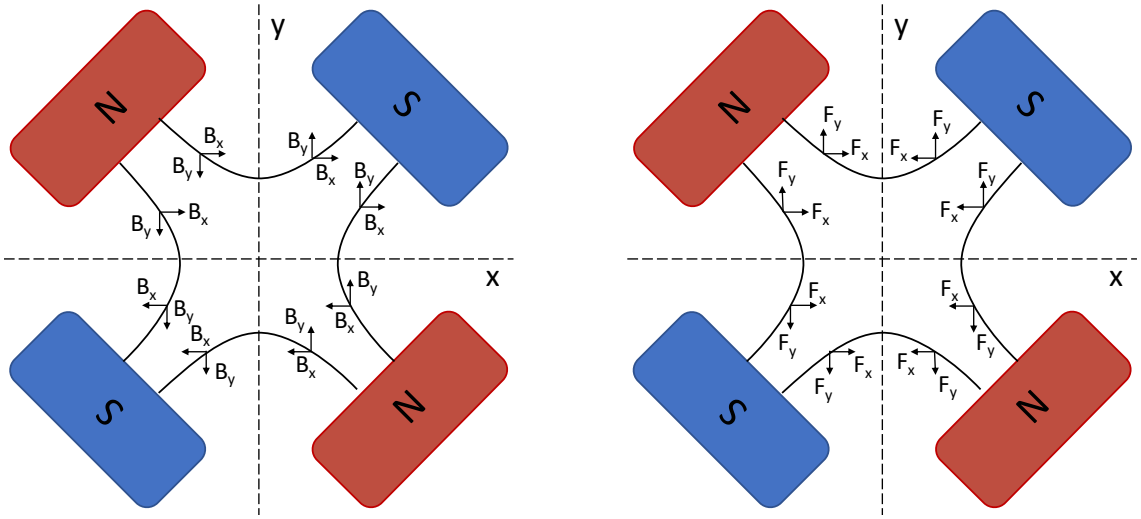

Figure 1.7: Components of the magnetic field (left) and magnetic force (right) in a quadrupole. North poles are shown in red, south poles are blue.

ticles inside the machine. Using the conditions that these concepts supply, we can look at the equation of motion for a single particle. The Hamiltonian for particle motion in an electromagnetic field represented by vector potential $\vec{A}$ and scalar potential V is:

$$H = eV + c\left[m^2c^2 + (\vec{p} - e\vec{A})^2\right]^{1/2}, \tag{1.17}$$

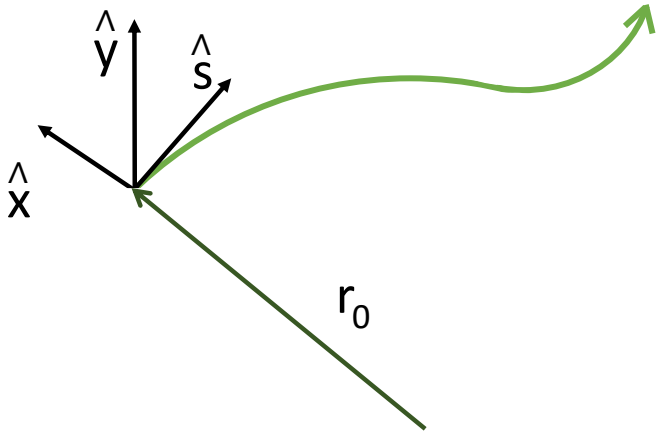

Figure 1.8: Frenet-Serret coordinate system ($\hat{x}$,$\hat{y}$,$\hat{s}$) at one point of a particle trajectory.

where $\vec{p}$ is the canonical momentum and the magnetic field is given by $\vec{B} = \nabla \times \vec{A}$ and the electric field is defined as $\vec{E} = -\nabla V - \frac{\delta \vec{A}}{\delta t}$. Using the Frenet-Serret coordinate system shown in Figure 1.8 with

$$\begin{aligned}\hat{s}(s) &= \frac{d\vec{r_0}(s)}{ds} \\ \hat{x}(s) &= -\rho(s)\frac{d\hat{s}(s)}{ds} \\ \hat{y}(s) &= \hat{x}(s) \times \hat{s}(s),\end{aligned} \tag{1.18}$$

we obtain the Hamiltonian:

$$H = e\phi + c\left[m^2c^2 + \frac{(p_s - eA_s)^2}{(1+x/\rho)^2} + (p_x - eA_x)^2 + (p_y - eA_y)^2\right]^{1/2}. \tag{1.19}$$

If we change the independent variable from t to s, the new conjugate phase space variables are (x,p_x; y,p_y;t,-H) and the new Hamiltonian is:

$$\tilde{H} = -(1+x/\rho)\left[\frac{(H-e\phi)^2}{c^2} - m^2c^2 - (p_x - eA_x)^2 - (p_y - eA_y)^2\right]^{1/2} - eA_s. \tag{1.20}$$

Expanding the Hamiltonian to second order in p_x and p_y and using the total energy $E = h - e\rho$ and the total momentum $p = \sqrt{E^2/c^2 - m^2c^2}$:

$$\tilde{H} \approx -p(1+x/\rho) + \frac{1+x/\rho}{2p}\left[(p_x - eA_x)^2 + (p_y - eA_y)^2\right]^{1/2} - eA_s. \tag{1.21}$$

The Hamilton's equations of motion are

$$\begin{aligned} x' &= \frac{\delta\tilde{H}}{\delta p_x} & p_x' &= -\frac{\delta\tilde{H}}{\delta x} \\ y' &= \frac{\delta\tilde{H}}{\delta p_y} & p_y' &= -\frac{\delta\tilde{H}}{\delta y}. \end{aligned} \tag{1.22}$$

With transverse magnetic field $\vec{B} = B_x(x,y)\hat{x} + B_y(x,y)\hat{y}$, the magnetic field components are:

$$B_x = -\frac{1}{1+x/\rho}\frac{\delta A_s}{\delta y} \qquad B_y = -\frac{1}{1+x/\rho}\frac{\delta A_s}{\delta x}. \tag{1.23}$$

If we neglect higher order terms, the betatron equations of motion become:

$$\begin{aligned} x'' - \frac{\rho + x}{\rho^2} &= \frac{B_y}{B\rho}\frac{p_0}{p}(1 + x/\rho)^2 \\ y'' &= -\frac{B_x}{B\rho}\frac{p_0}{p}(1 + x/\rho)^2. \end{aligned} \tag{1.24}$$

Applying the transverse magnetic field components and using $K_1 = \frac{1}{B\rho}\frac{\delta B_1}{\delta x}$:

$$\begin{aligned} x'' + K_x(s)x = 0 \qquad & K_x = 1/\rho^2 - K_1(s) \\ y'' + K_y(s)y = 0 \qquad & K_y = K_1(s). \end{aligned} \tag{1.25}$$

Since we ignored higher order terms, the solution to the Hamiltonian is the second-order linear ordinary differential equations (Hill's equations), the equations of transverse motion of the particles in a synchrotron:

$$\frac{d^2x}{ds^2} + k_x(s)x = 0 \qquad \frac{d^2y}{ds^2} + k_y(s)y = 0, \tag{1.26}$$

where k changes along the path and $B_1(s) = \delta B_y/\delta x$, $k_x(s) = 1/\rho^2 - \frac{B_1(s)}{B\rho}$ and $k_y(s) = \frac{B_1(s)}{B\rho}$.

The solution to the Hill's equation is:

$$x = \sqrt{\beta(s)\epsilon}\cos(\phi(s) + \phi_0), \tag{1.27}$$

where $\beta(s)$ is the betatron function, ϵ is the emittance and $\phi(s)$ is the phase advance.

1.2.4 Lattice design

The lattice design is one of the most crucial steps in the accelerator design. A basic lattice has a pattern of bending and focusing magnets. The lattice determines the magnet strengths and length and affects all other systems in the synchrotron.

A typical storage ring uses the basic FODO lattice structure, which consists of a focusing quadrupole magnet (F) followed by a defocusing quadrupole magnet (D), then another dipole focusing magnet (Figure 1.9). Any other elements without focusing properties (O) can be placed between the quadrupoles.

Taking the solution of Hill's equation (1.27), there is a constant amplitude component $\sqrt{\epsilon}$ and another amplitude component $\sqrt{\beta(s)}$ the function ϕ is called the phase advance.

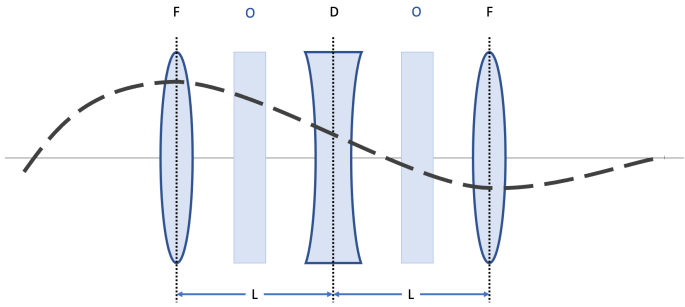

Figure 1.9: A basic FODO magnetic lattice. The focusing (F) and defocusing (D) lenses are separated by a distance L. In between (O) are any other structures, such as drift spaces, RF cavities or even bending magnets under special circumstances, that do not have focusing properties.

Both functions of s must have the same periodicity as the lattice and are connected by:

$$\phi' = \frac{1}{\beta} \qquad\qquad \phi = \int \frac{ds}{\beta}. \tag{1.28}$$

Differentiating the solution from eq. 1.27, the divergence of x is:

$$x' = -\sqrt{\frac{\epsilon}{\beta(s)}}\sin(\phi(s)+\phi_0) + \frac{\beta'(s)}{2}\sqrt{\frac{\epsilon}{\beta(s)}}\cos(\phi(s)+\phi_0). \tag{1.29}$$

The second term becomes zero when taking $\beta'(s)$ equal to zero. This defines the transverse phase space which is an ellipse, shown in Figure 1.10, with semi-axis $\sqrt{\beta\epsilon}$ in the x direction and $\sqrt{\epsilon/\beta}$ in the x' direction. The area is equal to $\pi\epsilon$, which is a constant. The parameter ϵ is called the emittance of the beam.

The lattice is a series of repetitive patterns of focusing fields in a ring (alternating-gradient machine). Each lattice element may be expressed as a matrix. Hill's equation as a linear differential equation can be defined as a 2×2 matrix in order to track particles from a point s_1 to a point s_2.

$$\begin{pmatrix} x(s_2) \\ x'(s_2) \end{pmatrix} = \begin{pmatrix} a & b \\ c & d \end{pmatrix} \begin{pmatrix} x(s_) \\ x'(s_1) \end{pmatrix} = M_{21} \begin{pmatrix} x(s_) \\ x'(s_1) \end{pmatrix}. \tag{1.30}$$

Using $w = \sqrt{\beta}$, the solution of Hill's equation becomes:

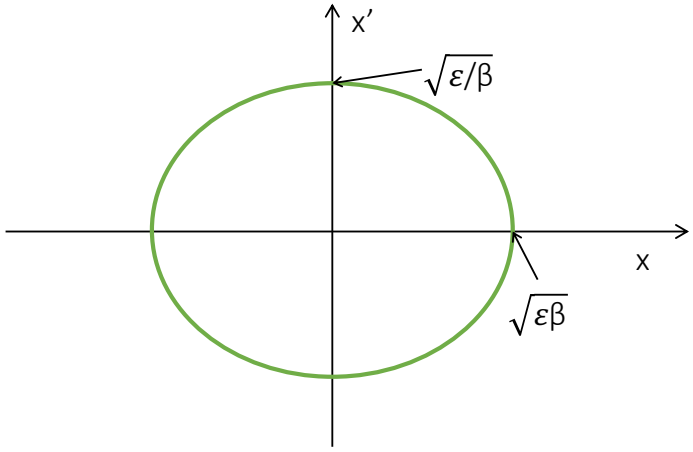

Figure 1.10: The transverse phase space of a particle circulating in a synchrotron. The area of this ellipse is $\pi\epsilon$, which is a measure of how much the particle diverges from the ideal trajectory.

$$x = \sqrt{\epsilon} w \cos(\phi(s) + \phi_0). \tag{1.31}$$

Taking the derivative and substituting $\phi' = 1/\beta = 1/w^2$:

$$x' = \sqrt{\epsilon} w' \cos(\phi(s) + \phi_0) - \frac{\sqrt{\epsilon}}{w} \sin(\phi(s) + \phi_0). \tag{1.32}$$

Substituting these into the transport matrix, we get:

$$M_{21} = \begin{pmatrix} \frac{w_2}{w_1}\cos(\phi) - w_2 w_1' \sin(\phi) & w_1 w_2 \sin(\phi) \\ -\frac{1+w_1 w_1' w_2 w_2'}{w_1 w_2}\sin(\phi) - (\frac{w_1'}{w_2} - \frac{w_2'}{w_1})\cos(\phi) & \frac{w_1}{w_2}\cos(\phi) + w_1 w_2' \sin(\phi) \end{pmatrix}. \tag{1.33}$$

If s_1 and s_2 are between two identical points in successive turns of a periodic structure, then ϕ becomes μ - the phase advance and $w_1 = w_2$ and $w_1' = w_2'$. Then the transport matrix becomes:

$$M = \begin{pmatrix} \cos(\mu) - w w' \sin(\mu) & w^2 \sin(\mu) \\ -\frac{1+w^2 w'^2}{w^2}\sin(\mu) & \cos(\mu) + w w' \sin(\mu) \end{pmatrix}. \tag{1.34}$$

Defining the parameters (known as Twiss or Courant-Snyder parameters):

$$\alpha = -ww' = -\frac{\beta'}{2} \tag{1.35}$$

$$\beta = w^2 \tag{1.36}$$

$$\gamma = \frac{1 + (ww')^2}{w^2} = \frac{1 + \alpha^2}{\beta}, \tag{1.37}$$

the transfer matrix becomes the Twiss matrix:

$$M = \begin{pmatrix} \cos(\mu) - \alpha \sin(\mu) & \beta \sin(\mu) \\ -\gamma \sin(\mu) & \cos(\mu) - \alpha \sin(\mu) \end{pmatrix} = \begin{pmatrix} a & b \\ c & d \end{pmatrix}, \tag{1.38}$$

which describes the complete turn around the machine. The Twiss matrix varies depending on the starting point s. For equivalent FODO lattices in a synchrotron, only a single cell solution is needed as the beta function and the phase advance repeat for each identical section.

Synchrotrons alternate between FODO bending sections and straight insertion sections used for beam manipulation such as accelerating, colliding, beam cleaning and others. For these insertion sections, the Twiss parameters need to be calculated individually.

1.3 Accelerators and experiments

This section introduces the accelerators and particle physics experiments relevant to this thesis: the LHC, HL-LHC, HE-LHC accelerators and the ATLAS and FASER experiments.

1.3.1 Accelerators

1.3.1.1 LHC

The LHC is the largest particle accelerator in the world, accelerating protons and ions [23]. It was built by the CERN between 1998 and 2008 in the existing Large Electron-Positron Collider (LEP) tunnel. It is a complex machine comprising many accelerator stages. It is designed to deliver a beam to a set of experiments focused on studying physics of and beyond the Standard Model (SM) at the collision energy up to the centre-of-mass energy of 14 TeV. LHC's goal is to allow physicists to test the predictions of different theories of particle physics, such as searching for new particles and resolving unanswered questions in particle physics. For instance, the LHC enabled the discovery of the Higgs boson in

2012 [24]. The LHC started operating in 2008 and provided over 180 fb^{-1} of data for each of its two major experiments, ATLAS and CMS during Run 1 and Run 2 [25], higher than the initial target value.

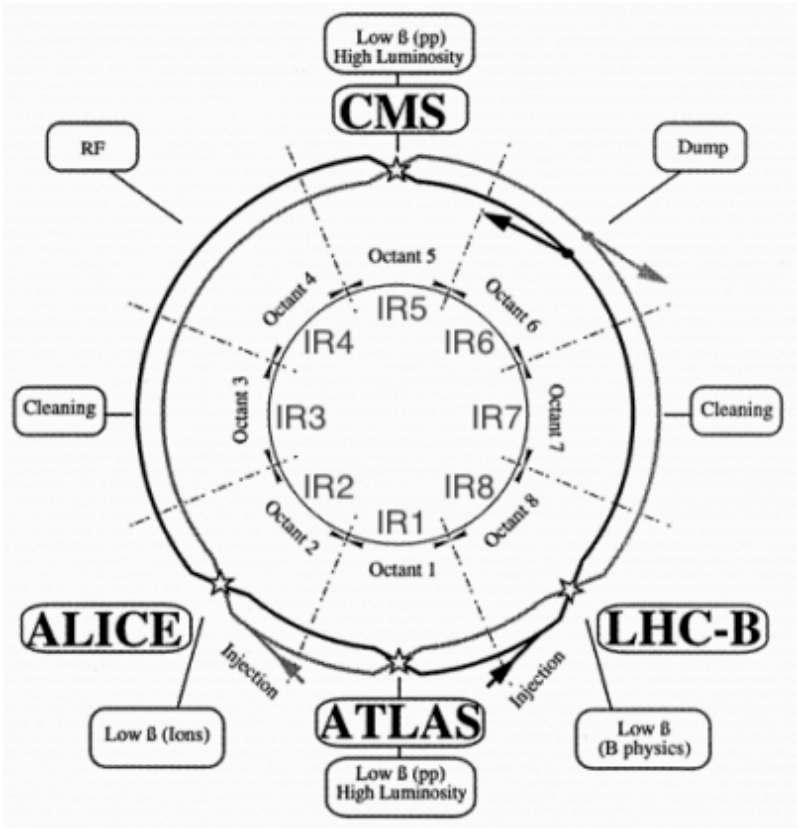

Figure 1.11: The layout of the LHC accelerator showing the different sections dedicated to experiments or beam manipulation [26].

The protons in the LHC are concentrated in bunches that circulate in opposite directions in the accelerator in a circular tunnel with a circumference of 27 km. The tunnel lies at an average of 100 m underground for shielding from cosmic ray radiation and infrastructure convenience (it would be hard to find space for such a large laboratory aboveground). A diagram of LHC's layout in Figure 1.11 shows the structure and locations of the different regions. The accelerator comprises of 8 beam manipulation straight sections and 8 arc sections. Straight sections are called insertion sections (IR) and contain specialized equipment for beam manipulation and particle detectors. The arc sections are mainly composed of bending and focusing magnets. The LHC contains 1232 dipole magnets and 392 quadrupole magnets, most of which are superconducting. At IR 2 and IR 8, the two beams (beam 1 and beam 2) are injected into the machine from the Super Proton Synchrotron

(SPS) at an energy of 450 GeV. Beam 1 travels in a clockwise direction and beam 2 in counter-clockwise when viewed from the top. In IR 4, the protons are accelerated using 8 radio-frequency cavities from 450 GeV to up to 7 TeV (nominal design energy, or less for earlier runs). Insertion sections IR 3 and IR 7 are used for beam cleaning (betatron and momentum cleaning respectively). At four interaction points (IP), in their respective insertion regions, these bunches are steered to collide (IP 1, IP 2, IP 5, IP 8). The collisions of the bunches are called bunch-crossings and happen every 25 ns at nominal running conditions. The bunch frequency is set by the frequency of the RF cavities. At the end of a run, both beams are disposed of in IR 6, at the beam dump. Extraction kickers horizontally deflect the beam while a septum magnet provides vertical deflection, and the beam is extracted from the default orbit. Afterwards, the beam is spread around in a circle to dissipate the power delivered to the dump evenly. The final absorber consists of a 7 m long carbon cylinder contained in a steel cylinder surrounded by concrete and iron shielding.

1.3.1.2 HL-LHC

After 2026, the HL-LHC will supersede the LHC, a project that will improve the accelerator's luminosity. Luminosity measures of the rate of potential collisions at the different interaction points. The design luminosity for HL-LHC is $7 \times 10^{34}\,\mathrm{cm}^{-2}\,\mathrm{s}^{-1}$ which will increase the data sample by one order of magnitude compared to the LHC design. The HL-LHC will use the same structure and elements from the LHC [27]. The most important parameters including the number of bunches, beam current, minimum β^* (β value at the interaction point), highest instantaneous luminosity and the number of events per bunch crossing of the HL-LHC and their comparison to LHC are shown in Table 1.1 [28].

Table 1.1: HL-LHC main parameters for proton-proton collisions compared to LHC.

Parameter	LHC (design report)	HL-LHC (design report)
Bunches	2808	2808
Beam Current (A)	0.54	1.1
Minimum β^* (m)	0.55	0.15
Peak luminosity ($10^{34}\,\mathrm{cm}^{-2}\,\mathrm{s}^{-1}$)	1.18	7
Events/crossing	40	140

The physics motivation for the upgrade includes higher precision Higgs boson measurements and measurements of rare Higgs decay modes and production, as well as searches for physics beyond the Standard Model.

The HL-LHC aims at delivering $3000\,\text{fb}^{-1}$ to the interaction points of its experiments in ~ 10 years while the LHC will have achieved $300\,\text{fb}^{-1}$ in ~ 10 years of operation. The means to reach higher luminosity is to reduce β^* through stronger triplet quadrupoles. However, this implies a larger crossing angle, which leads to a decrease in luminosity. To mitigate this problem, crab cavities will be installed. Crab cavities are radio-frequency (RF) cavities capable of generating transverse electric field rotating the colliding bunches and improving the overlap between the beams, thus increasing the instantaneous luminosity. Other hardware upgrade for the HL-LHC includes use of Nb_3Sn magnet technology (compared to Nb-Ti used by LHC, capable of producing fields up to $9-10\,\text{T}$) which provide fields of over $10\,\text{T}$ (up to $12\,\text{T}$). These will be used in the interaction regions and matching sections.

1.3.1.3 HE-LHC

A proposed Future Circular Collider (FCC) with the new state of the art technology reaching up to $100\,\text{TeV}$ collision energy is one potential candidate for a future particle accelerator at CERN for the post-LHC era [29]. The study of the FCC design incorporates an investigation of transforming the current LHC tunnel into a higher energy proton-proton collider, the High-Energy Large Hadron Collider (HE-LHC) [30]. It would use the LHC tunnel in combination with FCC technology such as lattice optics, beam instrumentation and magnets to reach collision energy of up to $27\,\text{TeV}$. This proposal would double the energy reach of the LHC while not requiring a large-scale excavation cost for FCC or any new collider. The energy increase would be provided by $400\,\text{MHz}$ superconducting cavity system, similar to that of the HL-LHC. The main parameters of the HE-LHC compared to LHC are shown in Table 1.2.

Table 1.2: Main beam parameters for proton-proton collision mode of the HE-LHC compared to the LHC.

Parameter	HE-LHC	LHC (design report)
Centre-of-mass energy (TeV)	27	14
Peak arc dipole field (T)	16	8.3
Minimum β^* (m)	0.45	0.55
Peak luminosity ($10^{34}\,\text{cm}^{-2}\,\text{s}^{-1}$)	16	1.18
Events/crossing	460	40

1.3.2 Detectors

Particle detectors measure the products of particle collisions in order to precisely evaluate the properties of known and search for currently unknown particles. The specific detectors presented in this thesis are the ATLAS detector at the LHC and the FASER detector at the LHC.

1.3.2.1 ATLAS

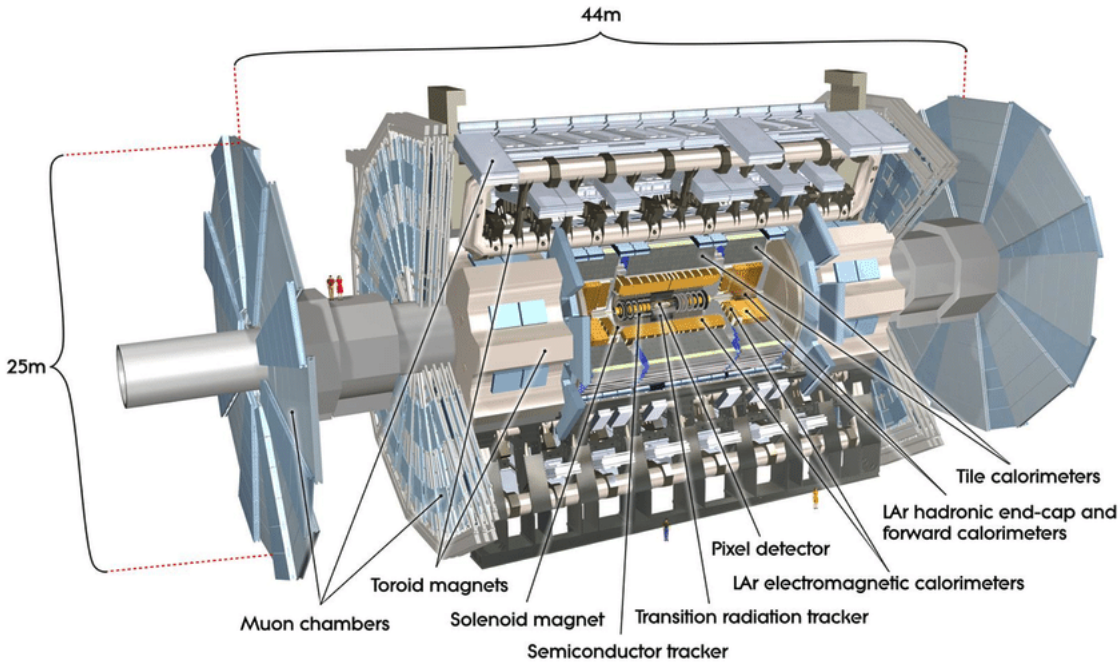

Figure 1.12: ATLAS detector layout [31] with its subdetectors.

The A Toroidal LHC Apparatus (ATLAS) detector is a cylindrical multi-purpose particle detector located at the IP 1 of the LHC. Its layout is shown in Figure 1.12. It is the largest detector of the LHC, measuring 25 m in diameter and 44 m in length. The interaction point in the centre of the detector is surrounded by an inner tracker, superconducting solenoid, electromagnetic and hadronic calorimeters, and a muon spectrometer [2].

The ATLAS coordinate system, shown in Fig. 1.13, is a right-handed Cartesian system (x,y,z), with the origin at the interaction point at the centre of the detector. The x-axis points towards the centre of the LHC, the y-axis points to the sky, and the z-axis is pointing in the direction of the beamline towards IP 8 of the LHC ring. Using the cylindrical coordinates (r,η,ϕ), the pseudorapidity η is defined as:

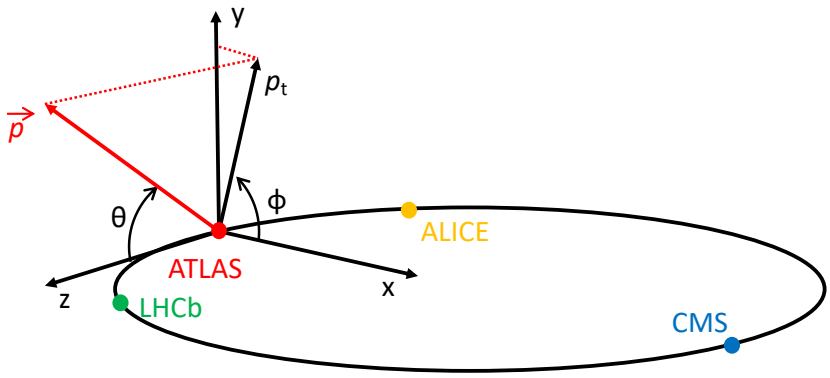

Figure 1.13: ATLAS coordinate system. The x-axis is oriented towards the centre of the LHC ring, the y-axis points to the sky, and the z-axis is oriented towards IP 8.

$$\eta = -\ln\left(\tan\frac{\theta}{2}\right), \tag{1.39}$$

where the polar angle θ is the angle between the momentum vector and the z-axis. The azimuthal angle ϕ is defined as the angle between the x-axis and a particle's transverse momentum vector (p_t). p_t is the momentum component transverse to the beam direction (in this case, the z-axis).

The ATLAS inner tracker consists of three parts, the pixel detector, the semiconductor tracker (SCT) and the transition radiation tracker (TRT). The original pixel detector had over 80 M readout channels spread out in three cylindrical layers in the barrel and three 2-layer disks in the endcap. A fourth Insertable B-Layer was added for Run 2 [32]. The SCT uses strips of silicon to provide over 6 M readout channels distributed over 4 cylindrical layers in the barrel and 18 disks in the endcap. The TRT provides approximately 350 k readout channels with 4 mm diameter straw tubes and in addition to measuring the position of charged particles, it can also be used for electron identification. Together, the inner detector measures the position and momenta of charged particles with pseudorapidities up to $|\eta| = 2.5$.

A solenoidal superconducting magnet with a 2 T magnetic field surrounds the inner tracker, which is enveloped by the calorimeter system designed to absorb most particles and measure their energy. It comprises the Liquid Argon (LAr) Calorimeter and the Tile Hadronic Calorimeter. The LAr is an electromagnetic calorimeter measuring the energy of electrons and photons. It is built from layers of lead and stainless steel, intended to

absorb the energy of photons and electrons, submerged in liquid argon, which is ionized by traversing particles. The ionized molecules produce electric current measured by the detector which is proportional to the energy lost by the particles. The Hadronic Calorimeter measures the energy of hadronic particles which the LAr does not absorb. It is made of steel absorbing sheets layered with sampling plastic scintillator tiles, recording the hadronic shower products. Both calorimeters cover the pseudorapidity range of $|\eta| < 4.9$.

The rest of the ATLAS detector, the muon system, is dedicated to measuring the energy and trajectory of muons, the only charged particle not absorbed by the calorimeter detector systems. The muon spectrometer uses three toroidal magnets with a field up to 3.5 T and four detector systems: the Thin Gap Chambers, the Resistive Plate Chambers, the Monitored Drift Tubes and the Cathode Strip Chambers, which provide 4000 individual muon chambers. The muon system has pseudorapidity of $|\eta| < 2.7$.

ATLAS also includes a Beam Conditions Monitor (BCM) dedicated to beam background identification. The BCM consists of 2 stations of 4 modules, at a longitudinal distance of ± 184 cm from the centre of the detector, at a radius of 55 mm from the beam line. Two modules are in the horizontal and two in the vertical plane on each side of the IP. Each module has two back-to-back diamond sensors with an active area of $8 \times 8\,\mathrm{mm}^2$ and a total thickness of 1 mm.

During the Phase II upgrade, while the LHC is upgraded to the HL-LHC, ATLAS will have part of the detector subsystems upgraded or replaced. These changes will include the inner tracker and muon and electron trigger systems. The tracking of the ATLAS experiment will be fully replaced by a silicon detector called the inner tracker (ITk). This detector will be made of cylindrical and endcap layers of pixels and microstrips. The ITk will cover a volume of 7 m in length and 1 m in diameter. A new subdetector - the High Granularity Timing Detector (HGTD) will be installed in the gap between the electromagnetic calorimeter and endcap cryostats ($z = \pm 3.5$ m), which will provide fast timing to help with vertex identification given the much higher pile-up during HL-LHC operation.

At the ATLAS detector, protons collide with a frequency of 40 MHz (every 25 ns). The detector and storage systems cannot record and keep all events. Therefore, events are filtered only by storing those interesting from the perspective of the physics programme, including, for example, the W, Z or Higgs bosons. The trigger system uses fast online algorithms to reconstruct the most prominent features of the physics events as they are

recorded. The trigger system has two levels. The first level (L1) trigger reduces the event rate to approximately 100 kHz. The second level, the high-level trigger (HLT), reduces the data output to 2 kHz. The L1 trigger is processed at the hardware level for muon detector systems and the calorimeters. The HLT trigger is software-based, and trigger calculations are performed on a computer farm at IP 1. It focuses on specific key signatures of physics processes of interest, such as single high-p_T or large E_T^{miss} events.

1.3.2.2 FASER

The ForwArd Search ExpeRiment (FASER) is an LHC experiment located 480 m along the beampipe from the ATLAS interaction point. The experiment is designed to search for a variety of light, weakly-coupled hypothetical particles, such as dark photons, dark Higgs bosons [4], heavy neutral leptons (sterile neutrinos) [33], and axion-like particles [34]. These particles could be produced in the decay of particles produced in the LHC collisions or by the interaction of these particles with material [4]. It will also be the first experiment sensitive to neutrinos produced by a collider experiment. The FASER detector has a cylindrical shape approximately 5 m long with a radius 30 cm oriented towards the ATLAS interaction point. It consists of a pair of scintillators surrounding an emulsion neutrino detector. Then a lead decay volume initiates an electromagnetic shower detected by a spectrometer consisting of three tracking stations surrounded by two permanent bending magnets. The last part of the detector is an electromagnetic calorimeter. A schematic of the detector is shown in Fig. 1.14. FASER was commissioned in 2021 and is expected to collect 150 fb^{-1} of data from $2022 - 24$, corresponding to Run 3 of the LHC operation schedule.

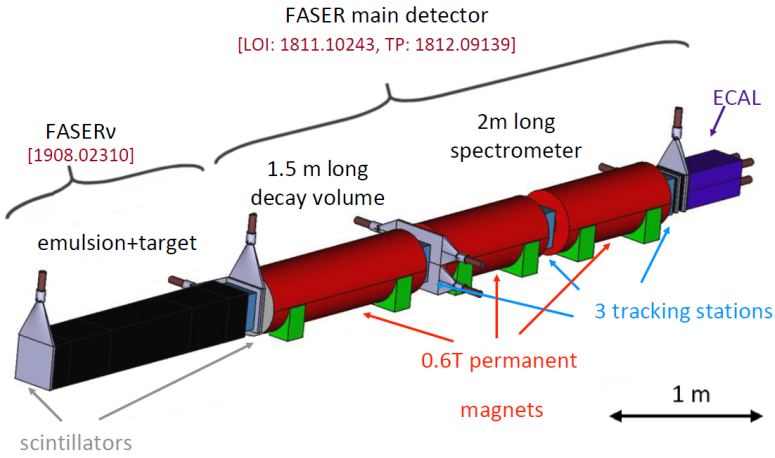

Figure 1.14: FASER and FASERν detectors and their subdetectors.

1.4 Background sources and their identification

A very large amount of energy is stored in the circulating beams of the LHC (360 MJ per beam [35]) and even more will be in the HL-LHC (700 MJ per beam [27]) and HE-LHC (1.4 GJ per beam [30]). A loss as small as 3×10^{-6} of the nominal beam intensity may induce a quench in the superconducting magnets, cause physical damage to scientific elements or interfere with the physics signal of the experiments [36]. Many processes that lead to beam losses, more generally called the beam-induced background (BIB). BIB relevant to physics analyses at collider detectors such as the ATLAS detector are part of the so-called non-collision background (NCB), which also includes detector noise, and cosmic-ray backgrounds.

At the LHC, BIB happens all around the ring, the primary sources relevant for the ATLAS detector arise from tertiary beam halo impacts and elastic beam-gas collisions. A diagram of the creation of these background sources is shown in Figure 1.15.

BIB affects the beam lifetime as its events cause a decrease in the number of protons in the beams. In the HL-LHC, the total proton-proton cross section at beam energy of 7 TeV is approximately 110 mbarns, meaning the beam lifetime due to proton-proton collision at the interaction points is approximately 80 h. The rate of the decrease of lifetime due to BIB is different for each beam background origin. The calculation of the loss rate is used in this thesis for the scaling of the beam background simulation results.

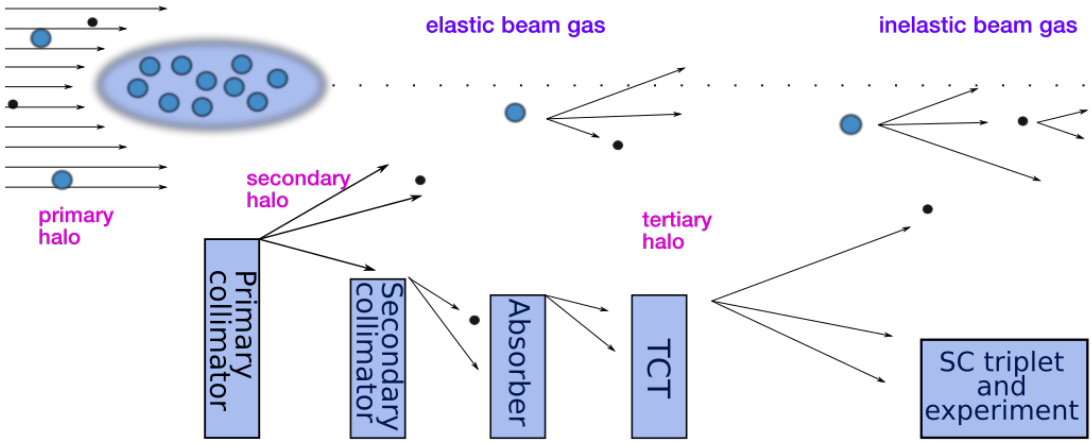

Figure 1.15: Origins of beam background around the LHC ring. Beam halo is created from interactions between bunch particles and accelerator structures, beam-gas depends on the gas density inside the beam pipe.

1.4.1 Beam halo losses

A beam halo consists of a small fraction of beam particles surrounding a dense beam core which creates a spread in position and momentum of the beam resulting in losses. Especially in the cleaning sections (IR 3 and IR 7) of the accelerator and before collisions where beams are squeezed together, beam halo particles can be scattered at wide angles and lost. A diagram in Figure 1.16 illustrates the beam halo passage through a collimator with resulting losses.

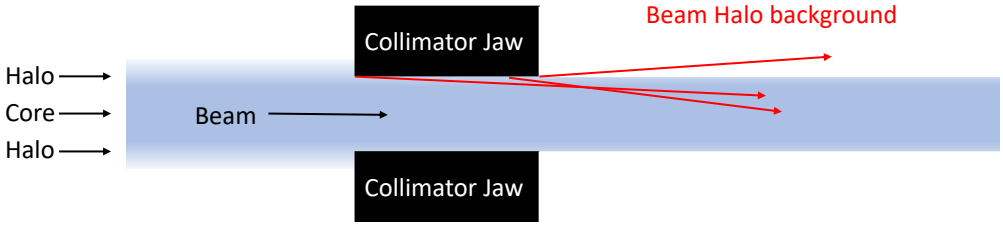

Figure 1.16: Diagram of beam halo interactions with a collimator. Particle showers created by beam impacting on the jaws can be absorbed by the collimator material or propagated further inside or outside the beam pipe.

For ATLAS, the beam halo cleaning background originates at aperture restrictions, particularly at the tertiary collimators, located 150 m from the interaction points. The main collimators around the LHC ring are shown in Figure 1.17.

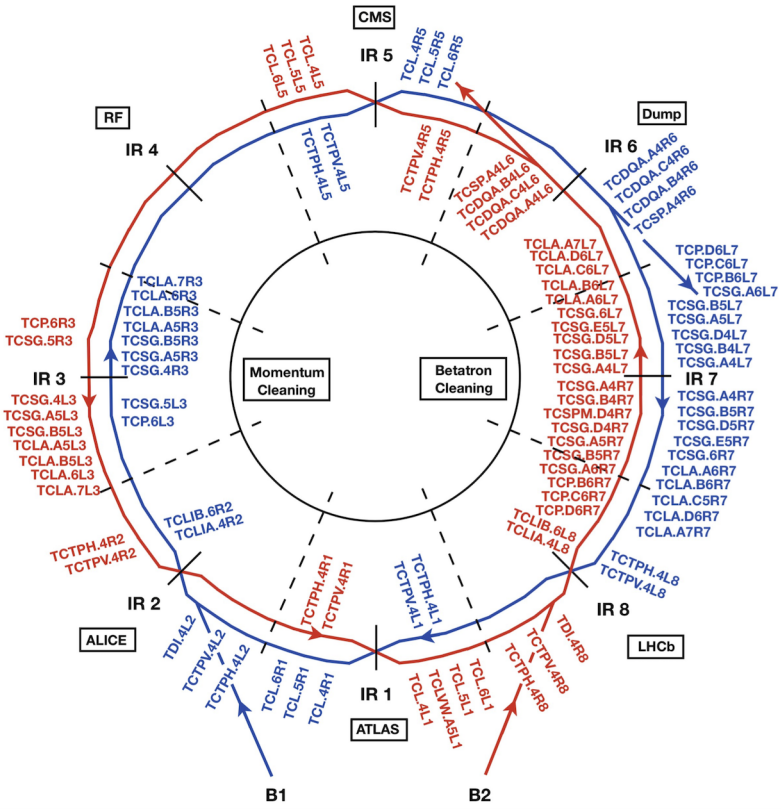

Figure 1.17: Collimation system layout with all collimators for beam 1 (blue) and beam 2 (red) [37].

Collimators at the LHC are grouped into families according to their use. Table 1.3 summarises their names, purpose and numbers. The most relevant collimators for this thesis are the Target Collimator Primary (TCP) and the Target Collimator Tertiary (TCT). The primary collimators are the first to intercept beam particles too far from the core. Tertiary collimators protect the particle physics experiments.

An example of a collimator jaw is shown in Figure 1.18, showing a movable jaw of a secondary horizontal collimator with its support and cooling pipes. The 1 m long jaw is made of graphite and has tapered ends which prevent impedance problems from geometric changes between the movable collimator jaw and the subsequent vacuum chambers.

Table 1.3: The acronym, purpose, count, and jaw material and length of the main LHC collimators.

Acronym	Purpose	Number	Material	Length
TCP	Primary collimator	8	C	0.6 m
TCS (G&M)	Secondary collimator	30	C	1.0 m
TCT (a&b)	Tertiary collimator	10	W	1.0 m
TCLI (a&b)	Absorbers for injection protection	2	C	1.0 m
TCLP	Absorbers for physics debris	4	Cu	1.0 m
TCLA	Absorbers for showers in IR 3 and IR 7	∼16	Cu	1.0 m

Figure 1.18: Graphite jaw of a LHC secondary collimator [38], the graphite jaw is 1 m long and features two tapered ends.

The minimum beam lifetime sufficient for no damage of any accelerator component in the HL-LHC is 12 minutes [39], called the *critical beam lifetime*. For studying background levels during regular operation, we use the optimistic beam lifetime of 100 hours called *long beam lifetime*. This lifetime is determined assuming default running conditions with no unexpected losses.

The rate of background loss due to beam halo can be expressed as:

$$R_{BH} = \frac{N_p N_b}{\tau_{beam}} \tag{1.40}$$

where N_p is the number of protons in a bunch, N_b is the number of bunches and τ_{beam} is the beam lifetime.

The rate of beam halo loss at the HL-LHC for the critical beam lifetime is $\sim 10^{12}$ protons per second and $\sim 10^{9}$ protons per second for the long beam lifetime.

1.4.2 Beam-gas interactions

Beam-gas background is created during encounters between residual gas molecules in the beam pipe and beam particles resulting in beam particle losses. Beam-gas encounters create background particles that can be passed through the beam pipe and potentially into detector systems. The intensity of beam-gas background radiation scales with the pressure in the beam pipe (about 10^{-6} mbar).

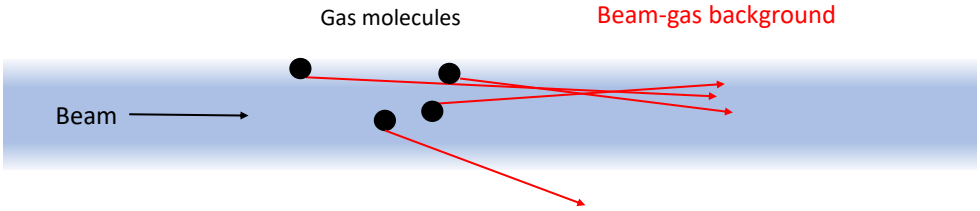

Figure 1.19: Diagram of beam-gas interactions. The high energy protons interact with the large gas molecules (black) and create particle showers or change their momentum to create beam-gas background (red).

At the LHC, inelastic collisions between beam particles and residual gas occur in the vacuum pipe near the experiments are called *local beam-gas* background. Local beam-gas is the primary source of background for the experiments. *Global elastic beam-gas* is caused by scattering around the ring, with the proton later being intercepted by the beam cleaning insertions or tertiary collimators. Global beam-gas has a negligible contribution at the location of interaction points [40].

The rate of beam-gas interactions is proportional to the gas density and the scattering cross-section. For proton-gas nucleus collision (p-gas) at LHC energies, the inelastic scattering cross-sections for the most common gases are shown in Table 1.4 [41].

For a single bunch in the LHC, the number of proton-gas interactions in the accelerator is:

$$N = \sigma \rho N_p N_b l \tag{1.41}$$

where σ is the scattering cross-section for the specific gas, ρ is the gas density, N_p is the

Table 1.4: Gas densities and proton-gas cross sections for beam current 530 mA and beam energy 7 TeV [41].

Gas	Density (10^7 mol/cm^3)	Cross section (mb)
H_2	0.98	94
CH_4	0.18	568
H_2O	0.55	554
CO	0.98	840
CO_2	4.70	1300

number of protons in a bunch, N_p is the number of bunches, and l is the distance travelled (the LHC circumference). Using the frequency of revolution (f), the interaction rate of beam-gas events is:

$$R_{BG} = Nf. \tag{1.42}$$

For example, the rate of proton losses in the LHC due to residual hydrogen gas is approximately 1.7 MHz.

1.4.3 Other loss mechanisms

The **Touschek effect** causes beam losses by scattering two charged particles in a part of the beam. Such scattering transfers transverse momentum into longitudinal momentum, and the particles are lost as they exceed the momentum acceptance of the accelerator. The typical lifetime of this beam loss mechanism at the LHC is approximately 500 days [42].

Synchrotron radiation occurs when an accelerated charged particle traverses a magnetic field. In turn, these radiation losses contribute to lowering the beam energy. At the LHC, the loss by synchrotron radiation is about 7 keV per turn, corresponding to a lifetime of approximately 1 day.

Beam-beam interactions cause perturbations in particle bunches as two passing beams interact through a long-range electromagnetic force.

Finally, other loss mechanisms exist, including unidentified falling objects (UFOs), electron cloud effects, operator error, beam instabilities etc. These mechanisms can be considered to have a negligible effect on the results presented in this thesis.

1.4.4 Physics debris

Another source of accelerator background originates from collisions of primary beam particles within the detector systems around the IPs. Particles backscattered from the detector with a small theta angle can be reinserted into the beam pipe and may collide with downstream accelerator components. Particles that could reintegrate the beam will, in turn, increase its emittance. Ultimately, these particles are filtered by the betatron collimators in IR 7. The particle loss originating from physics debris has a lifetime of approximately 300 hours.

Diffractive events (for example, single diffractive events, where the outgoing proton is reinserted into the beampipe) with larger momentum change δp will be mostly lost within the straight section. For $\delta p < 0.01$, particles are lost in IR 3, for $0.01 < \delta p < 0.25$, particles are lost inside the straight section downstream of the TAN[1] (an absorber located 140 m from IP 1) and for particles with $\delta p > 0.25$, particles are lost in the TAN.

Physics debris propagating through the ring can create a tertiary halo in another experiment, which is another type of machine-induced background called the *cross-talk*. Cross-talk depends on the luminosity at the original collision point and the position of the tertiary collimators in the receiving experiment in terms of phase advance.

1.5 Summary

This chapter outlined the basic history of accelerators and their concepts. Particle accelerators have been used since the 1930s, and their use has grown from nuclear and particle physics research to applications in medicine and industry. The LHC and its future upgrades, the HL-LHC and the HE-LHC, used in this thesis, are the largest synchrotron (and accelerator in general) ever built, achieving record beam energies. Beam losses are expected during accelerator operation. They must be reduced to decrease the levels of accelerator background, and well understood, to accurately simulate their effect. Specialized software tools are required for the study of beam background. These tools, presented in the next section, are used for many particle physics experiments and can handle a variety of beam background scenarios.

[1] Target Absorber Neutral

2 | Simulation strategies

This thesis aims to understand the particle showers generated in the LHC beamline and experiments that can reach the ATLAS, CMS and FASER detectors. Accelerator simulations have been applied to model the regions of interest to help the experiments understand the particle spectra and rates at the detectors. This chapter covers the simulation tools available to study particle transport in an accelerator, presents the methodology and gives a detailed overview of the geometry models.

2.1 Tools

Particle passage through an accelerator is complex. Each accelerator component, such as a magnet, collimator, or a RF cavity, affects the beam in a specific way. Advanced simulation tools are needed to simulate the beam trajectory and the interactions between the beam particles and the accelerator elements. There are many accelerator simulation programs. Some offer only singular use, such as software that generates magnetic field maps based on magnet geometry. Others are more general software capable of particle tracking through a series of elements. The main software packages used in this thesis are BDSIM, FLUKA and SixTrack. These are presented in this section along with the ATLAS detector simulation software, the CRMC event generator, and Pyg4ometry, a package for geometry manipulation.

2.1.1 BDSIM

BDSIM is a program written in C++, uniting accelerator tracking routines with particle-matter interactions [43]. BDSIM uses the Geant4 toolkit [44] to build a 3D model from an accelerator optics input with various accelerator components.

The model can be created from optical description files such as the MADX [45] output format, called twiss. A twiss file contains the values of optical parameters for all

accelerator elements. Different generic or custom apertures can be used for all components as well as a variety of magnet yoke designs, which are shown in Fig. 2.1. Custom geometry can also be provided as well as magnetic field maps. For studies of accelerator lines, the vast library of generic accelerator elements offered by BDSIM is faster and more flexible than using low-level simulation codes such as Geant4. BDSIM also provides a rapid 3D visualisation of the simulation project, a feature seldom offered by similar simulation tools. The manipulation of the simulation is done using simple text file input.

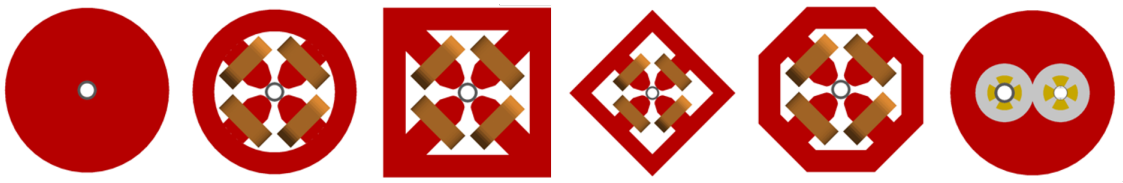

Figure 2.1: BDSIM quadrupole magnet yoke designs. From left: cylindrical, poles circular, poles square, poles faceted, poles faceted with crop, and LHC left and right

BDSIM provides multiple routines to calculate the trajectory of particles propagating in magnetic fields. The default Geant4 tracking algorithm works for thick lens tracking in global Cartesian coordinates and uses 4th order Runge-Kutta integrators [46]. Thin elements such as fringe fields and thin multipoles do not appear in Geant4; therefore, special BDSIM integrators must be used. BDSIM performs the transforms between Cartesian and curvilinear coordinate systems using a parallel geometry of cylinders that follow the beamline. The default BDSIM integrator uses the default Geant4 tracking with special BDSIM integrators for specific magnetic field types. BDSIM is in agreement with both MADX and PTC tracking codes. The output is generated using the ROOT file format [47]. BDSIM also provides analysis tools for its output file format and ROOT dictionaries for handling custom classes. The limitations of BDSIM are in the particle energy upper limit (maximum 100 TeV for a single particle) and the maximum physical size of the model. BDSIM uses a length of 10^{-9} mm between all solids as a safety tolerance to avoid infinite recursion. In practice, a model of the size of the LHC is on the limit for asserting tracking precision of 10^{7} mm, because of numerical tolerance due to the use of double precision numbers.

BDSIM is suitable for the beam background studies presented in this thesis as both tracking inside an accelerator and particle-matter interactions must be simulated.

Even though the simulation software was validated for other applications, results should be cross-validated with data or other programs to ensure their accuracy. In this

thesis, a set of results obtained using BDSIM simulations are compared to to previous work with BDSIM and FLUKA.

2.1.2 FLUKA

FLUktuierende KAskade (FLUKA) is a general purpose Monte Carlo program, initially developed for studies of particle showers in blocks of material, now used for transport of particles in matter and through electromagnetic fields [48, 49]. It is used by the radiation protection, acceleration design, shielding and detector simulation groups at CERN and for applications in dosimetry, radiotherapy, cosmic rays and others. FLUKA is supported by Flair [50], a visual interface also used for the input of beam properties and geometry files. FLUKA tracks particles using adaptive stepping algorithms, which solve the equations of motion at each step. Tracking through both magnetic and electric fields is available.

2.1.3 SixTrack

SixTrack is a two-particle tracking code optimised for long-term propagating in the electromagnetic field of high-energy accelerator rings, such as the LHC [51]. It uses a six-dimensional phase space for tracking particle motion in a symplectic manner. Symplecticity is linked with preserving the phase space volume occupied by the particle beam. SixTrack is used for particle tracking but is not suitable for particle-matter interactions. For that reason, its output can be supplied to other simulation programs such as BDSIM and FLUKA.

2.1.4 ATLAS simulation software

Physics events originating from collision or backgrounds are simulated using a Monte Carlo simulation of the ATLAS experiment. The process has the following structure: event generation, detector simulation, digitisation and reconstruction. Event generation is done with a specific event generator created for use with the desired physics process. Then, particles are propagated through the detector and interactions with the sensitive material of detector subsystems are recorded. Digitisation is specific to each sub-detector and mimics the electronic readout output. Finally, reconstruction includes pattern recognition and reconstruction of tracks, segments, vertices, cells and clusters in the different sub-detectors. Higher level objects are also produced, such as missing energy estimation and jet identification.

2.1.5 CRMC

The Cosmic Ray Monte Carlo (CRMC) is a package used for studying particle production [52] from a cosmic-ray or a hadronic collisions. CRMC features collision models for simulating the physics debris from IP 1 and generating the beam signal and background of interest in this thesis in Chapter 6. The models used in this thesis are SIBYLL, EPOS and PYTHIA. CRMC comprises various cosmic-ray and non-cosmic-ray event generators. The generator produces output in different formats, including the HepMC event file, which is readable by BDSIM. The SIBYLL model is a hadron interaction event generator used for air shower, fixed target and collider simulations, and its results are comparable with ATLAS forward experiments [53, 54]. EPOS is a Monte Carlo generator for minimum bias hadronic interactions, which can reproduce LHC results for a set of parameters (small transverse momentum, which is the case of this simulation) [55]. Comparison between the CRMC simulated events and Run 1 LHCb minimum bias events are within the uncertainty level for the SIBYLL and EPOS models [56]. PYTHIA is the default model used in ATLAS physics analyses [57].

2.1.6 Pyg4ometry

Pyg4ometry is a python package designed to be a simple and flexible tool for creating geometry models usable by Geant4 and FLUKA [58]. It can create geometry from scratch or load and edit existing models. Programmable geometry generation simplifies and decreases the time needed for creating geometry models. A parametrisation of geometry reduces the possibilities for errors and makes scaling and reproducing the volumes very easy. Pyg4ometry also offers overlap checking and visualisation capable of showing said overlaps.

2.2 Methodology

2.2.1 Goals

The goals of the work presented in this thesis can be separated into different parts: model construction, event simulation and analysis. Geometry models, presented later in this Chapter, were created for all simulation studies except for particle propagation into the ATLAS detector, which has a very detailed geometry already available within the ATLAS

simulation software. The main goal of the studies is to look at general trends of background radiation. Evaluating and understanding the differences in background radiation levels for various optics parameters or changing single element geometry while using the same level of detail of the model is the primary purpose of this work. The overall geometry is comprehensive while using BDSIM generic components, which significantly increase the model creation and simulation speed. The event simulation process is optimised for speed while keeping all necessary particle and tracking information. Raw data was only used in the beginning stages of the work, after which only histogram files were held using BDSIM's analysis tool rebdsim.

2.2.2 Biasing

Biasing is used to increase the probability of physical processes of interest. It does so by assigning weights to particles, which are inversely proportional to the ratio of the biased and nominal generation probabilities. This thesis uses two biasing techniques: cross-section biasing and particle splitting. These are available in the BDSIM software.

Cross-section biasing introduces a numerical scaling factor by which the cross-section of a selected process is multiplied. The user has to specify the particle, the process of interest to be scaled, and the scaling factor. Particles generated through the selected process are then assigned appropriate weights based on the scaling factors. Depending on the interest, cross-section biasing can be applied only within certain geometry regions or materials; it can also be used for only primary particles, secondary particles or all particles.

Particle splitting offers an increased production of a specific particle. When a desired secondary particle is produced, the generation process and the parent particles are wrapped in a physics process. This process is then repeated many times which could produce the desired particle again with different momenta and energy. Each new outcome is re-weighted to match the input weight. At present, only muons can be used in BDSIM for biasing by splitting. Muons are particularly interesting because of their relatively long lifetime and low interacting characteristics. If a muon is produced in an interaction, the process is randomly repeated several times, corresponding to the sampling number. The weight of new particles is then adjusted accordingly, typically by dividing their current weight by the splitting factor.

2.2.3 Simulation Scaling

BDSIM provides results scaled per single primary particle irrespective of the number of particles simulated. To obtain meaningful results, results must be normalised based on the actual operation parameters of the accelerator. In the case of this thesis, the LHC or HL-LHC machine parameters are used.

The scaling factors used for HL-LHC BIB events presented in Chapter 1 are: $R_{BH} \sim 10^9$ Hz for beam halo background (for beam lifetime of 100 hours) and $R_{BG} = 1.7$ MHz for beam-gas background. Simulations of particle production at the ATLAS interaction point during the LHC Run 3 are scaled using the instantaneous luminosity of $2 \times 10^{34}\,s^{-1}\,cm^{-2}$.

2.2.4 Error quantification

Results are saved per primary event in user-defined bins where each bin is associated with the mean of a physical quantity. The error on the bin is the standard error on the mean (standard deviation of the values associated with the bin for the whole dataset divided by the square root of the sum of weights).

The systematic error is a consistent, repeatable error associated with the experiment design and calibration. Such errors result from observational, instrumental, environmental and theoretical sources.

2.3 Simulation models

At a minimum, accelerator simulations require optical parameters to create a lattice for particle propagation. For simulations of beam loss, an accurate aperture model must be added. To have a complete understanding of the background generated by high energy particles and their propagation, the geometry of the accelerator elements and the shielding and tunnel structure should also be included in the model. In the regions of topmost interest in this thesis, that is, the vicinity of the ATLAS, CMS and FASER detectors, higher accuracy and more detail are required. Therefore, the models are generally custom-built and include all physical volumes with sufficient detail. In regions of lower interest, the basic geometry of accelerator elements and surrounding shielding (for example, tunnel walls) are adequate.

2.3.1 LHC and HL-LHC high luminosity interaction section model

This section presents the geometry models used in beam transport simulations in the interaction regions IR 1 and IR 5. The same tunnel geometry is used for incoming particles from beam 1 (direction of IP 8 to IP 1 and IP 4 to IP 5). Beam 2 (direction of IP 2 to IP 1 and IP 6 to IP 5) uses a more simplified tunnel model as it is used only for general comparison to beam 1. The accelerator elements and absorber and shielding volumes are specific to the location of interest. These models are used in Chapters 3, 4 and 6. The geometry models represent the $250 - 3000\,\mathrm{m}$ long section between IP 1 or IP 5 and the beginning of the arc or IP 8 depending on the specific simulation case. The geometries are created by combining multiple sections: a converted tunnel section, a custom-made section and several generic sections. The first section is converted from an existing FLUKA file and covers the region around the IPs. The second section is a generic BDSIM tunnel section. The third section is a custom-made tunnel section with a side tunnel housing the FASER detector. Any additional sections are again generic BDSIM tunnel sections. The $\sim 540\,\mathrm{m}$ long section used for the beam-gas background simulations is shown in Figure 2.2.

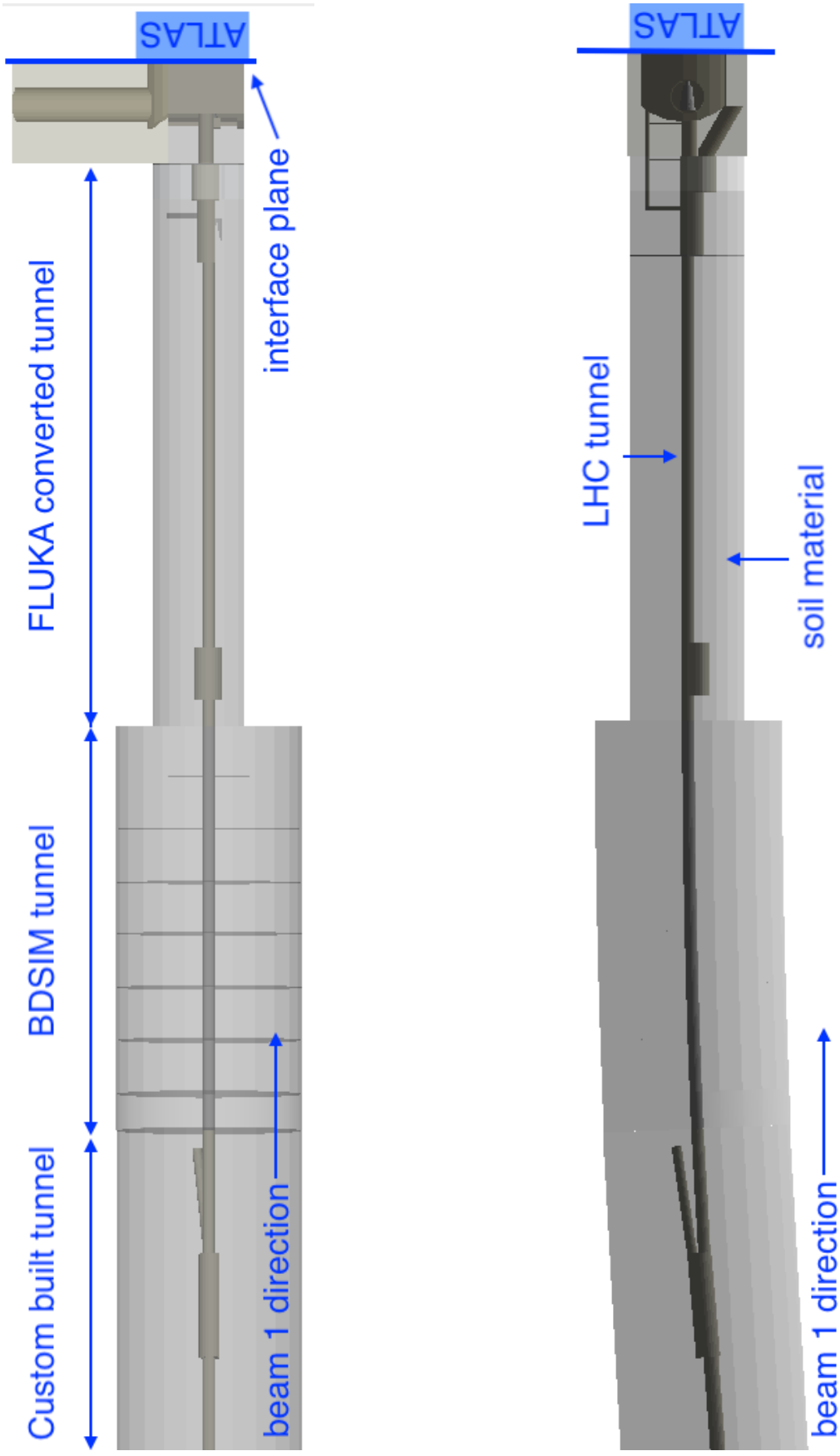

Figure 2.2: Side (upper) and plan (lower) view of the geometry model leading up to the ATLAS detector. The approximately 600 m long and 50 m wide model includes the main LHC tunnel, service tunnels and various rooms attached or close to the main tunnel.

The first section, shown in Figure 2.3, covers part of the ATLAS experimental hall with the interaction point and the full straight section of IR 1 with total length of approximately 250 m. It is converted from a FLUKA model [59] of the IR 1 using pyg4ometry. The conversion is done from the FLUKA "input" file format (INP) to a GDML file format, which is supported by Geant4 and BDSIM and can be further manipulated in pyg4ometry. It includes the transition from the general cylindrical LHC tunnel to the smaller square-shaped hole near the IP, the ATLAS experimental hall shape and the side rooms and shaft structures.

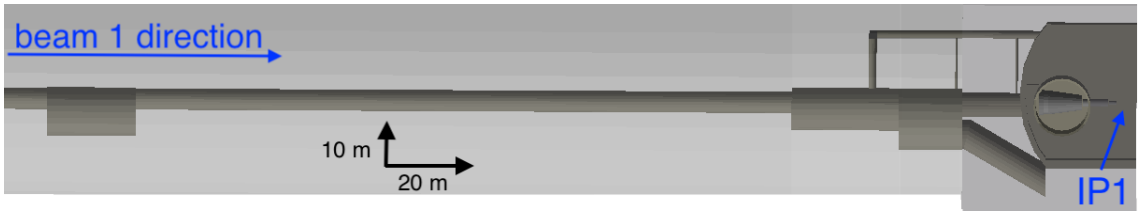

Figure 2.3: Top view of the FLUKA converted section of IR 1.

The second section of the model covers the end of the straight section and the dispersion suppressor (DS) section. It is made of a generic BDSIM tunnel defined using the particular dimensions of that particular LHC tunnel section and follows the machine curvature. Its cross-section is shown in Fig. 2.4. Outside of the concrete tunnel is a soil material, which spans over a diameter of 30 m. The soil has a uniform density set to be the average density measured during geological studies for the LHC (approximately 2.5 tons/m^3) [60]. This section is about 160 m long.

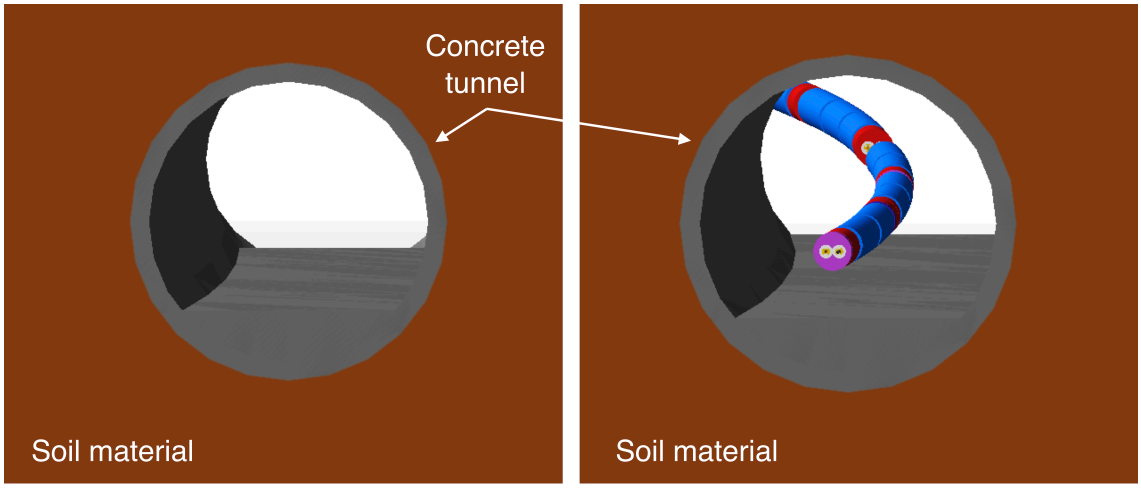

Figure 2.4: Generic BDSIM tunnel section without (left) and with (right) added accelerator components.

For the third section, a generic BDSIM tunnel could be used in the IP 1 and IP 5 beam 1 simulations, however, a more detailed section was created $\sim$ 500 m from IP 1 adding the side tunnel (TI12) and local room structure (UJ12). This section was created specifically to study particle propagation between the ATLAS and FASER experiments. It covers approximately 150 m and is shown in Figure 2.5. The room UJ12, which unites the LHC and TI12 tunnels, was added onto the LHC tunnel geometry. After that, the TI12 tunnel, which houses the FASER experiment, was added.

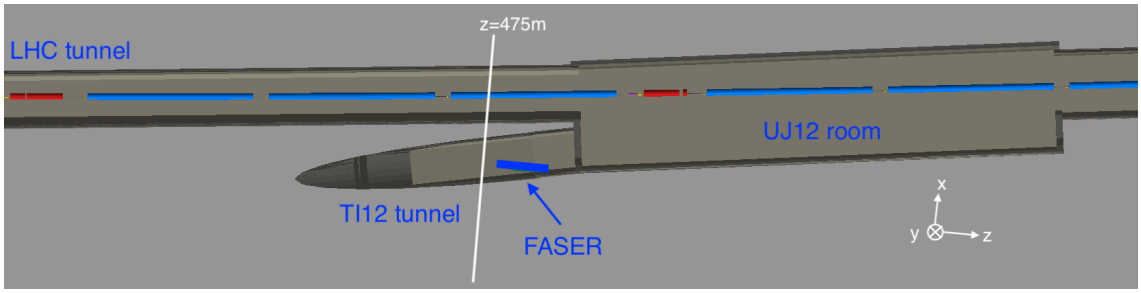

Figure 2.5: Detailed view of the area around the FASER detector with a plane cut at $y = 1$ m above the beam line.

After the UJ12 room, a generic BDSIM tunnel was added to continue the accelerator model up to IP 8, shown in Fig. 2.6. This section was created for studies of beam-gas background originating from that direction (using beam 1). With this addition, the full geometry spans $\sim$ 2500 m.

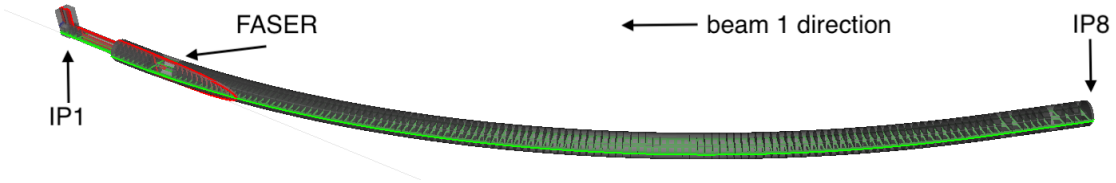

Figure 2.6: The model for beam-gas simulations between IP 8 and IP 1.

Two absorbers, the TAS and the TAN protect the LHC accelerator elements and the particle detectors from physics debris and beam-induced background particles. The TAS [1] is a cylindrical copper shielding placed around the beam pipe starting at a distance of 20 m from the ATLAS interaction point. The TAS protects the LHC triplet magnets outside the experimental hall from physics debris background particles colliding with the beam. It also acts as a shield from the NCB reaching the ATLAS detector. It is 1.8 m long and has a 0.5 m diameter. The TAN is located in front of the second separation dipole

[1] Target Absorber Secondary

- 140 m from the collision point. It is designed to shield the accelerator against neutral particles but also protects the ATLAS detector from NCB. It is 3.5 m long and has a pentagonal face with a maximum radius of 550 mm from the centre of the two beam pipes. The TAN has a more complicated geometry as it houses the Y chamber, which joins the two separated beam pipes into one, and a copper absorber and iron shielding surround it. The absorber geometry, shown in Fig. 2.7, was created in pyg4ometry and added to the beamline simulation model.

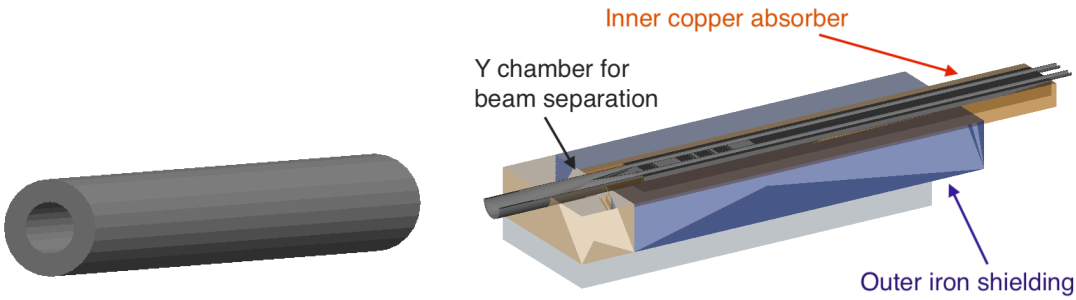

Figure 2.7: The TAS (left) and TAN (right) absorbers visualised with BDSIM.

Additional shielding is provided by four concrete blocks surrounding the beam pipes near the IP. Figure 2.8 shows the geometry of one of these blocks and their positioning in the accelerator. The four blocks are located at 98 m, 118 m, 130 m and 188 m from the IP respectively. Each block was created in FLUKA's Flair software and is approximately 3 m long and 1.5 m high.

2.3.2 HE-LHC model

A model of the HE-LHC geometry was generated using the 27 km long accelerator optical parameters created by MADX, which was then surrounded by a generic BDSIM tunnel section of the LHC tunnel. A full accelerator model was used for multi-turn beam halo studies. The outer layer of the tunnel is set to absorb all outgoing particles (the simulation kills all particles entering the tunnel material) to prevent contamination between different sections of the ring. This model was specifically used to study the effects of beam offset produced in IR 7 on beam background. The cutout of the IR 7 section is shown in Fig. 2.9.

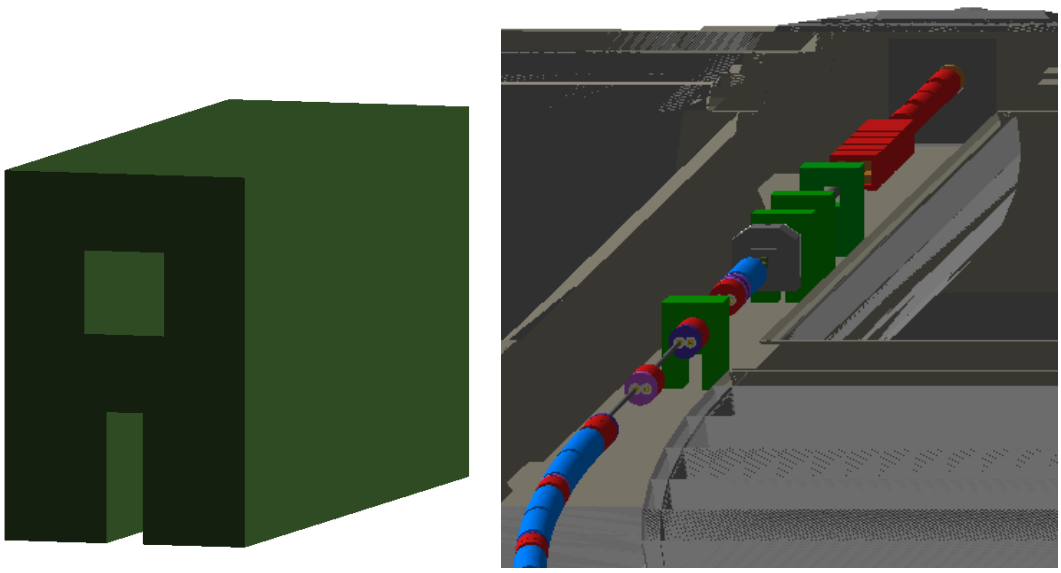

Figure 2.8: The concrete shielding block (left) and all four blocks placed in the beam line (right).

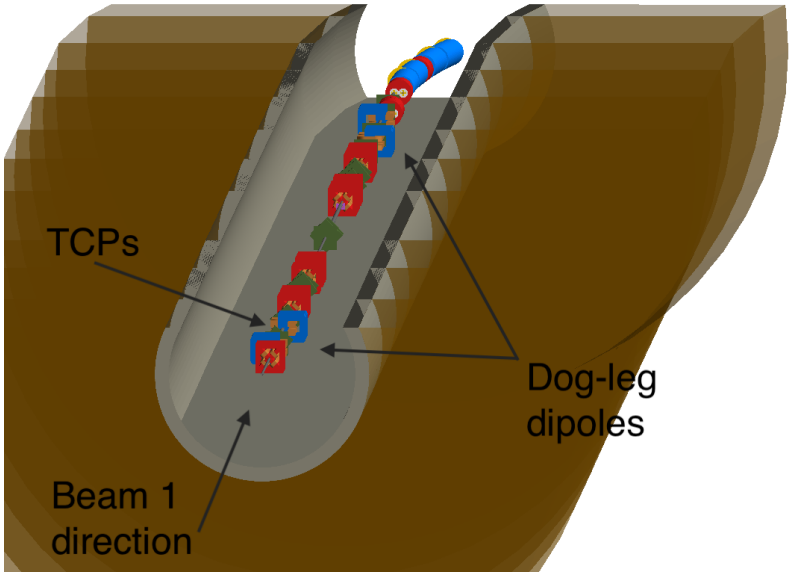

Figure 2.9: HE-LHC geometry model of the IR 7 in the BDSIM visualiser. Collimators are in green and the dog-leg dipoles are blue rectangular bend magnets.

2.4 Summary

BDSIM and FLUKA are general type simulation programs capable of tracking particles inside an accelerator and recording interactions with matter. Similar Monte Carlo software used for accelerator design and modelling is mostly specialised codes targeting single

physical processes or specific applications. Both BDSIM and FLUKA can use input from an event generator such as CRMC and produce output which can be supplied to the ATLAS detector software for particle physics analysis. BDSIM is user-friendly with various pre-defined accelerator and geometry components while accepting external geometries and field maps and comes with a handy analysis suite. BDSIM is used in this thesis for all simulation results unless otherwise noted. The accelerator model typically consists of a set of beamline elements defined by their parameters while neglecting surrounding geometry. Geometry files of magnets, shielding components and even tunnel structures are often created by specialised engineering groups and available in different formats. Pyg4ometry can be used to compile a complete model from different input formats (such as GDML, INP and others) and to create, join and visualise custom geometry which can be used in a Geant4 model. Different analysis strategies are used depending on the process for beam background generation being simulated. Manipulation of the results due to biasing must also be assessed. The level of statistical and systematic errors should be determined in order to consider an approach to improve the confidence of the result. The simulation results of the studies of particle propagation using the software tools described in this chapter are presented in the following chapters.

3 Accelerator background reaching the ATLAS detector

NCB may negatively affect the ATLAS detector. Elevated background rates can reduce the statistical significance of the physics signal and increase the detector occupancy beyond the capabilities of the trigger system. Background signal could also mimic a physics signal (e.g. missing transverse energy in the calorimeter jets), whose effects must be characterized such that appropriate analysis cuts are introduced to remove these spurious hits from the dataset.

This chapter uses the simulation model for the HL-LHC and for its potential future upgrade: the HE-LHC, described in the previous chapter. The simulation studies aim at a better understanding of the influence of those upgrade projects on the levels of accelerator backgrounds at the ATLAS detector. The region of interest of the following background studies is the ATLAS interface plane (IFP), defined as a geometric plane perpendicular to the beam direction, located at the start of the experimental hall, 22.6 m upstream from the collision point. The studies include comparisons between various optics and geometry settings.

3.1 Motivation

During the LHC operation, non-collision backgrounds in the ATLAS experimental hall is monitored using the ATLAS detector subsystems and using dedicated radiation monitors. The radiation background levels must be closely monitored during data taking as it directly impacts the detector performance and data quality. The beam-induced background was studied during the LHC Run 1 [61], [62] using the results of the Beam Conditions Monitor (BCM) during Run 2 and using simulation studies for the HL-LHC [3]. An article

presenting the results from Run 2 with ATLAS detector responses to beam background is currently being prepared.

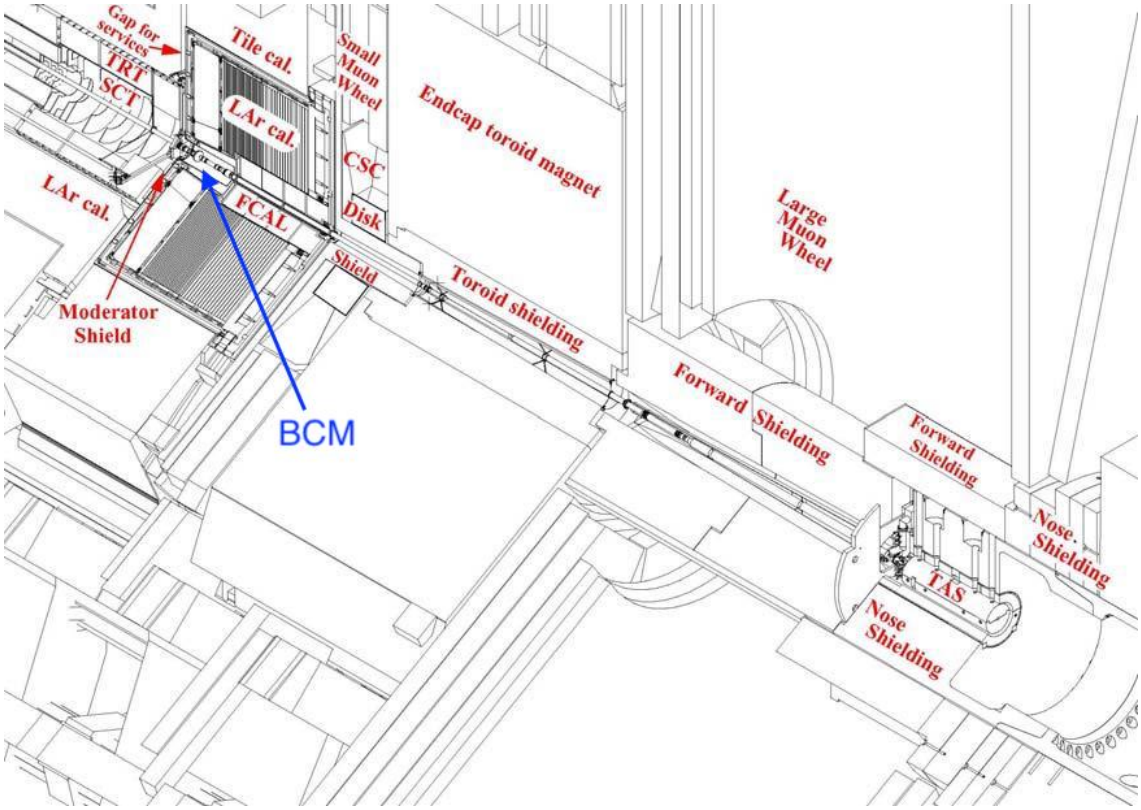

Figure 3.1: Detail of the beam line and nearby detector components and shielding elements inside the ATLAS detector [63] with the location of the BCM monitors.

To mitigate the impact of non-collision background, the ATLAS detector is heavily shielded by concrete and heavy-element absorbers. The detail of additional shielding inside the ATLAS detector is shown in Fig. 3.1. Despite the hall and tunnel shielding, the background radiation affects the detector in two ways. Firstly, beam background from beam halo, beam-gas or other sources travelling close to the beam line towards the centre of the ATLAS detector can cause large longitudinal clusters of energy deposition, especially in the pixel detectors close to the interaction point. These greatly increase detector occupancy, which, in turn, increases the dead time of front-end electronics. Due to its position near the beam pipe, the BCM can detect such background. The BCM detector serves to identify the backgrounds and tag runs with increased rates to be excluded from physics analyses. The rates of background hits measured by the BCM in LHC Run 2 in 2018 are shown in Figure 3.2 [64]. The average rate recorded by the BCM is $\sim 1\,\text{Hz}$ per bunch crossing.

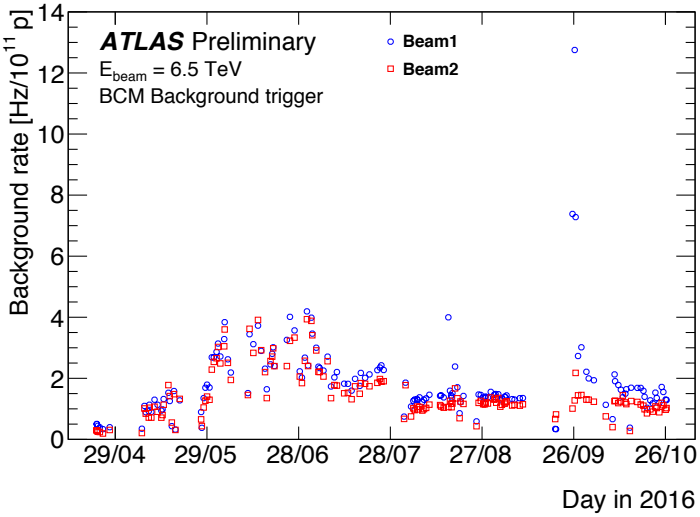

Figure 3.2: Rate of background radiation at ATLAS measured by the beam condition monitors during the proton-proton run in 2016.

Also, minimum interacting particles (e.g. muons) from NCB can deposit energy in the calorimeter and muon spectrometer, which could be reconstructed as a jet [1]. Fake jets negatively impact physics analyses which depend on measurements of missing transverse energy and jet identification. An example of fake jet reconstruction in Figure 3.3 shows jets in the Δt-η plane (time from collision as a function of pseudorapidity) in the LAr calorimeter for both LHC beams [61]. The plot shows the time relative to a collision of the leading jet from the A side (positive z) as a function of its pseudorapidity. This jet is easily identifiable based on the detection time (before the actual collision at $t = 0\,\mathrm{s}$). However, other such events can be occur in time with proton-proton collisions. Various sets of jet cleaning criteria are used to identify NCB, which appear in all jet analyses. The dedicated cleaning reduces the NCB contamination down to 0.5% [65].

The ATLAS interface plane is chosen as the event selection plane for the simulations in this chapter, because it is located just after the shielding material in the LHC tunnel. Therefore, particles reaching that plane are likely to reach the ATLAS detector subsystems. An exception is those particles stopped by the TAS, a secondary absorber inserted around the beam line inside the detector.

[1] A stream of particles produced when a quark or gluon is one of the outgoing particles created in the proton-proton collision at the interaction point.

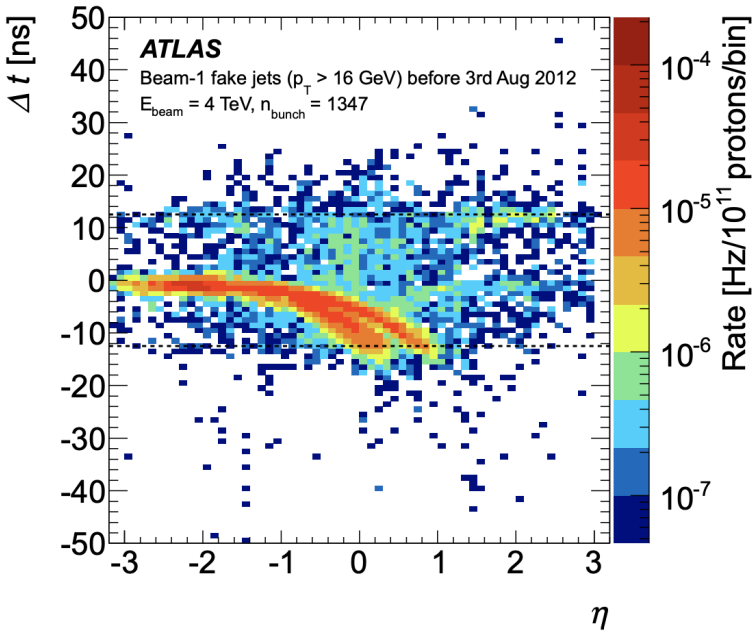

Figure 3.3: Beam-induced background fake-jet distribution in the Δt-η plane from beam 1 during a run from 2012 [61]. Δt is defined as time from collision.

3.2 Model and simulation preparation

3.2.1 HL-LHC IR 1 lattice optics

ATLAS is located in IR 1. The accelerator elements are shown in Figure 3.4. The machine diagram shows dipoles in blue, quadrupoles in red, black are passive elements such as collimators and absorbers, pink denotes kickers, and yellow represents the solenoid in the detector region. This section delivers the small β-value for the interaction point, generated by the quadrupole triplet located at $20-50$ m from the IP. After that, a pair of separation dipole magnets isolate the two beams into their separate beam pipes for the remainder of the matching section, dispersion section and arc.

The IR 1 is designed to prepare the beams for collisions at the ATLAS detector. The beam size and crossing angle should be as small as possible to achieve the highest luminosity. The primary optics parameters plotted from MADX optical parameters input file using python are shown in Fig. 3.5. The beam size is periodic in the arc and dispersion suppression section and then grows to reach its maximum of up to 2.7 mm in the triplet and the minimum of $\sim 7\,\mu$m at the collision point. The beam position is kept constantly at 0 throughout the arc and straight sections with respect to the optimal beam orbit on

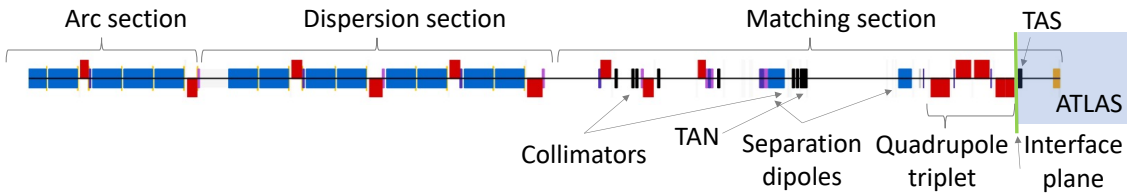

Figure 3.4: Accelerator lattice of the interaction region 1 leading to the ATLAS interaction point. Colours represent: blue - dipoles, red - quadrupoles, pink - kickers, black - collimators and absorbers, yellow - solenoid. Green line represents the simulated interface plane.

which it travels. In the last 150 m before the IP, the two beams share one beam pipe, so the centroid is offset in the x-plane to allow for collisions in the horizontal plane (different to the LHC, which collided the two beams in the vertical plane). The dispersion is minimised throughout the IR and equals 0 at the IP to ensure constant particle momentum during collisions.

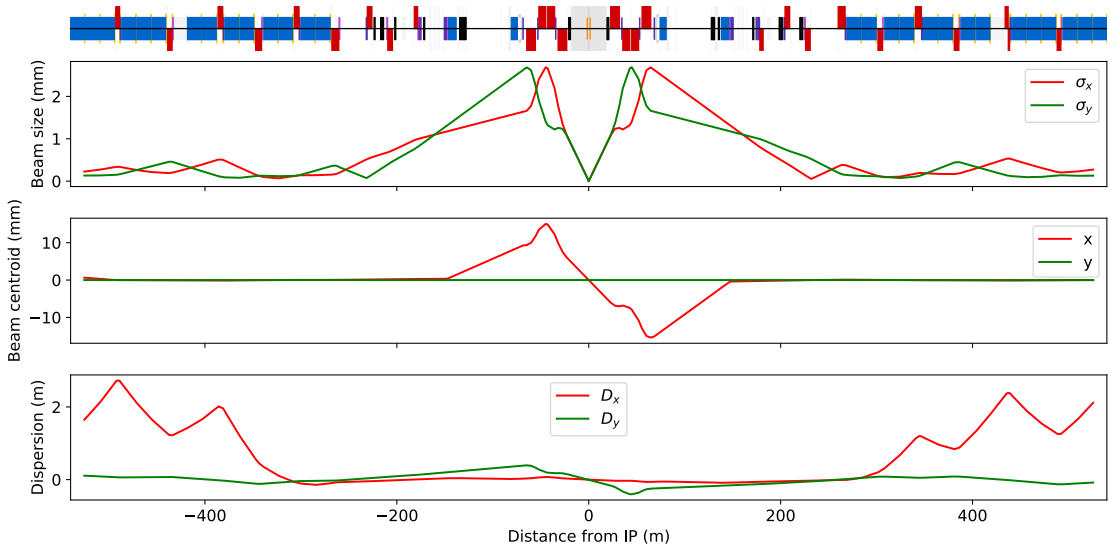

Figure 3.5: HL-LHC optics parameters (beam size, beam centroid and dispersion) for the optics settings v1.5 for $\beta^* = 15$ cm in IR 1. Plots were made in python using MADX input.

3.2.2 HE-LHC accelerator lattice optics

A complete model of the HE-LHC accelerator was generated for studies of beam halo losses in IR 7 and IR 1 and local beam gas backgrounds in IR 1. Beam halo losses are mainly produced in IR 7, the betatron cleaning section. Due to high losses in this region, only

warm magnets are used to prevent quenches. The collimator location, collimator family sequencing and phase advance between collimators are taken from the LHC design. The accelerator elements in IR 7 are shown in Figure 3.6.

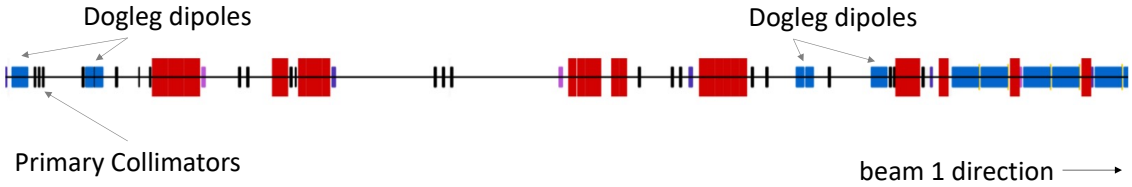

Figure 3.6: Accelerator lattice of the interaction region 7 for beam 1.

The principal optics parameters for IR 7, including the dispersion suppression section and the start of the arc, are shown in Fig. 3.7. The beam size changes throughout the section and oscillates between the collimator families. The beam centroid shows the offset created by the separation dipoles for a 10 mm offset. The horizontal dispersion is equal to 0 at the primary collimator location but then starts to oscillate. The vertical component of the dispersion is 0 throughout the section.

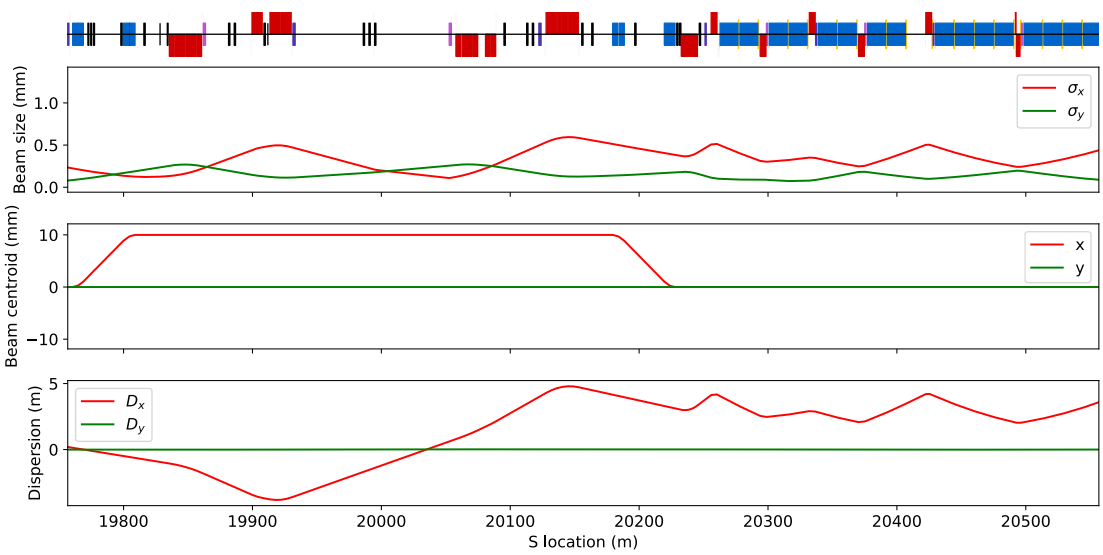

Figure 3.7: HE-LHC optics parameters (beam size, phase advance and dispersion) in IR 7 for optics with a 10 mm dog-leg offset.

The HE-LHC collimation system is based on the LHC and HL-LHC designs with momentum cleaning in IR 3 and betatron cleaning in IR 7. However, the section was reviewed to search for available space due to the size of new dipoles and additional accelerator

elements. The dispersion section in IR 7 includes two dog-leg sections, which increase the beam separation inside the straight section from 194 mm to 224 mm in the case of LHC to accommodate wider elements. The beam separation in the HE-LHC in the arc section is set to 250 mm, which raises the question of the necessity of the dog-leg magnets.

The main beam parameters are summarized in Table 3.1, with most optics parameters following the LHC settings. The biggest differences are doubling the beam energy and larger inter-beam distance due to the larger sizes of beamline elements.

Table 3.1: HE-LHC collimator settings for the primary, secondary and tertiary collimators of beam 1 using the collision energy settings.

Beam energy	13.5 TeV	RMS emittance	2.5 μm
Inter-beam distance	250 mm	Bunch spacing	25 ns
Particles per bunch	2.2×10^{11}	IP beta function $\beta^{\star}_{x,y}$	45 cm

The main collimator settings for both potential injection energies and top energy are summarized in Table 3.2. These settings were taken from the baseline settings of the HL-LHC collimation with optics v1.3. To this day, injection energy is not yet decided so settings for both LHC injection energy 450 GeV and upgraded HE-LHC injection energy 1.3 TeV are shown.

Table 3.2: HE-LHC collimator settings in σ for collision and injection energies for the main families of collimators. All beam RMS sizes (σ) for a reference emittance of 2.5 μm.

Collimators \ Energy	450 GeV	1.3 TeV	13.5 TeV
Primary collimator (TCP) (σ)	5.7	9.7	6.7
Secondary collimator (TCS) (σ)	6.7	11.4	9.1
Tertiary collimator (TCT) (σ)	13.0	22.1	10.5
Active absorber (TCLA) (σ)	9.0	15.3	11.5
Dump protection (TCDQ) (σ)	8.0	13.6	10.1

Dog-leg offsets were selected for the simulation to be 0 mm (for no offset), 10 mm and 20 mm for comparison of background differences. All three of these are physically possible, but a 0 mm offset would remove the need for the dipole dog-leg dipoles and free up to 16 m space for additional components. A plot of the orbit offset of the beam travelling through the dog-leg section is shown in Fig. 3.8.

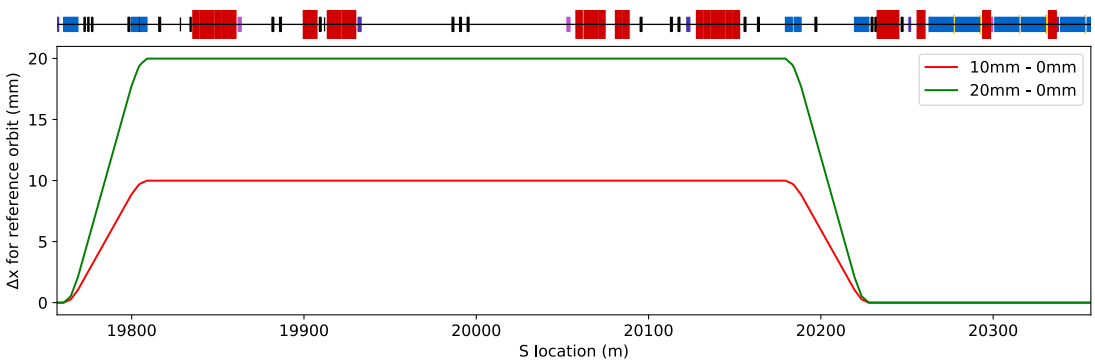

Figure 3.8: Δx for reference orbit of the beams with an offset of 20 mm and 10 mm compared to 0 mm in the HE-LHC IR 7.

3.2.3 HL-LHC beam-gas simulation setup

Local beam-gas interactions were simulated in the region of IR 1 to study the background propagation and particle spectra at the ATLAS interface plane. The simulation aimed to accurately portray the accelerator elements with magnetic fields, aperture size and material while also including the tunnel, caverns and other shielding elements. With these parameters in mind, the BDSIM software was used for this simulation. A beam distribution with HL-LHC parameters was generated and propagated through IR 1 with gas particles present in the beam pipe according to vacuum pressure studies [61]. The cross-section of the interactions between the primary protons and the gas was biased to achieve high statistics and a flat primary hit distribution.

Beam-gas simulations were run with 20 MeV kinetic energy cut using single element gas profile with biasing ensuring flat distribution. All results used a minimum of 2.5×10^6 primary proton interactions with gas particles. All simulations were generated starting as many single primary particle simulations, which were then added and scaled per single beam-gas interaction. Each beam-gas interaction cascades, producing multiple secondary particles at the interface plane. Additional scaling was used to achieve results per proton bunch per unit time using equation 1.42 with operational and vacuum conditions specific for each simulation. HL-LHC plans to use 2.2×10^{11} protons per bunch with 25 ns bunch spacing. Every few bunches, there are gaps (used for dump kickers to charge) leading to collision bunch frequency of 3×10^7 Hz.

3.2.4 HL-LHC beam halo simulation setup

A Sixtrack simulation was used to study impacts on tertiary collimators (TCTs) in IR 1 originating from primary impacts on primary collimators (TCPs) in IR 7. The Sixtrack simulation results were kindly provided by Bjorn Lindstrom from the HL-LHC collimation team. The ratios of tertiary impacts per primary collimator hit for the simulation cases are summarised in Table 3.3.

Table 3.3: Number of simulated primary hits and the ratio of tertiary/primary hits for IP 1.

Beam direction	β^*(cm)	Simulated primary impacts	TCT impacts per TCP hit
IP 1 beam 1	15	40×10^6	4.49×10^{-4}
IP 1 beam 2	15	40×10^6	1.21×10^{-3}
IP 1 beam 1	20	200×10^6	2.58×10^{-4}
IP 1 beam 2	20	800×10^6	1.32×10^{-5}
IP 1 beam 1	64	192×10^6	4.49×10^{-5}
IP 1 beam 1	100	200×10^6	1.31×10^{-5}

An example of impact hits on a collimator in IR 1 and the energy distribution of the hits are shown in Fig. 3.9. The tertiary halo impacts are distributed on the face and along the jaws of the horizontal collimator. The angles in x at the face of the collimator are due to the sloped collimator geometry. The energy distribution shows that the primary halo that impacts on the collimator maintains more than 99% of the design beam energy. All hits distributions and their energy spread on TCTs in IR 1 (beam 1 for $\beta^* = 15, 20, 64, 100$ cm and beam 2 for $\beta^* = 15, 20$ cm) and IR 5 (beams 1 and 2 with $\beta^* = 15, 20$ cm) are shown in Appendix A.

Sixtrack can efficiently generate primary loss maps. However, it does not simulate secondary particles. The coordinates and momentum of the simulated primaries at the point of interaction identified by SixTrack are then used by other simulation packages capable of particle-matter interactions with tracking of secondaries. BDSIM simulation software was selected to propagate secondaries between the tertiary collimators and the interface plane of ATLAS.

With BDSIM, all simulations are generated starting with many single primary particle simulations, which are then added and scaled to the number of tertiary collimator hits. Calculating the ratio of tertiary/primary collimator hits and using the beam lifetime, results were also scaled to the nominal proton bunch crossing rate during regular operation.

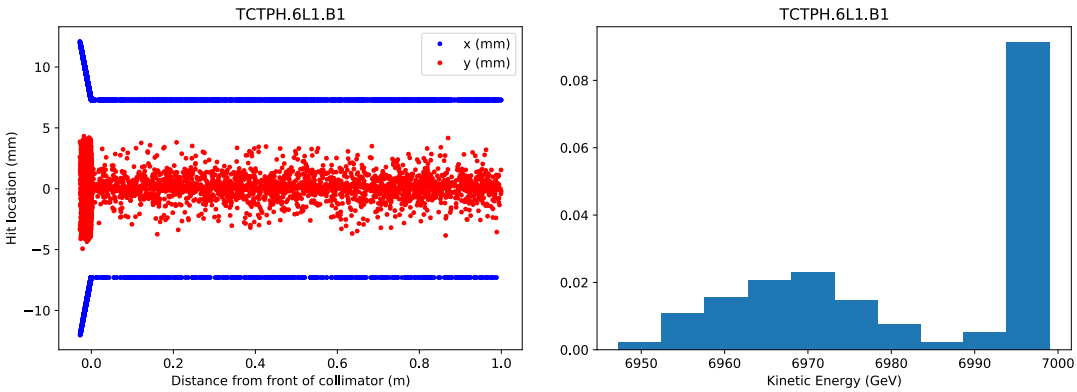

Figure 3.9: Impact hits on a TCT (TCTPH.6L1.B1) in IR 1, beam 1 (left) and their energy distribution (right) created from 200M TCP hits using HL-LHC Sixtrack simulation results for $\beta^* = 20\,\text{cm}$.

3.2.5 HE-LHC beam halo simulation setup

Beam halo background was generated in the full accelerator of HE-LHC to study the dependence of beam losses in IR 7 and beam background radiation in IR 1 on the dog-leg offset. BDSIM results are then compared with previous results from similar simulation studies performed using FLUKA [66]. The BDSIM simulation uses hits in the IR 7 primary collimator as primary particles, using an input beam profile such that all primaries impinge on the TCP with an impact parameter up to $\sim 3\,\mu\text{m}$ (beam input shown in Fig. 3.10). The impact parameter of BDSIM simulations was tuned to maximise the beam penetration down in the lattice. A small impact parameter can propagate further down the lattice than a larger impact parameter [67]. A kinetic energy cut of 1 GeV is used, and the simulation runs for 200 turns of the HE-LHC circular lattice.

All simulations are scaled with the same parameters as HL-LHC beam halo simulations, because the foreseen HE-LHC operation parameters are unknown at the time of writing.

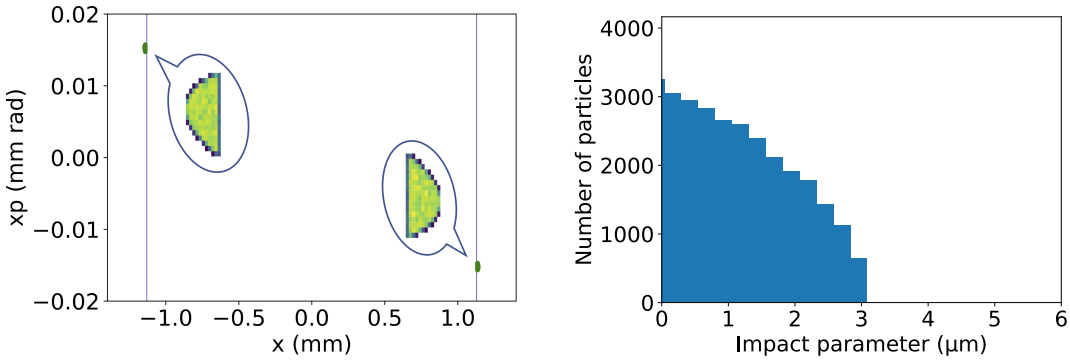

Figure 3.10: Horizontal halo impacting on the first horizontal primary collimator in IR 7 of the HE-LHC. Left plot shows the impact of the beam ellipse on the collimator jaws (blue lines). Right plot the number of particles hitting the collimator.

3.3 Results of beam-gas studies for HL-LHC

Simulation results are presented at the ATLAS interface plane for the most recent optics version v1.5 of the HL-LHC with comparisons to previous version v1.0 and using v1.4 for TAN geometry comparison studies.

3.3.1 HL-LHC BDSIM/FLUKA comparison v1.0

The first studies of beam background for the HL-LHC were performed using the original baseline optics version (v1.0) [1, 68], and these results are compared with BDSIM. The v1.0 optics use the 2013 IR 1 layout version with 7 TeV beam energy and $\beta^* = 15\,\text{cm}$. The tertiary collimators in IP 1 (one vertical and one horizontal collimator) are placed in the 4th cell (131.8 m and 133.5 m) from the IP and are set to their nominal setting - $8.3\,\sigma$. The TAN uses a simplified geometry with parallel beam chambers. Additional concrete shielding blocks in IR 1 are also not used. For beam-gas simulations, only interactions between the ATLAS detector and the TAN ($\sim 130\,\text{m}$) are considered since the matching section layout was not yet defined at the time.

A flat pressure profile is used in the last 150 m before the IP to ensure a uniform density of primary interactions with hydrogen gas. A more realistic vacuum pressure profile was not available for HL-LHC optics at the release time of FLUKA simulation studies. Both FLUKA and BDSIM spatial distributions of beam-gas interactions are shown in Figure 3.11 normalized to unity. The FLUKA distribution shows a few spikes at the location of the separation magnets (approximately at $-140\,\text{m}$ and $-80\,\text{m}$). The BDSIM simulation is very

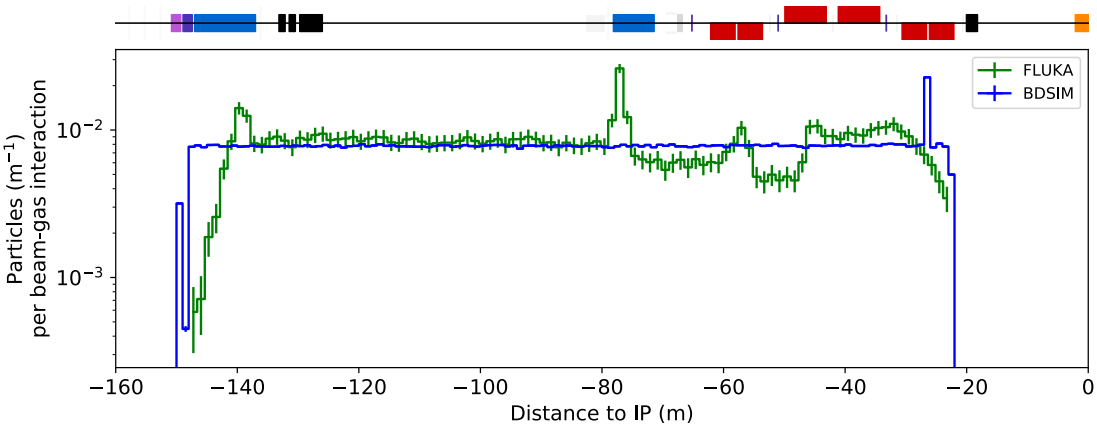

Figure 3.11: Origin of primary interactions with hydrogen gas for secondary production at the interface plane.

flat with a single spike at the location of the final focusing quadrupole magnet closest to the IP.

The energy spectra of various secondaries are shown in Fig. 3.12. BDSIM and FLUKA show a comparable level of secondaries at the interface plane with only minor differences in distribution. For protons, the energy spectrum has the same shape with a small peak in BDSIM at 100 GeV. FLUKA estimates a larger proton production at 5 TeV. BDSIM estimates a smaller production of protons at small radii and more for radii larger than 2 m. The neutron kinetic energy spectra are comparable for both simulations, while in spatial distribution BDSIM also scores more particles for larger radii. Muon spectra are similar in both kinetic energy and spatial distributions for both BDSIM and FLUKA simulations.

3.3.2 HL-LHC v1.5 default optics

The current most up-to-date optics version of the HL-LHC is the v1.5, which became available in 2021. Updated collimator settings were later established in 2022. Table 3.4 shows the evolution of the collimator settings. In v1.5, updated geometry of beamline components (TAN, TAS, shielding blocks) is used, as well as a detailed geometry of the tunnel and surroundings of the ATLAS experimental hall. There are two sets of tertiary collimators (a set consisting of a vertical and a horizontal collimator) in IR 1 located at 212 m and 132 m from the interaction point.

The two beams are prepared for collisions at approximately 200 m before the ATLAS

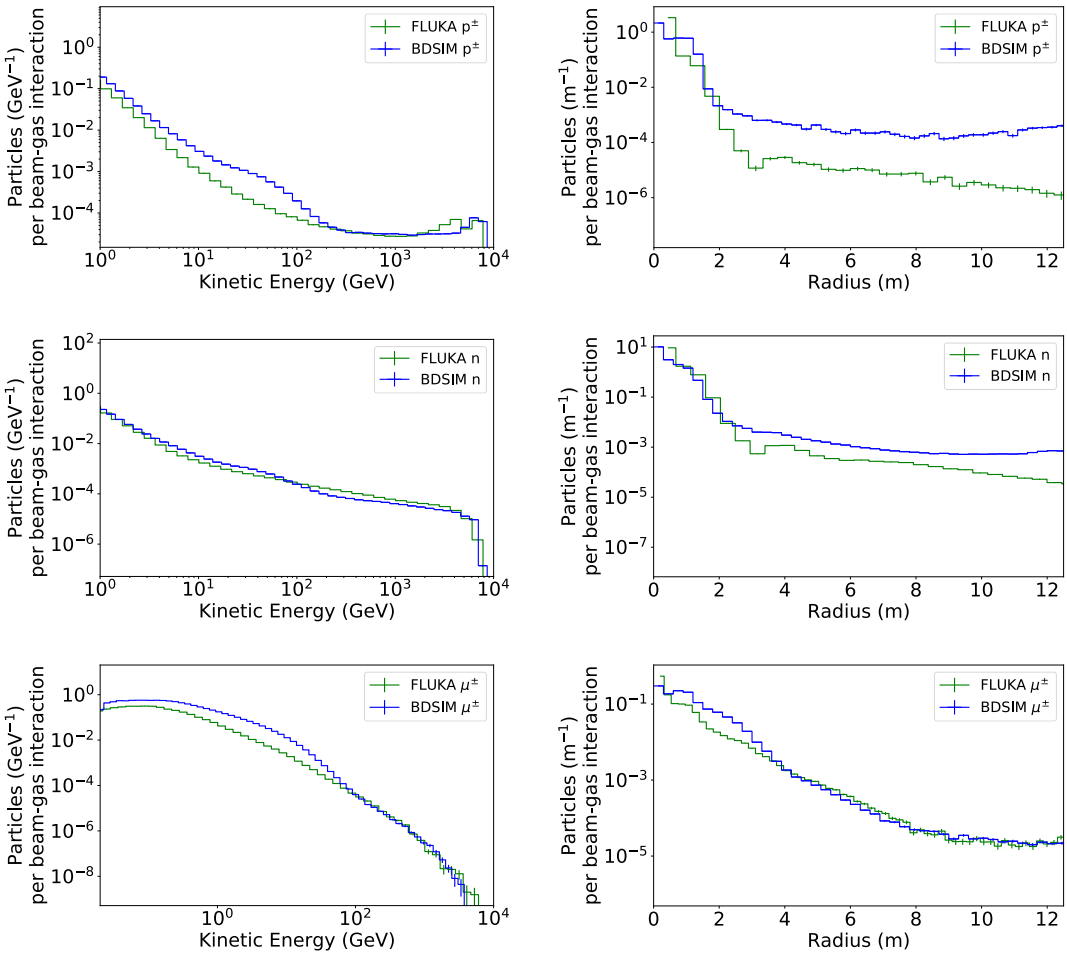

Figure 3.12: Energy (left) and radial spatial (right) distributions of secondary protons (top), neutrons (middle) and muons (bottom) at the the ATLAS interface plane for BDSIM and FLUKA.

Table 3.4: HL-LHC collimator settings in number of sigma of the beam size for collision energy for primary, secondary and tertiary collimators for different optics versions.

Collimator	v1.0	v1.3	v1.5
TCP IR 7	6.0	6.7	8.5
TCS IR 7	7.0	9.1	10.1
TCT IR 1	8.3	10.4	11.4

interaction point. The kickers deflect and align the beams in the horizontal plane to assume the chosen crossing angle. The beam changes size throughout the straight section in the vertical plane but remains centred. The progress is shown in Figure 3.13, where the location of primary interactions with gas particles in the horizontal and vertical planes outline the beam size and trajectory throughout the section. In previous versions and the current

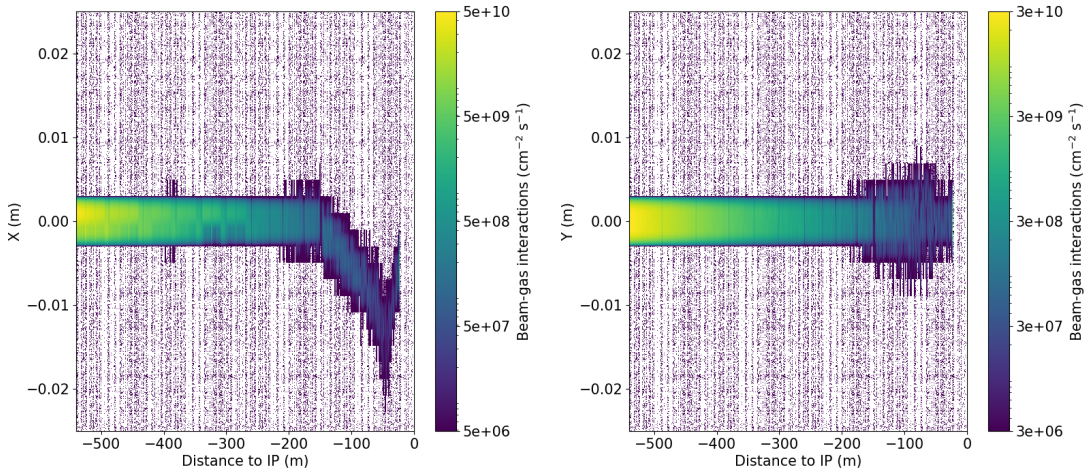

Figure 3.13: Origin of primary interactions with oxygen gas in horizontal (left) and vertical (right) planes for HL-LHC optics v1.5 with $\beta^* = 15\,\text{cm}$.

operation of the LHC, the beams collided in the vertical plane instead.

Figure 3.14 shows the spatial distributions of inelastic primary interactions that produce secondary particles at the interface plane. The number of particles increases between the arc and interface plane. The number of particles produced increases exponentially between the TAN and the interface plane.

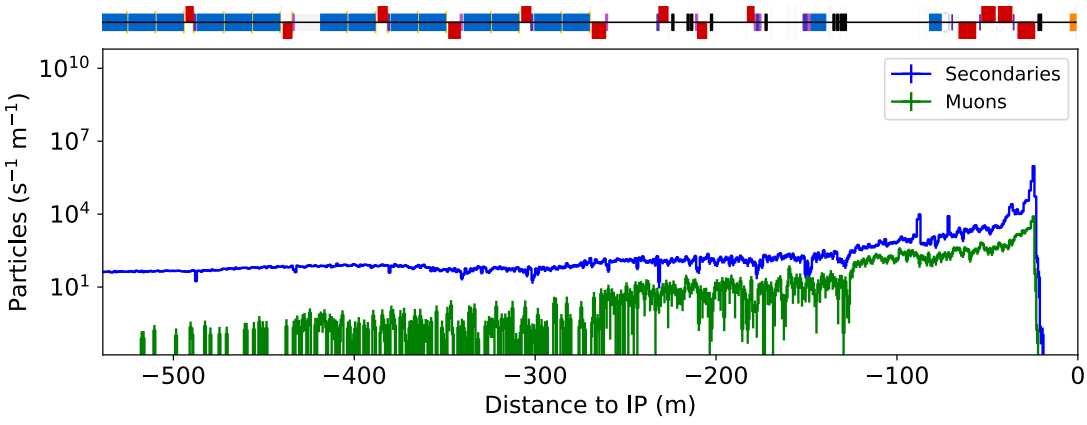

Figure 3.14: Origin of primary interaction for beam-gas for all secondary particles and muons at the interface plane for HL-LHC optics v1.5.

Distributions of the energy, the azimuth (scaled by the kinetic energy of each particle) and radius (also scaled by energy) of secondary particles at the ATLAS IFP are shown in Figure 3.15. The energy distribution shows that most secondaries at the interface plane

have low energy ($< 1\,\text{GeV}$). A high number of protons have energies up to the beam energy, which is caused by elastic scattering of primary protons with gas particles. Such protons keep up to 100 % of their energy and momentum, but are classified as secondary protons. The azimuthal distributions show peaks at $\phi = \pm\pi/2$ with higher energy contribution in the negative ϕ; the particles are spread in the vertical plane. The radial distribution figure shows most secondaries are located inside and near the beam pipe and decrease in number for higher radius (reduced by the tunnel wall shielding). For larger radii (R$>$ 1 m), the most significant contribution comes from muons, due to their ability to propagate further in material.

The effects of different β^* settings on beam-induced background were studied with optics parameters using $\beta^* = 15\,\text{cm}$, $\beta^* = 25\,\text{cm}$ and $\beta^* = 40\,\text{cm}$. These optics parameters are part of the low β^* program at ATLAS. The variations in beam size for the three different settings are shown in Fig. 3.16, showing the horizontal and vertical beam size components. The optics with $\beta^* = 15\,\text{cm}$ produce the largest beam size in the triplet region. During runs with larger β^* settings, beams have a smaller maximum size by a factor of 1.3 and 1.6 for $\beta^* = 25\,\text{cm}$ and $\beta^* = 40\,\text{cm}$ respectively. Even for such large differences, the beam sizes are still very small compared to the aperture of beam elements in this section (up to 10 cm diameter). Therefore, the background differences for these settings should only differ due to quadrupole field strengths and not be related to collimator sizes.

For different β^* optics, the origin of the primary interaction with gas is shown in Figure 3.17. The location of the origin beam-gas interaction is the same for all three cases. A small contribution comes from the arc and the dispersion suppression section. In the straight section, the number of secondaries reaching the interface plane grows by up to four orders of magnitude.

The azimuthal distribution for all secondary particles and muons is shown in Figure 3.18. The distributions have peaks at $\phi = \pm\pi/2$ and display only minimal differences for the three β^* settings. For all secondary particles, the rise in azimuthal distribution is larger at $\phi = \pi/2$ while more muons are present at $\phi = -\pi/2$.

In conclusion, varying the β^* value does not affect the background radiation levels at the ATLAS interface plane for a beam-gas background source. This is expected as the beam only differs in size. The beam size is always small enough to traverse the section without impinging on the aperture or collimator jaws.

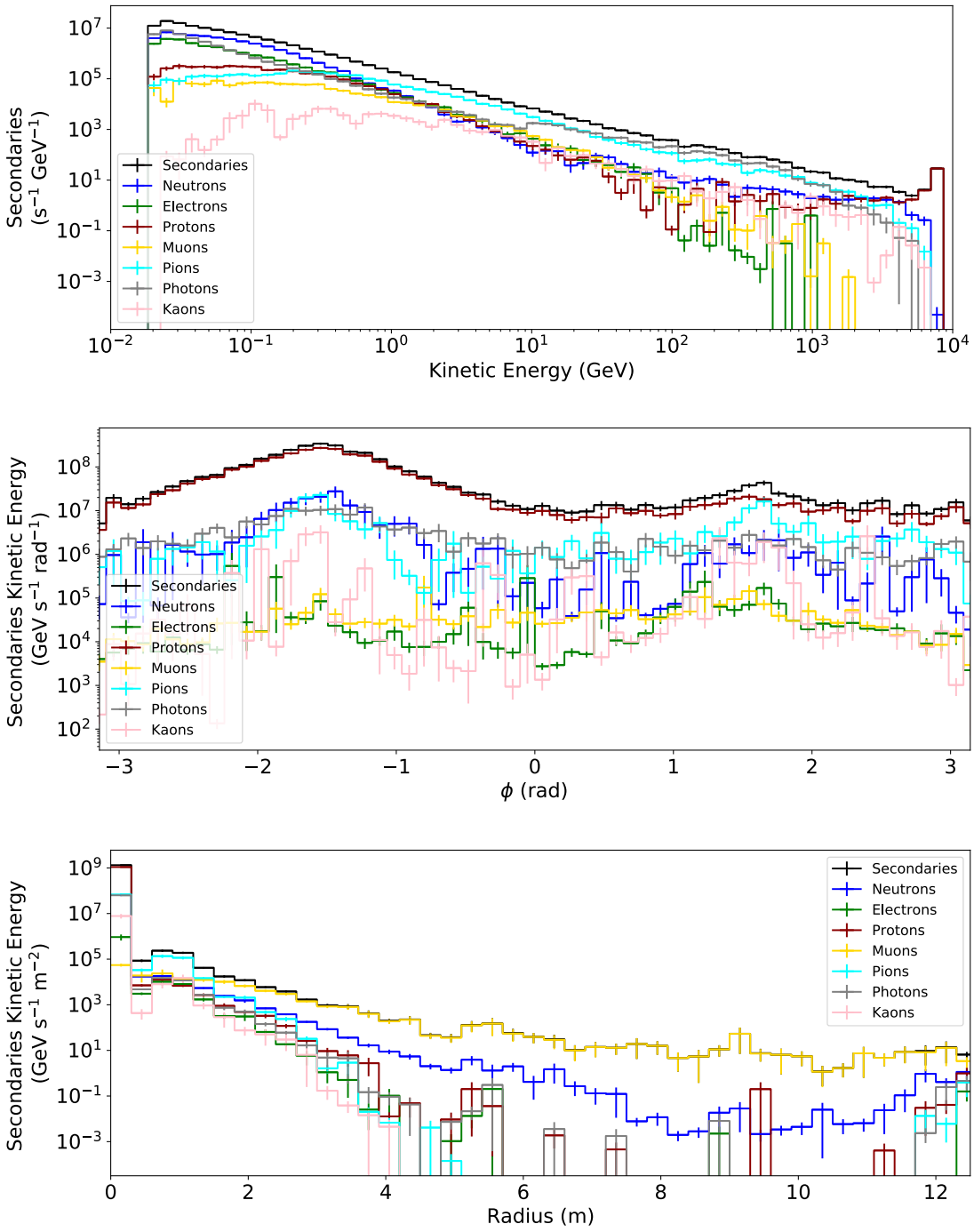

Figure 3.15: Energy (top), and energy-scaled azimuthal (middle) and energy-scaled radial (bottom) distributions for most abundant secondary particles at the ATLAS interface plane for HL-LHC using the default collision optics of v1.5.

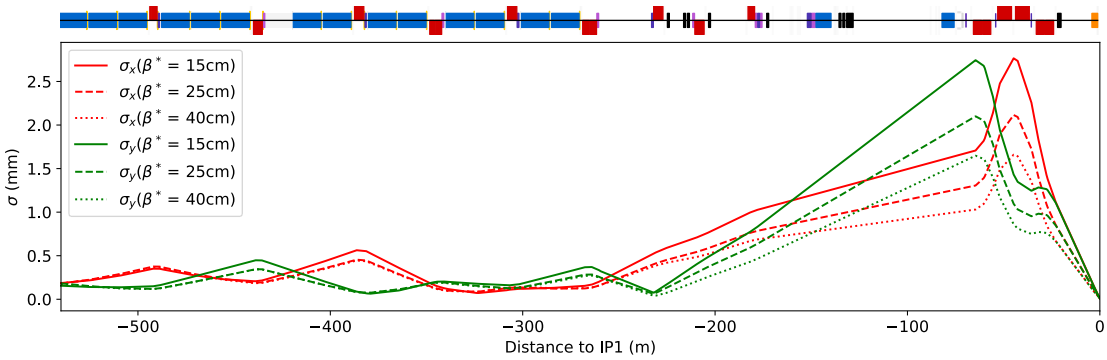

Figure 3.16: Beam size in IR 1 for the HL-LHC optics settings v1.5 for β^* of 15, 25 and 40 cm.

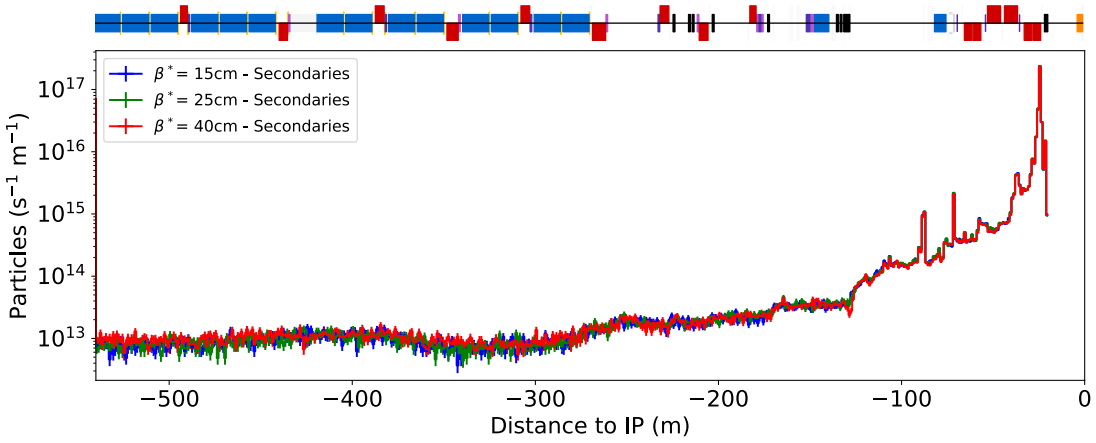

Figure 3.17: Origin of primary interactions with hydrogen gas in IR 1 of HL-LHC optics v1.5 for secondary production at the ATLAS interface plane for different β^*.

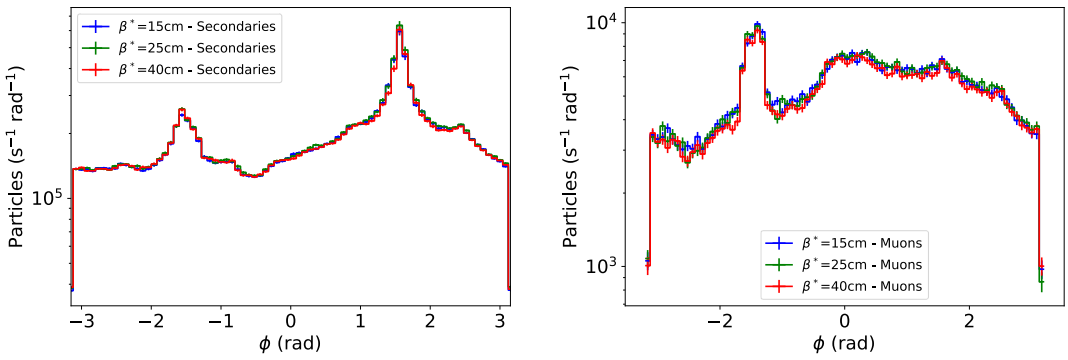

Figure 3.18: Azimuthal spectra for all secondary particles and muons as a function of ϕ at the interface plane for different β^*.

3.3.3 HL-LHC comparison of v1.0 and v1.5

The newest optics settings of v1.5 effectively lower the beam-induced background at the ATLAS interface plane compared to v1.0 by adding a second set of collimators. The origin of primary interactions producing secondary particles and muons specifically at the interface plane is compared for both optics versions in Figure 3.19. The various concrete shielding blocs and updated TAN geometry were included in the v1.0 so that only optics changes can be compared. Both simulations used the same uniform vacuum density.

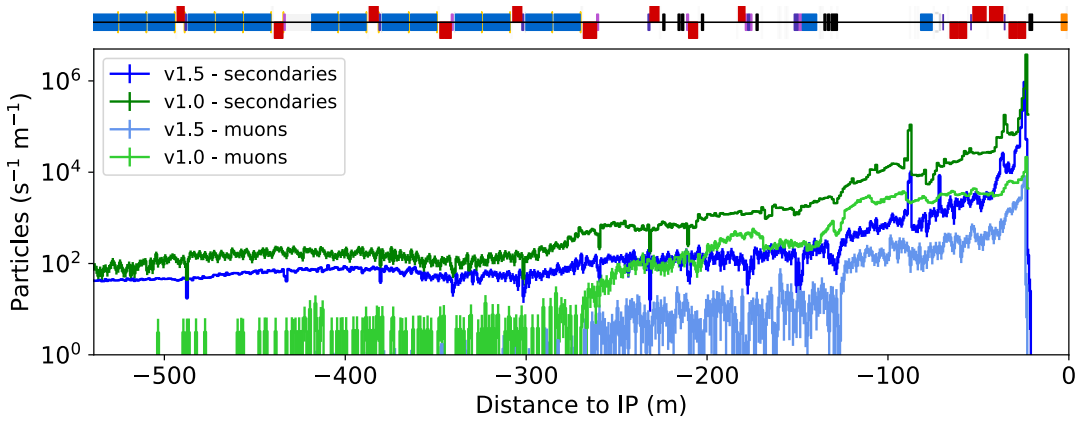

Figure 3.19: Origin of primary interactions with hydrogen gas for secondary particles passing through the ATLAS interface plane for HL-LHC optics versions 1.5 and 1.0.

The azimuthal and radial spatial distributions of all secondary particles and muons scaled by the energy of the particles are shown in Figure 3.20. The simulated background radiation obtained using the v1.0 and v1.5 configurations display similar shapes for both angular and radial distributions. All secondary particles are concentrated in $\phi = \pm\pi/2$, and the number of particles drops sharply with increasing radius.

The changes to the optics in IR 1 between versions 1.0 and 1.5 reduced the beam background at the ATLAS interface plane originating from beam-gas interactions by one order of magnitude.

3.3.4 HL-LHC TAN geometry studies

Studies were performed in order to quantify the effects of reducing material in the neutral beam absorber (TAN) on background radiation levels at the ATLAS interface plane for use during HL-LHC operation. The TAN is required to absorb the flux of forward going high energy neutral particles produced at the collision point of ATLAS protecting the

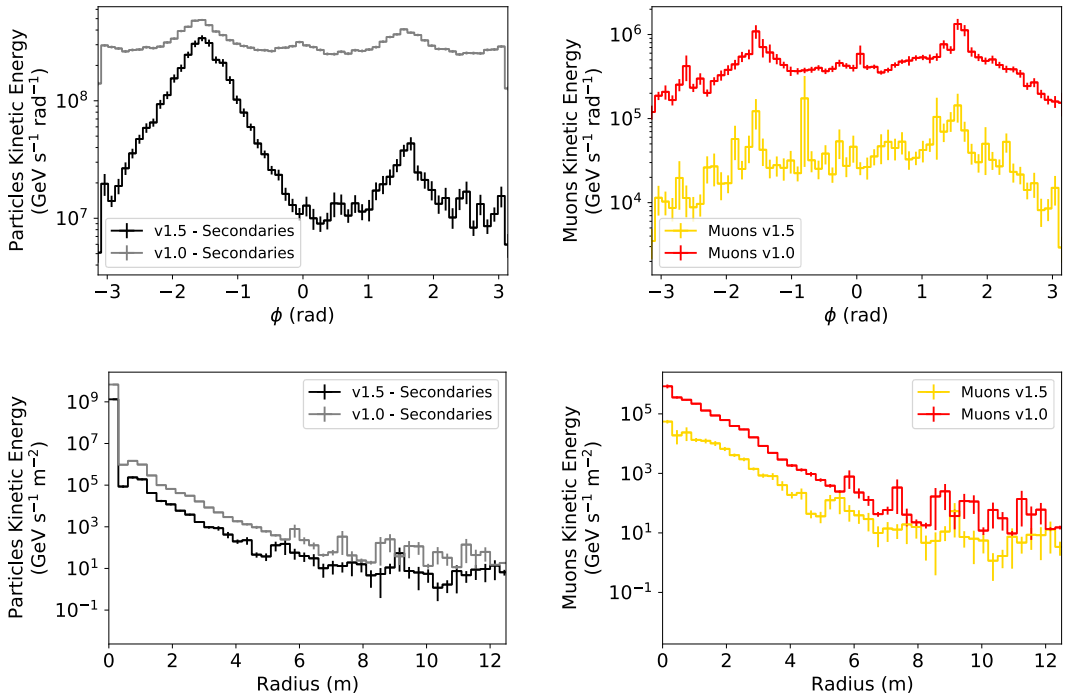

Figure 3.20: Azimuthal (top) and radial (bottom) spatial distributions for secondary particles (left) and muons (right) scaled by the particles kinetic energy at the ATLAS interface plane for HL-LHC optics versions 1.5 and 1.0.

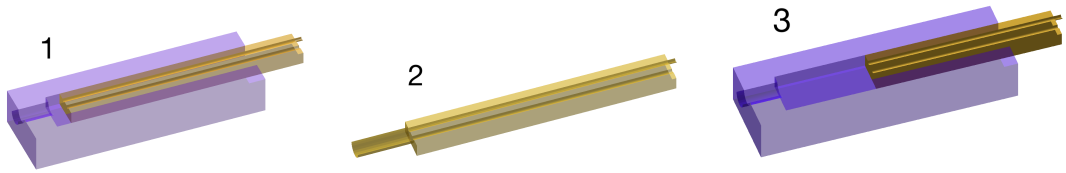

Figure 3.21: Simulated TAN geometries - integral design (#1), without outer shielding (#2), with shorter inner absorber (#3). Yellow colour represents the inner absorber, purple is the outer shielding.

second beam separation dipoles (D2). This simulation looked at the effect of the TAN in decreasing beam background reaching IP 1. Three foreseen TAN geometries shown in Figure 3.21 that vary in manufacturing complexity and costs were discussed. Case #1 is the original TAN design, including an inner copper absorber and outer iron shielding, case #2 is missing the outer iron shielding, and case #3 has a shorter inner copper absorber length by 1 m. These studies were done using the HL-LHC optics v1.4 with beam-gas interactions in the last 540 m before IP 1.

Figure 3.22 shows the location of origin of secondaries for the three cases. The second

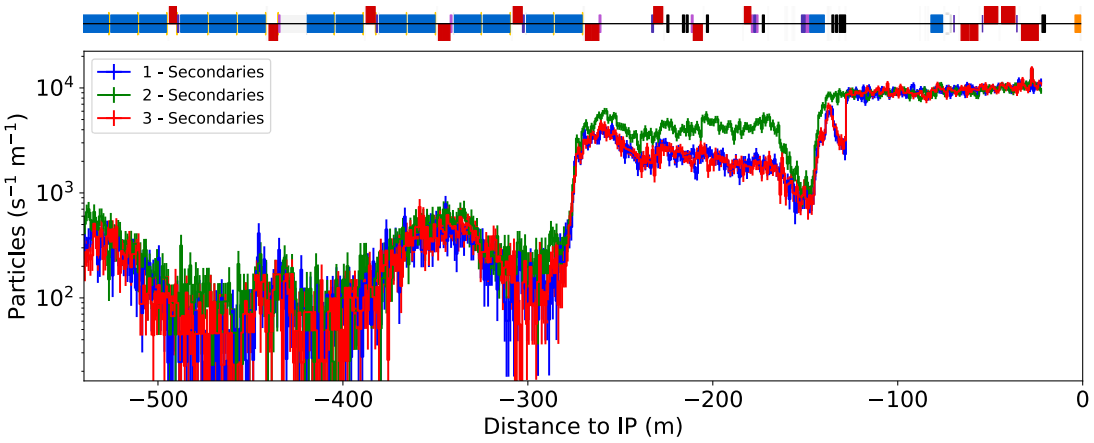

Figure 3.22: Origin of primary interactions with hydrogen gas for secondary particles passing through the ATLAS interface plane for different TAN geometries.

case shows an increase in secondaries between 250 and 150 m in front of the IP compared to the other geometries. The increase is explained by the missing shielding layer, which allows more background particles to propagate around the TAN.

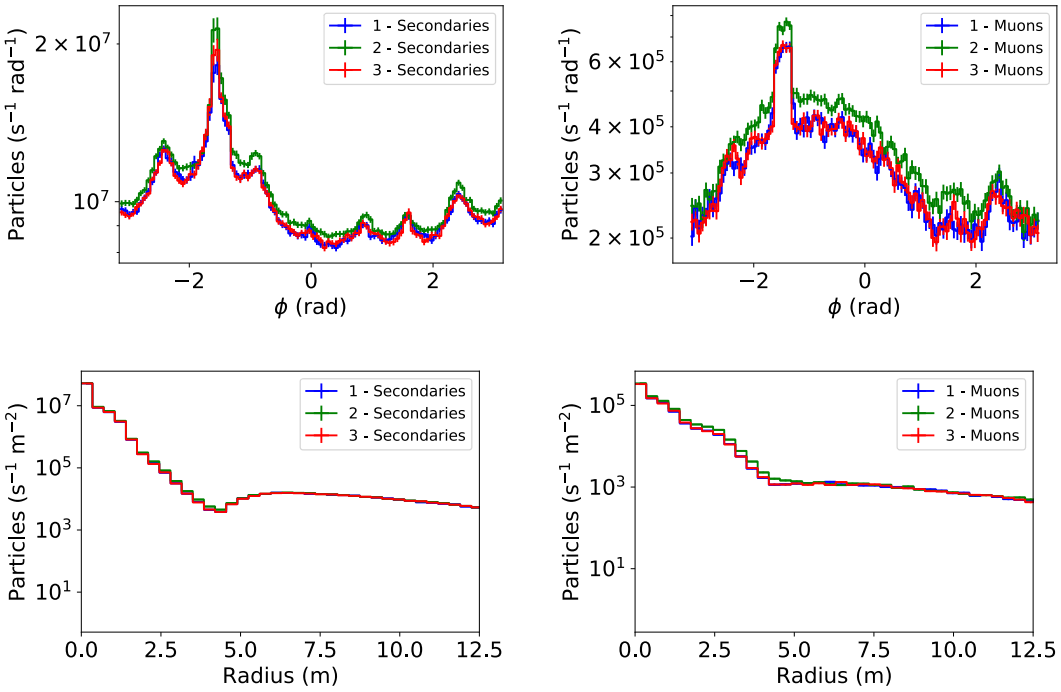

Figure 3.23: Azimuthal (top) and radial (bottom) distributions for secondary particles (left) and muons (right) passing through the ATLAS interface plane for different TAN geometries.

Comparing the spatial distributions of all secondary particles and muons in azimuthal and radial coordinates, shown in Fig. 3.23, we can conclude that the three geometry cases are similar in the spatial distribution of background radiation rate levels with a slight increase in the level of particles produced by the geometry scenario with no outer shielding. Azimuthal distributions show a larger background contribution in negative ϕ with a peak at $-\phi/2$. The number of background particles decreases with increasing distance from the beam pipe.

To conclude, the geometry differences in the TAN designs have minor effects on the amount of beam background at the ATLAS interface plane. The worst case is the TAN absorber without the outer shielding (case #2), which allows background radiation with a larger radius to pass near the beam line without being absorbed in the iron shielding.

3.3.5 Comparison between HL-LHC v1.5 and LHC Run 2 optics

The studies of background radiation propagation near the IP 1 during HL-LHC operations were compared to the simulated LHC Run 2 background levels. In order to compare changes due to optics differences, both simulations were scaled using the design parameters for the HL-LHC operation presented in Table 1.1. The number of protons in a bunch, as well as the overall number of bunches, will increase for HL-LHC compared to the LHC. However, the interaction probability density of a specific gas depends on the vacuum density profile, which is not yet determined for HL-LHC. Therefore, a density value of 10^{13} molecules/m^3 of H_2 gas is assumed, corresponding to Run 2 conditions. However, the vacuum system will be updated in the Long Shutdown 3, and this value is expected to decrease.

The vertex position of the inelastic interaction of primary particles at the interface plane is compared for both simulations in Figure 3.24. The distributions are comparable with the main differences between 250 and 100 m before the IP, where the LHC settings produce more background radiation.

The azimuthal and radial spatial distributions for secondary particles are shown in Figure 3.25. The levels of background are equal in both scenarios. The azimuthal distribution of secondary particles shows a shift of the peaks from $\phi = 0, \pm\pi$ in the LHC case to $\phi = \pm\pi/2$ in the HL-LHC case, which can be explained by the change in orientation of the collision plane from vertical to horizontal.

To conclude, HL-LHC background levels originating from beam-gas interactions are

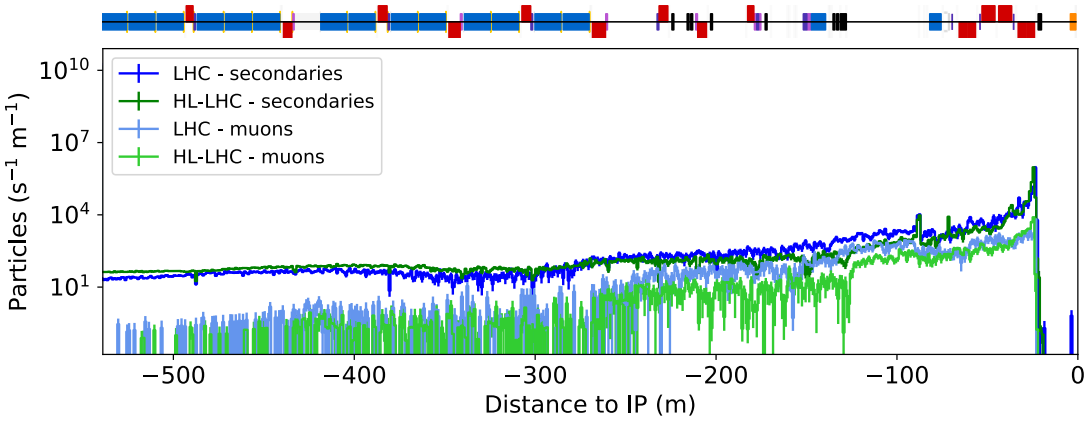

Figure 3.24: Location of the origin of secondary particles passing through the ATLAS interface plane for HL-LHC and LHC optics.

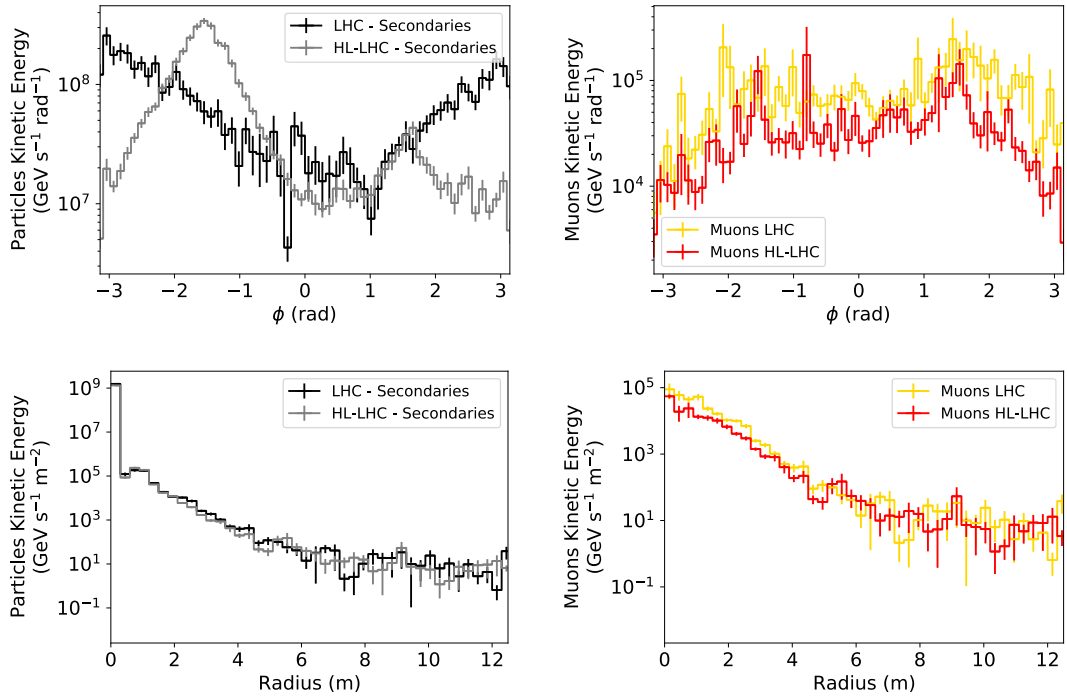

Figure 3.25: Azimuthal (top) and radial (bottom) distributions for secondary particles (left) and muons (right) at the ATLAS Interface Plane for HL-LHC and LHC optics.

comparable to the LHC Run 2 simulation results of the same beam intensity. The azimuthal spatial distribution of background radiation at the interface plane has its maximum moving from the horizontal plane to the vertical plane.

3.4 Beam halo studies for HL-LHC and HE-LHC

Simulation results are presented at the ATLAS interface plane for the most recent optics version of the HL-LHC (v1.5) and for different β^* optics. Results specific to HE-LHC also include losses in IR 7.

3.4.1 HL-LHC IP 1 beam 1 results

This study presents the impact of the tertiary halo from beam 1 at the ATLAS interface plane for optics v1.5. The smallest β^* setting was studied with the optics settings corresponding to $\beta^* = 15\,\text{cm}$, for which we expect the highest background rates as this configuration corresponds to the largest beam diameter foreseen during HL-LHC operations. Comparisons of optics models with $\beta^* = 20\,\text{cm}$ and $100\,\text{cm}$ are also presented.

Results are normalized to one second of nominal operation assuming an optimistic beam cleaning design with a lifetime of 100 hours. In the critical scenario, the minimum beam lifetime capable of not damaging any accelerator component in the HL-LHC is 12 minutes, which would scale up the optimistic scenario simulation results by an additional factor of $\sim 10^3$.

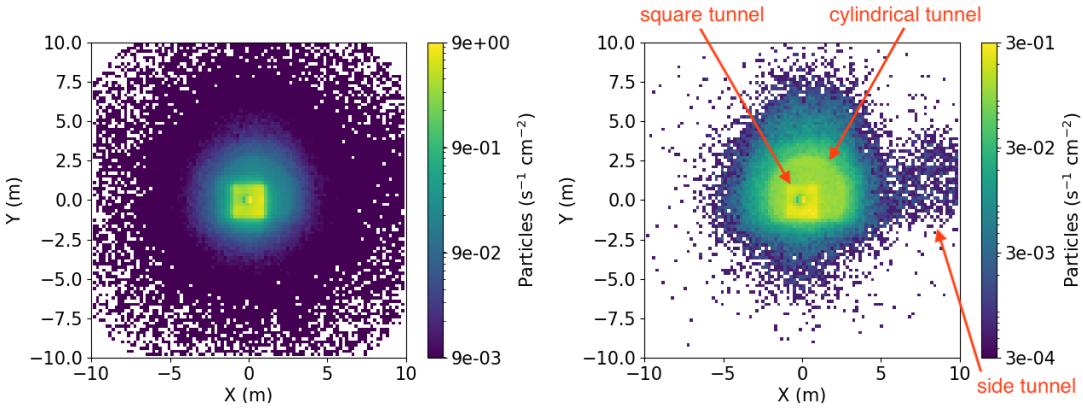

Figure 3.26: Fluence of secondary particles (left) and muons (right) reaching the interface plane from beam halo origin for HL-LHC v1.5 optics with $\beta^* = 15\,\text{cm}$.

The fluence of all secondaries and muons is shown in Fig. 3.26. The flux of all secondary particles shows the outline of the square tunnel near the ATLAS cavern and the fainter outline of the cylindrical LHC tunnel in the background with particles concentrated on the positive x side. The muon fluence also shows the tunnel outlines and has a more considerable decrease of particles for a larger radius. The side tunnel outline is also visible.

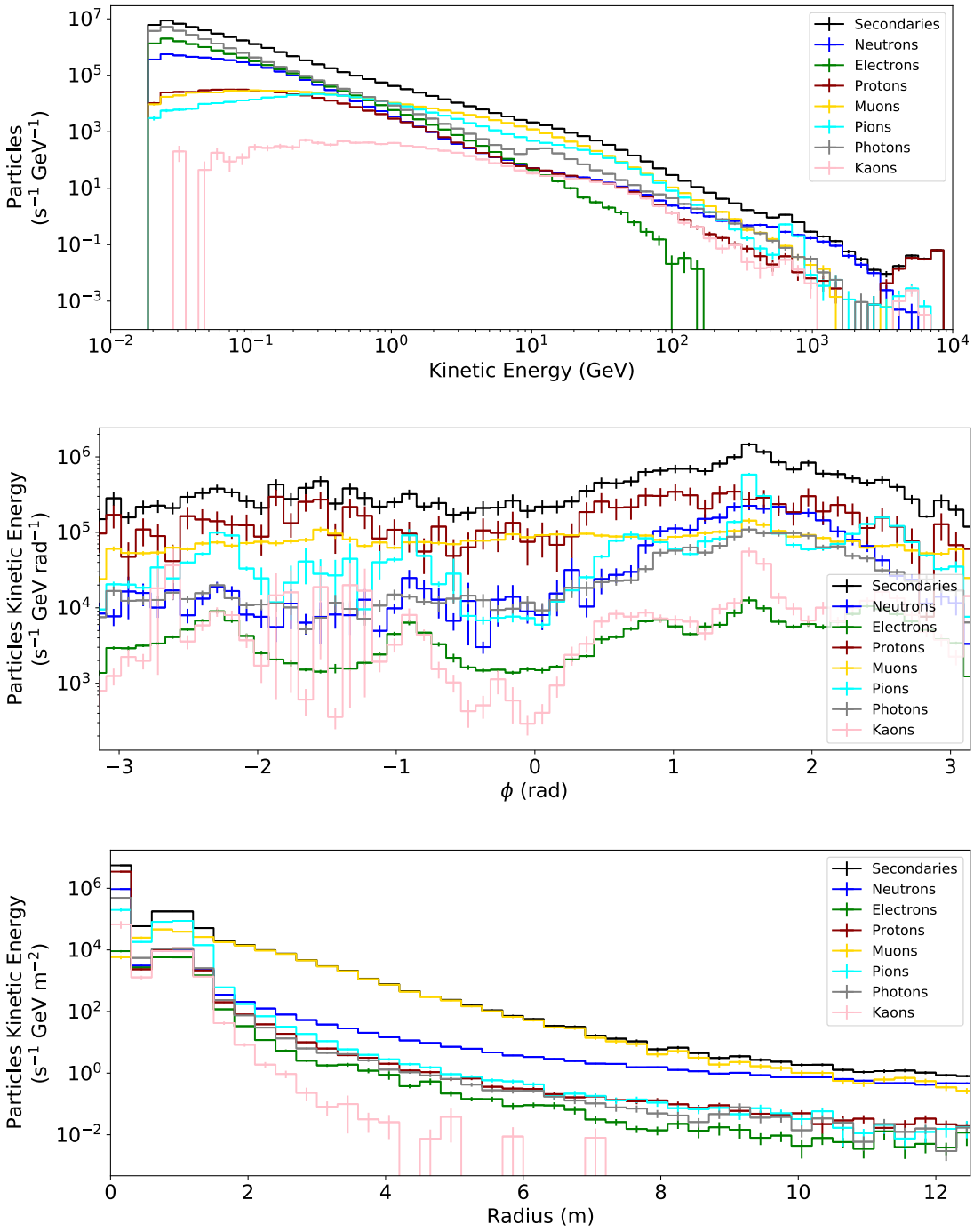

Figure 3.27: Energy (top), and energy-scaled azimuthal spatial (middle) and energy-scaled radial spatial (bottom) distributions for secondary particles at the ATLAS interface plane created from tertiary halo at the HL-LHC with default collision optics v1.5.

The energy and spatial distributions in cylindrical and radial coordinates scaled by the particles' kinetic energy of secondaries created by tertiary halo hits collected at the ATLAS IFP are shown in Figure 3.27. The number of secondaries decreases with

increasing kinetic energy. The integral of the secondary distribution evaluates the total rate of background radiation from the tertiary beam halo at the interface plane to be $\sim 500\,\text{kHz}$. The azimuthal spatial distributions show peaks at $\phi = +\pi/2$ with an overall higher energy contribution in the positive ϕ. Most secondaries are located inside and near the beam pipe and decrease in number for higher radius (reduced by tunnel wall shielding). For larger radii ($\text{R} > 1\,\text{m}$), the most significant contribution comes from muons. This is because muons can pass through more material than other particles before interacting.

The effects of beam halo were also studied for different optics, mainly for changes in β^*, as this parameter changes during the beam preparation for collisions, and slight β^* variations occur as a means of luminosity levelling. The point of origin of secondary particles and muons scaled by their kinetic energy at the interface plane is shown in Fig. 3.28 for $\beta^* = 15$, 20 and 100 cm. The highest contribution for all particles comes from directly hitting the TCTs at $-220\,\text{m}$ and $-140\,\text{m}$ and immediately in front of the interface plane. For muons, high energy contribution also comes from secondary hits on the aperture or particle decay. In both cases, the optics with $\beta^* = 15\,\text{cm}$ produces more background radiation than higher β^* settings.

The azimuthal spatial distributions scaled by energy for all secondary particles and muons comparing $\beta^* = 15$, 20 and 100 cm at the interface plane are shown in Fig. 3.29. All scenarios peak at the positive $\phi = \pi/2$ angle, and most of the background radiation is created from $\beta^* = 15\,\text{cm}$ and decreases for increasing β^*. For muons, the distributions for all β^* values have peaks at $\phi = \pm\pi/2$ and decrease with increasing β^* value.

In conclusion, tertiary beam halo produces background at the ATLAS interface plane up to $\sim 500\,\text{kHz}$. The background radiation level increases with decreasing β^* and most of the background radiation is pointed towards $\phi = \pm\pi/2$, which corresponds to the positive x-plane.

3.4.2 HL-LHC IP 1 beam 2 results

Beam halo losses are expected to differ for the two beams at IP 1 due to the distance between the primary and the tertiary collimators and the position of the tertiary collimators as a function of beam size. The differences for the $\beta^* = 15\,\text{cm}$ optics for beams 1 and 2 are presented here. The results use the long beam cleaning lifetime of 100 hours.

The position of the creation vertex of secondary particles scaled by the kinetic energy they produce at the interface plane is shown in Fig. 3.30. The highest contribution for

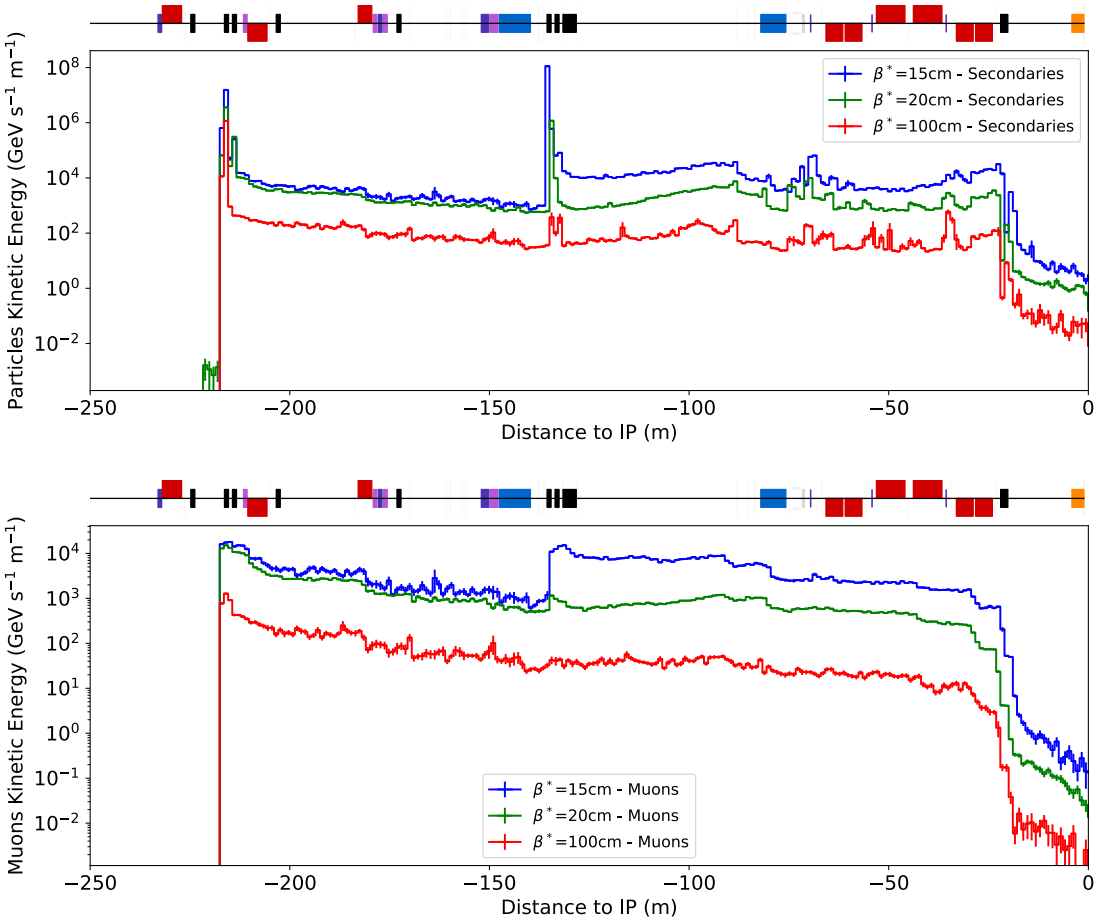

Figure 3.28: Origin of all secondary particles (top) and muons (bottom) reaching the interface plane from beam halo background origin for HL-LHC v1.5 optics for $\beta^* = 15$, 20 and 100 cm.

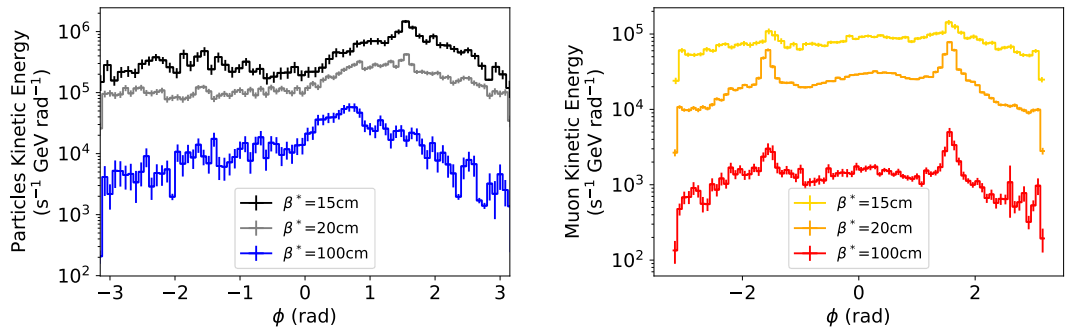

Figure 3.29: Azimuthal spatial distribution scaled by kinetic energy for all secondary particles and muons at the interface plane for HL-LHC v1.5 optics with $\beta^* = 15$, 20 and 100 cm.

all particles comes from primaries hitting the TCTs at −220 m and −140 m. Beam 2 distribution shows more particles created elsewhere than beam 1 by at least an order of magnitude.

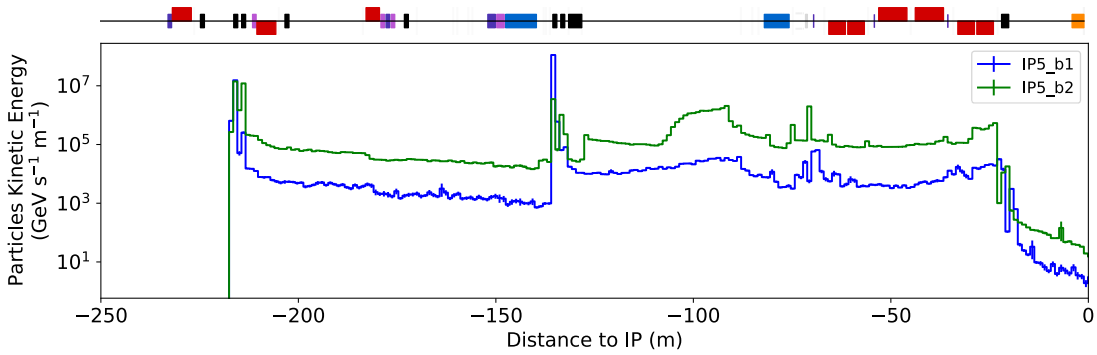

Figure 3.30: Longitudinal position of the creation vertex of secondary particles scaled by their kinetic energy reaching the interface plane from beam halo origin from beams 1 and 2 for HL-LHC v1.5 optics for $\beta^* = 15$ cm.

The azimuthal distributions scaled by the particles' kinetic energy for secondary particles and muons at the interface plane are shown in Fig. 3.31. The distribution of muons has peaks at $\phi = \pm\pi/2$ where at $\phi = \pi/2$ the peak mainly consists of μ^- and at $\phi = -\pi/2$ it is made of μ^+. The positive ϕ orientation displays more background charged particles for both figures. Neutral particles such as photons and neutrons contribute more to negative azimuthal angles.

In conclusion, the tertiary halo from beam 2 produces higher levels of background than beam 1 (~ 9 MHz vs ~ 0.5 MHz). The background radiation has similar distribution and originates from the same locations.

3.4.3 HE-LHC IP 1 results

This study presents the effects of using different dog-leg offsets on the beam losses and, in particular, the behaviour of neutral secondaries using the BDSIM accelerator simulation package. The results are examined at the end of IR 7 and at the position of the ATLAS interface plane.

All energy losses from primary halo around the beamline are shown in Fig. 3.32 and a zoomed-in review of IR 7 losses is in Fig. 3.33. At the location of the primary collimators, more energy loss is seen in IR 7. The total energy loss in the IR 7 section (900 m length) is integrated and summarized in Table 3.5. A dog-leg with no offset produces the least losses

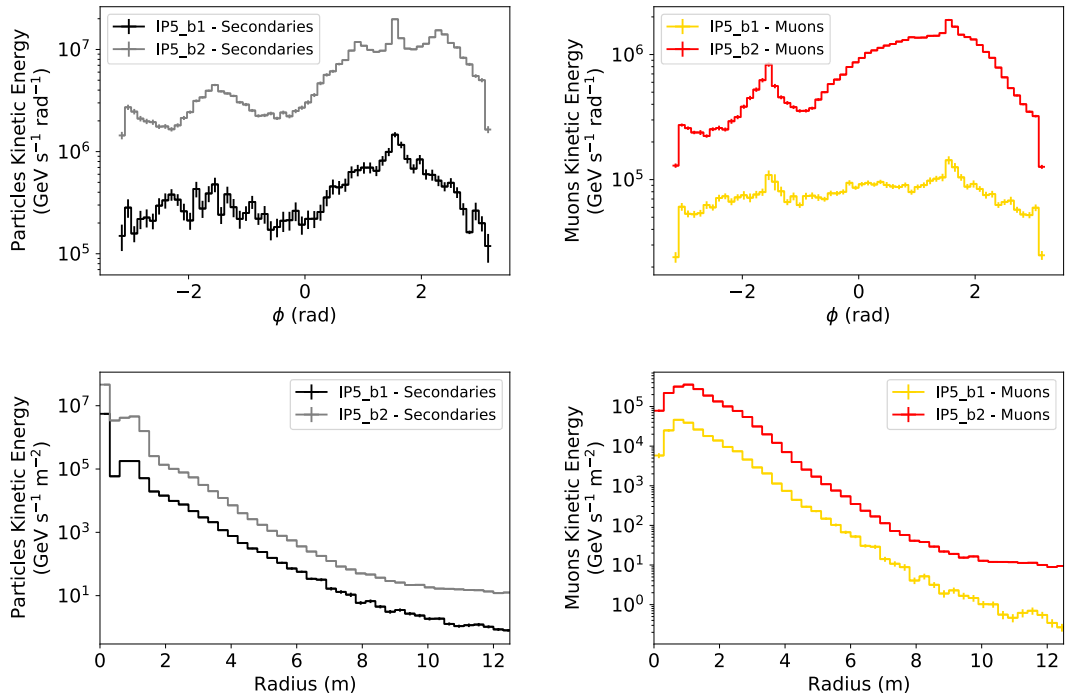

Figure 3.31: Azimuthal (top) and radial (bottom) distributions for secondary particles (left) and muons (right) at the interface plane for beams 1 and 2 of the HL-LHC v1.5 optics with $\beta^* = 15\,\text{cm}$.

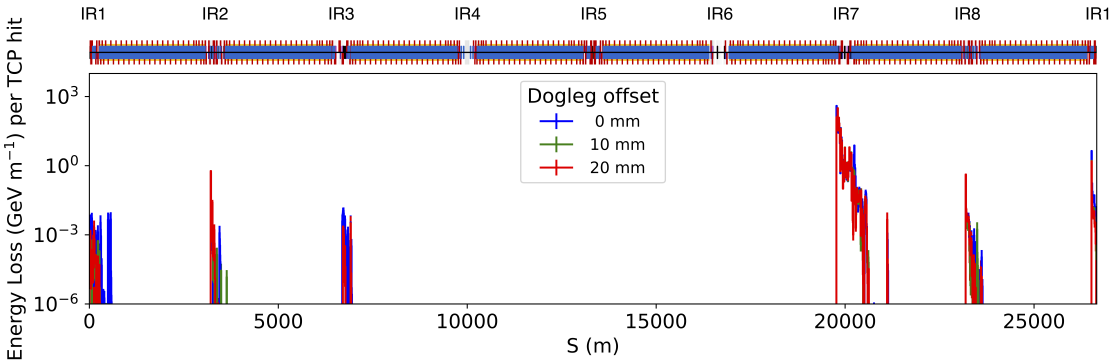

Figure 3.32: Beam halo losses on collimators around the HE-LHC beamline for different dog-leg offsets. Highest losses are in the betatron cleaning area IR 7. IR 5 does not have any collimators in this optics version and therefore does not show any losses.

in this region, while a dog-leg with offsets of 10 mm and 20 mm produce an equal energy loss.

The losses in IP 1 due to particles scattered at the tertiary collimator are shown in Figure 3.34. A 0 mm dog-leg offset results in the highest background level at IP 1.

The integrated energy loss in the IR 1 section (between 26250 and 26650 m) is pre-

Table 3.5: Energy loss in IR 7 of the HE-LHC for different dog-leg offsets.

Dog-leg offset	E_{loss} (GeV / TCP hit)
0 mm	6850 ± 36
10 mm	9524 ± 36
20 mm	9351 ± 35

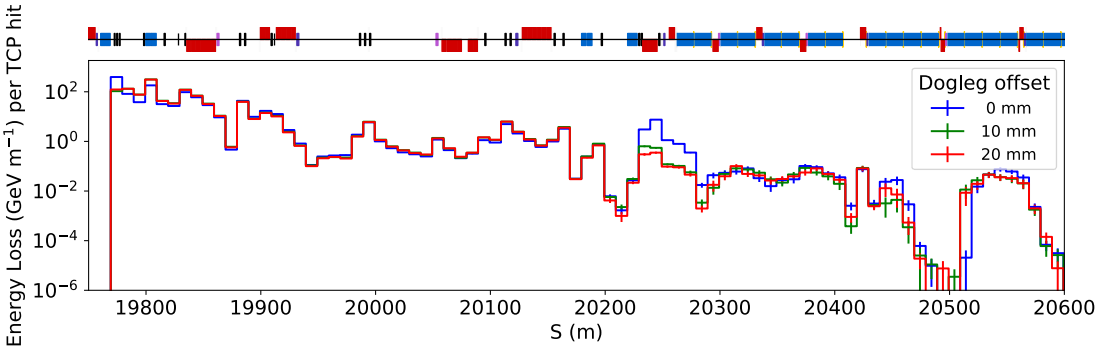

Figure 3.33: Beam halo energy losses in IR 7 of the HE-LHC for different dog-leg offsets.

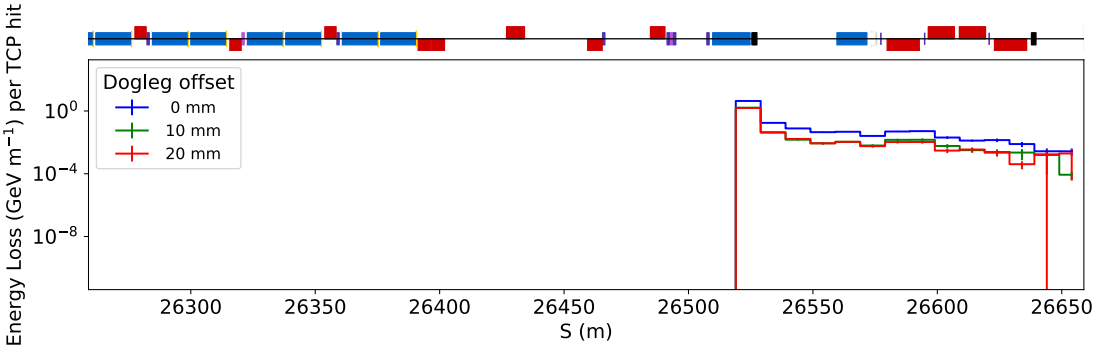

Figure 3.34: Beam halo energy losses in IR 1 of the HE-LHC for different dog-leg offsets.

sented in Table 3.6. A dog-leg with no offset produces the most energy loss in this region, while a dog-legs with offsets of 10 mm and 20 mm result in comparable levels of energy loss. The opposite occurs in IR 7, which could be explained by the more extensive halo particle deposition in IR 7 and the significant attenuation in the material between IR 7 and IR 1 which reduces the number of particles reaching IR 1.

Energy spectra of secondary particles at the interface plane (Fig. 3.35) also show the same distribution for all dog-leg offsets with a higher number of secondaries for the 0 mm offset. The background particles scored at the interface plane have kinetic energies mainly between 1 GeV and 100 GeV with a long tail up to the beam energy.

Table 3.6: Energy loss in IR 1 of the HE-LHC for different dog-leg offsets.

Dog-leg offset	E_{loss} (GeV / TCP hit)
0 mm	49 ± 2
10 mm	18 ± 1
20 mm	17 ± 1

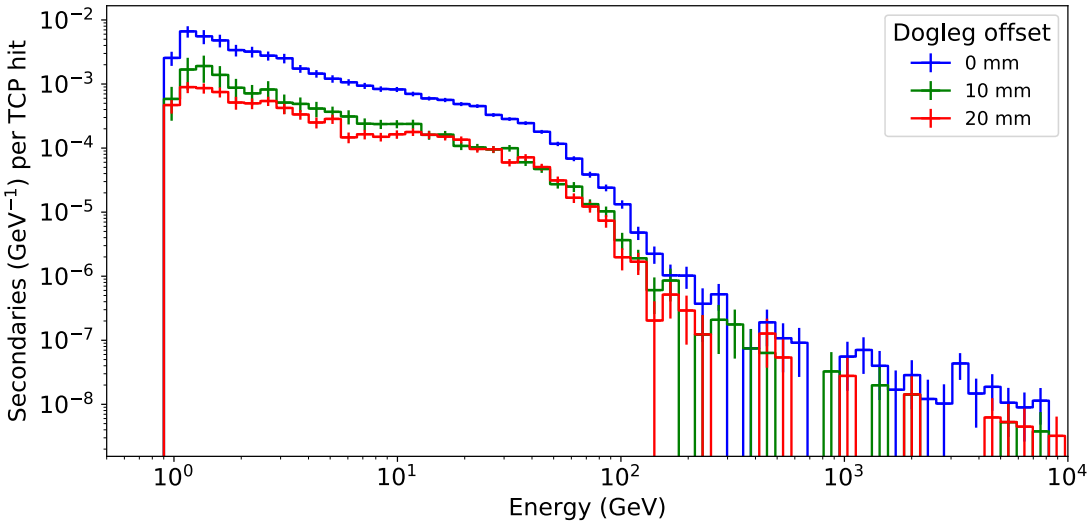

Figure 3.35: All secondary particles kinetic energy spectrum at IP 1 scaled per single primary collimator hit.

To conclude, beam halo induced background reaching the ATLAS detector for the HE-LHC collision energy settings decreases with the dog-leg offset. For all particle types, the spatial distribution stays the same but the number of particles at the interface plane decreases. Since the accelerator settings are not yet decided, the estimated values of energy loss in IR 7 and IR 1 are subject to change depending on the exact parameters being used.

Similar simulations presented in [66] performed in FLUKA show that the scenarios without dog-leg magnets would deliver a dangerously high power load to the superconducting magnets after IR 7 caused by energetic neutral particles. The main input parameters of both simulations (beam parameters, collimator settings) are the same. The difference in results can be attributed to the different level of detail in the geometry between BDSIM and FLUKA simulations, but the input parameters such as the impact parameter, halo distribution and optics settings should also be reviewed between the two simulations. The primary goal of FLUKA study was to determine the power load increase to the cold section magnets. Their findings show a dramatic increase in power load due to energetic neutral

particles which would be prevented with the use of the dog-leg. The goal of BDSIM studies was used to check the beam background radiation differences in IR 1, which is lowest with higher dog-leg offset, but the results in IR 7 disagree with FLUKAs. Nonetheless, the dog-leg importance should be reviewed if the HE-LHC project is approved and the operation parameters are determined.

3.5 Summary

This chapter studied the non-collision background impacting the ATLAS detector. Results were presented using the ATLAS interface plane as a region of interest for simulation scoring for the different optics and foreseen parameters of the HL-LHC and HE-LHC.

The studies with most importance to the HL-LHC design and operation are beam-background radiation level results using the up-to-date default parameters (v1.5) and their comparison to the current LHC levels. The upgrades of the accelerator have effects on background levels and needs to be quantified. Other operational parameters (β^* and collimator settings) will be used not as often and not for main physics studies of the large particle experiments. The studies of the levels of NCB due to these parameter changes are not as significant as the principal settings since their contribution will be much smaller. The studies of geometry changes are only used in decision making in choosing the best geometry for its primary use as well as minimizing background levels to the detectors. After the geometry is selected, the other options will no longer be relevant and the preferred option will be part of the default settings.

The comparison between BDSIM vs FLUKA of HL-LHC v1.0 results reveals that BDSIM produces comparable background levels at the ATLAS interface plane assuming the same accelerator configuration. The evolution of optics from v1.0 to v1.5 shows a decrease in the beam-gas background thanks to more shielding, collimators and other changes in element location. Beam-gas induced background was found to have a negligible dependence on the β^* optics. Beam halo background is inversely proportional to β^*.

The comparison of background effects at the interface plane of ATLAS from beam-gas and beam halo interactions are displayed in Fig. 3.36. Beam halo contributions are shown for the long beam lifetime of 100 h scenario. For particle rate at the interface plane, beam halo contribution (1×10^7 Hz) is higher than the background from beam-gas interactions (3×10^6 Hz) by one order of magnitude. However, for energy scaled particle

rate the beam-gas background (5×10^8 GeV Hz) is higher by one order of magnitude than beam halo induced background (5×10^7 GeV Hz). This result is comparable within one order of magnitude to previous HL-LHC studies published in [3].

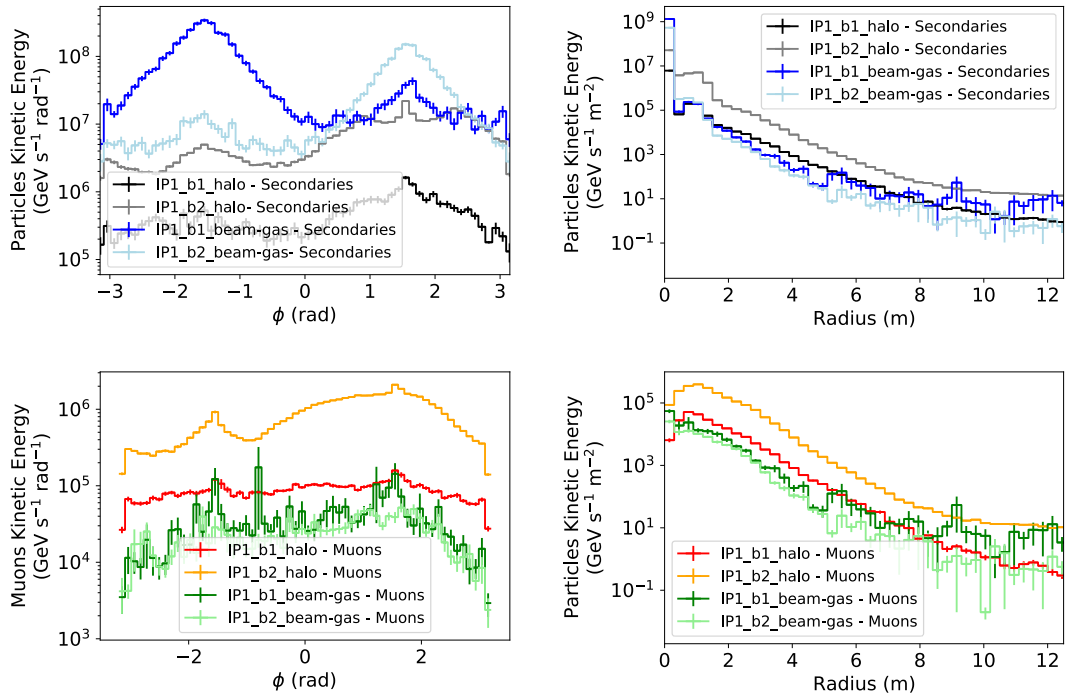

Figure 3.36: Azimuthal (left) and radial (right) spatial distributions scaled by kinetic energy for all secondaries (top) and muons only (bottom) for different background process and beam origin.

The propagation of beam halo background radiation was also investigated for the possible HE-LHC accelerator. The dog-leg offset in IR 7 is introduced in LHC to widen the intra-beam distance to accommodate larger elements. This is not necessary in HE-LHC since the intra-beam distance is larger and therefore the use of the dog-leg is reviewed. The results show that the beam offset due to the dog-leg decreases the level of tertiary halo background at the detector interface plane in IR 1 for all particle types and is therefore beneficial.

The background propagation between the ATLAS interface plane, and the detector, as well as the detector response, are presented in Chapter 5. Chapter 4 investigates the BIB in second high luminosity interaction region of the HL-LHC, at the CMS detector and compares the background radiation rates between CMS and ATLAS.

4 Accelerator background reaching the CMS detector

Beam background is present in the ATLAS experiment as well as in other experiments of the Large Hadron Collider (LHC) such as the CMS. It can similarly negatively affect detector operation and physics analyses. The CMS detector is located at IP 5 of the LHC. The high luminosity regions (IR 1 and IR 5), which generate small beam sizes at the interaction point, are almost identical in terms of hardware and optics. The most significant difference between the IPs is the orientation of the crossing angle plane. For HL-LHC, the crossing plane is in the horizontal plane at IP 1 and in the vertical plane at IP 5.

This chapter presents the beam-induced background studies reaching the CMS interface plane and compares the results to that of the similar studies for ATLAS presented in Chapter 3. The results are shown for the HL-LHC optics v1.5 and the corresponding geometry setup.

4.1 Model and simulation setup

The geometry model used for IR 1 studies is also used for simulations of beam-induced background in IR 5. This is possible because the tunnel shape is the same, with small exceptions that are neglected, such as the difference in the number and location of service rooms inside the tunnel. The top view of the tunnels for beam 1 approaching IP 1 and IP 5 is shown in Fig. 4.1. The tunnel structure is only different in the last $\sim 100\,\mathrm{m}$ before the collision point. This difference could affect the distribution of background radiation in the surrounding areas of the detector hall but is unlikely to change background distribution inside the detector itself because of the structure's location far from the collision point and the direction away from the beamline.

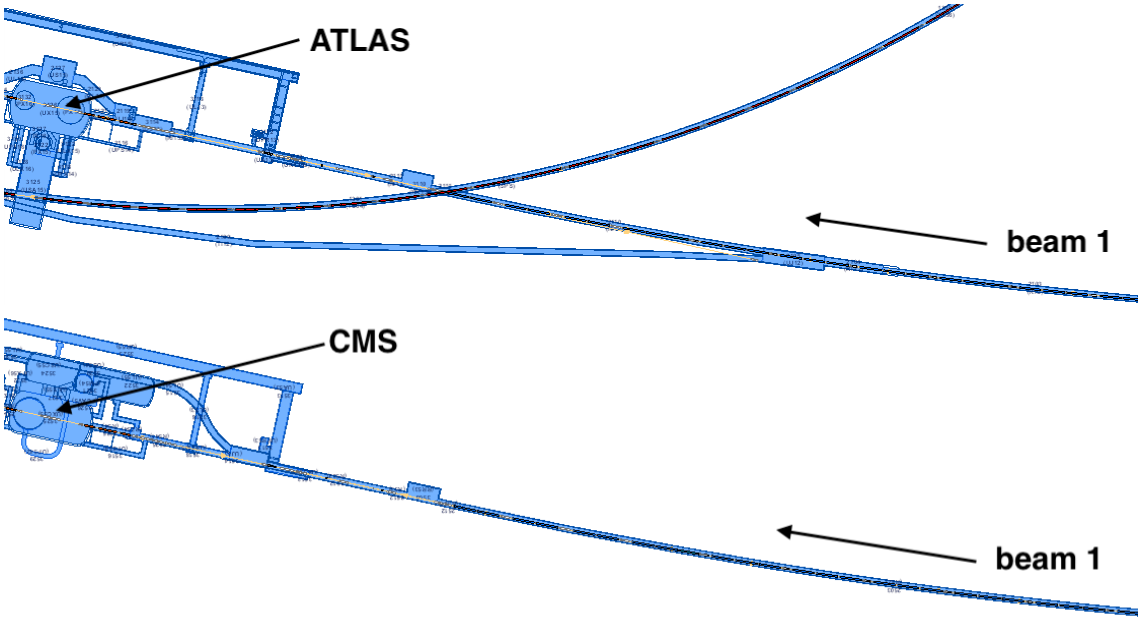

Figure 4.1: Aerial view of the accelerator tunnel complex leading to the ATLAS (top) and CMS (bottom) experimental halls.

The accelerator lattice elements in the last 540 m in front of IP 1 and IP 5, shown in Fig. 4.2, are also very similar. Significant differences include the position of the kickers and the location of a few elements, such as collimators, with respect to the collision point.

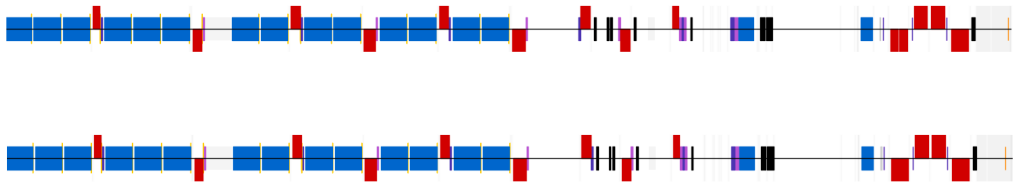

Figure 4.2: The accelerator lattice elements in the last 540 m in front of IP 1 (top) and IP 5 (bottom). The collision points are on the right.

Since the lattice elements are very similar, we expect the beam parameters to match. The main optics parameters for IP 1 and IP 5 are compared in Figure 4.3 for both before and after the collision point. The beam size reaches up to 2.4 mm in the final focusing quadrupoles with a maximum beam offset of 10 mm from the beam ideal orbit for colliding beams. The beam centroid is offset in opposite planes (horizontal in IP 1 and vertical in IP 5). Dispersion is 0 m at the intersection point, which ensures the smallest possible emittance.

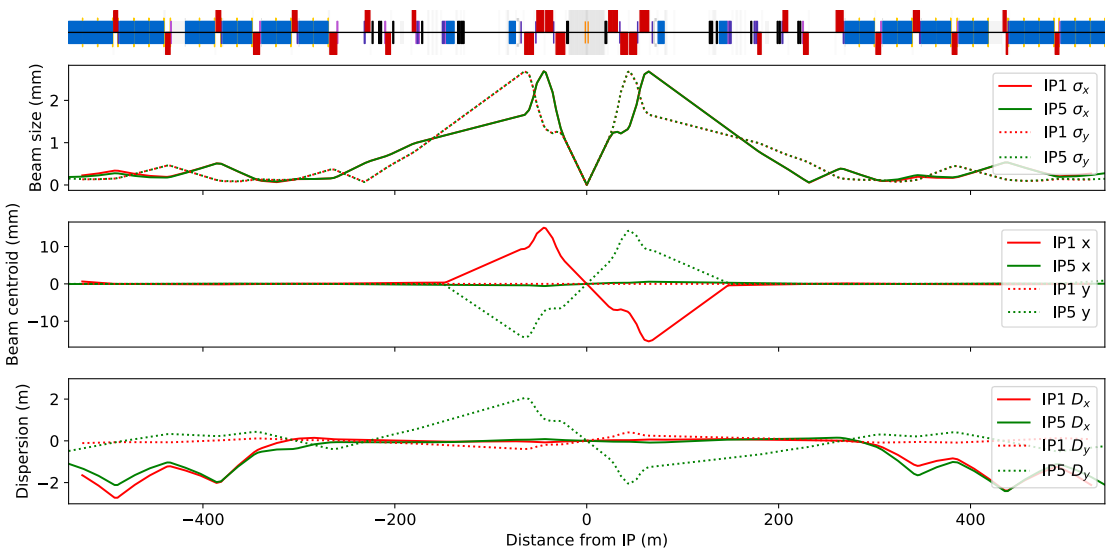

Figure 4.3: Beam size (top), beam centroid position (middle) and dispersion (bottom) in IP 1 and IP 5 for HL-LHC optics with $\beta^* = 15\,\text{cm}$.

4.2 CMS beam-gas studies

To quantify the levels of beam-gas background radiation on the CMS detector, local beam-gas interactions were simulated inside the beam pipe in the IR 5 straight section. Secondary particles generated from the interactions were propagated to the detector interface plane at 22.5 m from the collision point, as was the case in ATLAS simulations, where particles type and kinematic properties are recorded. As the background originates from inside the beam pipe but can propagate up to metres away in the transverse direction, a simulation of both accelerator and its surrounding geometry is necessary. The simulation model was developed using BDSIM. This model accounts for accelerator elements with magnetic fields, aperture size and material, and the tunnel, caverns and other shielding elements. A beam distribution with HL-LHC parameters is generated and propagated through IR 5. The beam pipe vacuum pressure is assumed to be uniform everywhere in IR 5. The cross-section of the interactions between the primary protons and the gas is biased to achieve high statistics and a flat primary hit distribution. The bias is re-weighted in the analysis.

Beam-gas simulation results use a kinetic energy (KE) cut of 20 MeV, which is the minimum energy for particles detected by the vertex detector. All secondary particles are scored at a virtual sampler plane with a diameter of 25 m, large enough to detect all particles heading for CMS (which has a diameter of 15 m). Simulations are scaled per single beam-gas interaction with additional scaling using the beam-gas interaction rate. The

results are then rescaled per second of nominal HL-LHC operation using 2.2×10^{11} protons per bunch with 2808 filled bunches. The HL-LHC optics v1.5 with $\beta^* = 15\,\text{cm}$ was used to create results with 2.5×10^6 beam-gas interactions per simulation.

4.2.1 Beam 1

This section presents the simulated results of beam-gas interactions in the IR 5 from beam 1 origin for the HL-LHC optics v1.5 with $\beta^* = 15\,\text{cm}$.

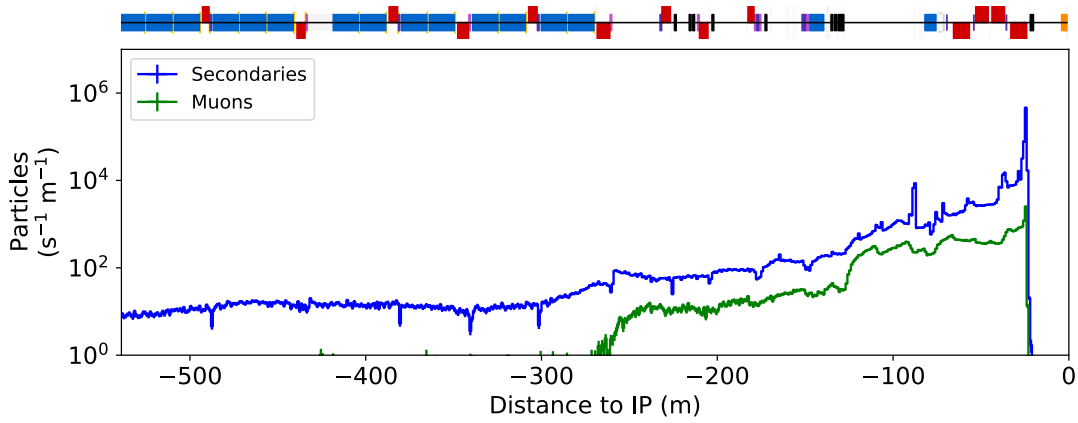

Figure 4.4: Origin of all secondary particles and muons due to beam-gas background scaled by their kinetic energy reaching the IP 5 interface plane from beam halo origin in beam 1 for HL-LHC v1.5 optics with $\beta^* = 15\,\text{cm}$ with kinetic energy cut of 20 MeV and flat hydrogen gas pressure profile.

The location of origin of all secondary particles and muons reaching the interface plane for beam 1 is shown in Fig. 4.4 for $\beta^* = 15\,\text{cm}$. The background rate increases with decreasing distance to the IP. Muons follow the same origin distribution with fewer muons produced per unit of time and length. All secondary particles show many jumps throughout the region due to the radiation being absorbed by the material of the accelerator components. Long drifts provoke an increase in background radiation.

The energy, azimuthal and radial spatial distributions for different secondary particles at the interface plane of IP 5 for beam 1 are shown in Fig. 4.5. Energy scaled distributions measure how much kinetic energy is present at each spatial location in different coordinates. The energy spectra show a decrease in particles with energy. The integral of the rate distribution for secondaries is 8.5×10^5 Hz. Low energy (20 MeV<KE< 1 GeV) background radiation is mainly composed of photons, electrons and neutrons. For higher energies (20 MeV<KE< 1 TeV), the most common particles are pions and photons. For

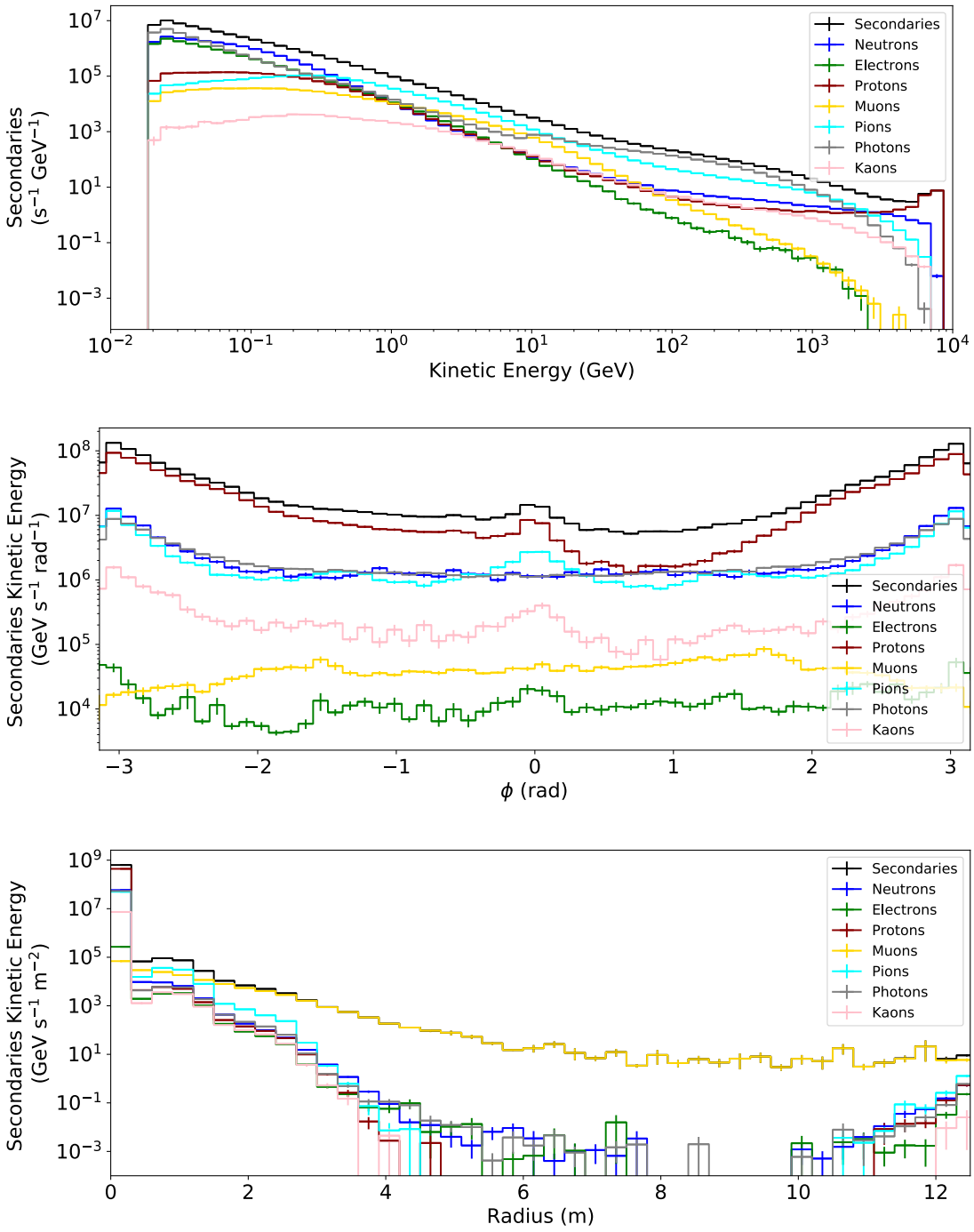

Figure 4.5: Energy (top), azimuthal (middle) and radial (bottom) distributions of beam-gas background from beam 1 at the CMS interface plane with HL-LHC v1.5 optics for selected secondaries.

energies close to 7 TeV, protons from small angle beam-gas scattering dominate. The azimuthal spatial distributions scaled by the kinetic energy of the selected secondary particles show peaks at $\phi = 0$ and $\pm\pi$ rad, which indicates that the background radiation is mainly

directed towards the horizontal plane. The muon distribution is concentrated in the vertical plane; it is not affected by the bending field of the dipoles. The spatial distribution decreases as a function of radius for all particles with a significant dip at (R$\sim$ 0.5 m), where most material is concentrated and provides a shield.

In conclusion, beam-gas interactions in beam 1 produce background radiation at the CMS interface plane up to a level of $\sim$ 1 MHz. The background level decreases with the kinetic energy, and is concentrated in the horizontal plane, mostly inside and close to the beam pipe.

4.2.2 Beam 2

This section presents the simulation results of beam-gas interactions in the IR 5 from beam 2 origin and a comparison with the beam 1 results. The beam-gas background is expected to have the same magnitude and distribution for both beams as the optics and geometry are analogous. The differences in results will come from the shorter tunnel geometry file used for beam 2 (only the straight section uses tunnel geometry) and minor differences in the positions of accelerator elements.

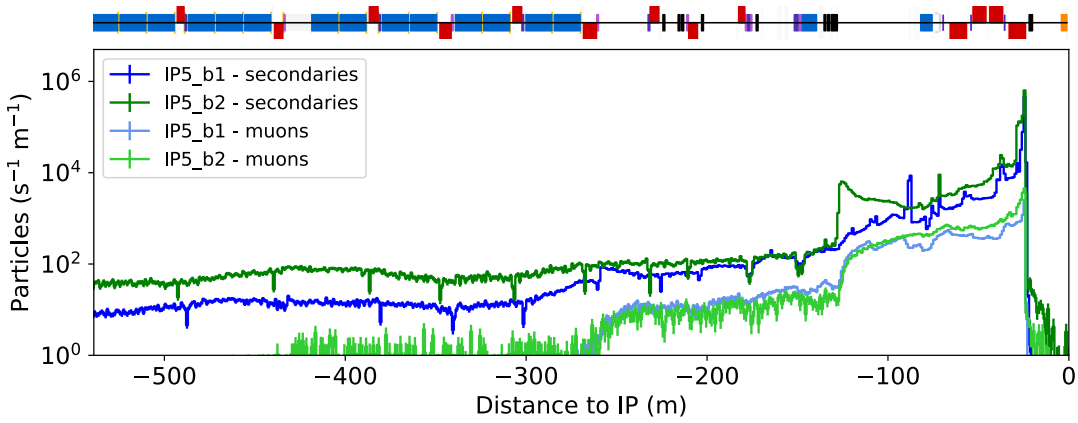

Figure 4.6: Origin of secondary particles and muons due to beam-gas interactions reaching the IP 5 interface plane from beam-gas for beam 1 and beam 2 for HL-LHC v1.5 optics with $\beta^* = 15$ cm.

The origin of secondary particles and muons at the interface plane for both beams is shown in Fig. 4.6 for $\beta^* = 15$ cm. The number of background particles increases throughout the section, with a higher increase after the dispersion suppression section (~ -250 m) and after the TAN (~ -130 m). The distributions for both beams are similar. More particles are generated further out for beam 2, which is caused by shorter shielding present in

beam 2. The beam 2 tunnel geometry only extends up to the end of the straight section ($\sim -250\,\mathrm{m}$). The peak at $\sim -130\,\mathrm{m}$ from the IP for beam 2 is caused by interactions with the tertiary collimators.

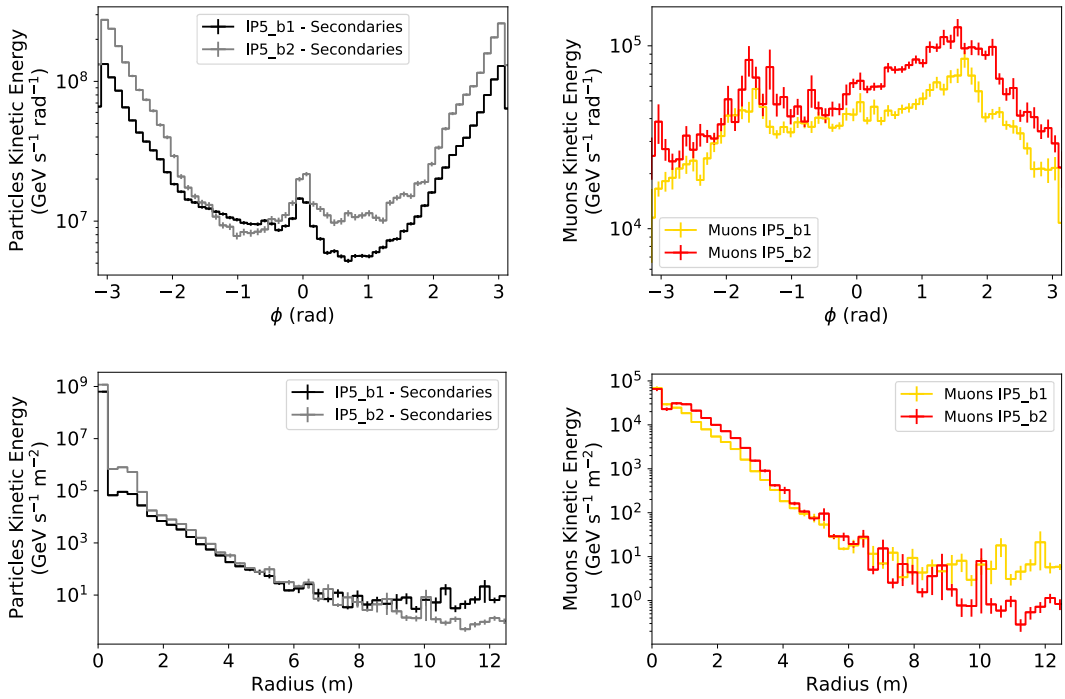

Figure 4.7: Azimuthal (top) and radial (bottom) spatial distributions from beam-gas induced background scaled by their kinetic energy for all secondary particles (left) and muons only (right) at the interface plane of CMS for beam 1 and beam 2 of the HL-LHC v1.5 optics with $\beta^* = 15\,\mathrm{cm}$.

The azimuthal and radial distributions scaled by energy for secondary particles and muons for both beams at the interface plane of CMS are shown in Fig. 4.7. All distributions are similar. The azimuthal distribution for secondaries shows peaks at $\phi = 0$ and $\pi\,\mathrm{rad}$, in the horizontal plane. Muon distribution peaks at $\phi = \pm\pi/2$ in the vertical plane. The difference between the distributions can be attributed to the fact that muons propagate outside the magnet volume more easily than other particles and are less deflected by the dipole magnetic fields. The kinetic energy of background particles decreases with the radius for all particle types, but most energy is concentrated inside the beampipe. Calculating the total secondary rate distribution integral, the background radiation frequency is $1.7 \times 10^6\,\mathrm{Hz}$.

In conclusion, beam-gas background from beam 2 produces background radiation at the CMS interface plane up to a level of $\sim 2\,\mathrm{MHz}$. The rate of background radiation

decreases with kinetic energy and is concentrated in the horizontal plane, mostly inside and close to the beam pipe. The background radiation rates from beams 1 and 2 have similar spatial distributions. The total rate of beam-gas induced background from beam 2 is about twice as high, which can be attributed to the difference in the geometry model, but the overall difference is minor.

4.3 CMS beam halo studies

A Sixtrack simulation was used to create impacts on TCTs in the IR 5 originating from primary impacts on TCPs in the IR 7. The Sixtrack simulation results were provided by Bjorn Lindstrom from the HL-LHC collimation team [38]. The optics scenario with $\beta^* = 15\,\text{cm}$ was simulated since it is the optics with the smallest β^* considered for HL-LHC nominal operation. $\beta^* = 15\,\text{cm}$ is treated as the worst-case scenario since background levels decrease with increasing β value.

The primary halo simulated in the Sixtrack model impacts on the aperture of the tertiary collimators. The ratios of tertiary impacts per primary collimator hit for the simulation cases are summarized in Table 4.1. The simulations of 4×10^7 primary collimator hits (for both beam 1 and beam 2) produced approximately 5×10^3 tertiary collimator hits in each beam.

Table 4.1: Number of simulated primary hits and the ratio of tertiary/primary hits for IP 5.

Beam direction	β^*(cm)	Simulated primary impacts	TCT impacts per TCP hit
IP5 beam 1	15	4×10^7	1.34×10^{-4}
IP5 beam 2	15	4×10^7	1.21×10^{-4}

The simulations are scaled using the tertiary per primary collimator ratio and the beam lifetime using the optimistic value of 100 hours.

4.3.1 Beam 1

This study presents the impact of tertiary halo from beam 1 at the CMS interface plane for optics v1.5. The smallest β^* setting was studied with the optics settings with $\beta^* = 15\,\text{cm}$, for which we expect the highest background rates due to the largest beam size throughout the IR 5.

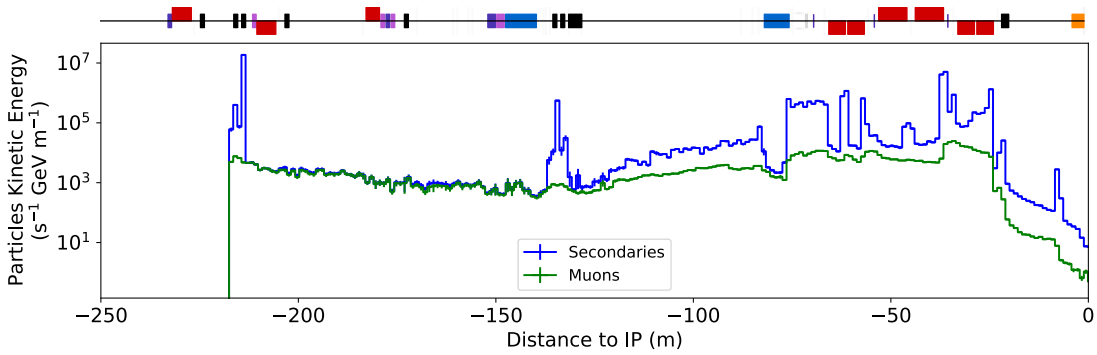

Figure 4.8: Origin of secondary particles (top) and muons (bottom) due to beam halo background scaled by their kinetic energy reaching the IP 5 interface plane from beam halo origin in beam 1 for HL-LHC v1.5 optics with $\beta^* = 15\,\text{cm}$.

The point of origin of all secondary particles and muons scaled by their kinetic energy at the interface plane is shown in Fig. 4.8 for $\beta^* = 15\,\text{cm}$. The highest contribution for all particles comes from primary impacts on the first TCTs at $-220\,\text{m}$. There are additional peaks at the location of the second set of collimators ($-130\,\text{m}$) and throughout the triplet. Muons are not created directly at the collimators but uniformly throughout the section from subsequent decays of secondary particles (e.g. charged pions and kaons).

The energy, azimuthal and radial spatial distributions of secondary particles at the interface plane of IP 5 for beam 1 are shown in Fig. 4.9. Particles of small energy dominate the distribution. For higher energy, the particle rate exponentially decreases. The total integrated beam halo background rate at the interface plane is $3.12 \times 10^6\,\text{Hz}$. The energy-scaled azimuthal distribution shows peaks at $\phi =\sim -3$ and $\pi/2$, caused by the bending field of dipoles. The highest contribution at the peak locations comes from pions. The energy scaled radial distribution shows most particle energy is located inside or near the beam pipe (Radius $< 1\,\text{m}$), with larger radii particle energy at the interface plane decreases. The most significant contribution at a large radius (Radius $> 1\,\text{m}$) comes from muons.

To conclude, the integrated rate of background radiation from tertiary beam halo at the CMS interface plane from beam 1 scaled per unit time of nominal beam operation with a lifetime of 100 h is approximately 3 MHz.

4.3.2 Beam 2

Beam halo losses are expected to differ for the two beams at IP 5 due to the distance between the primary and the tertiary collimators and the position of the tertiary collimators

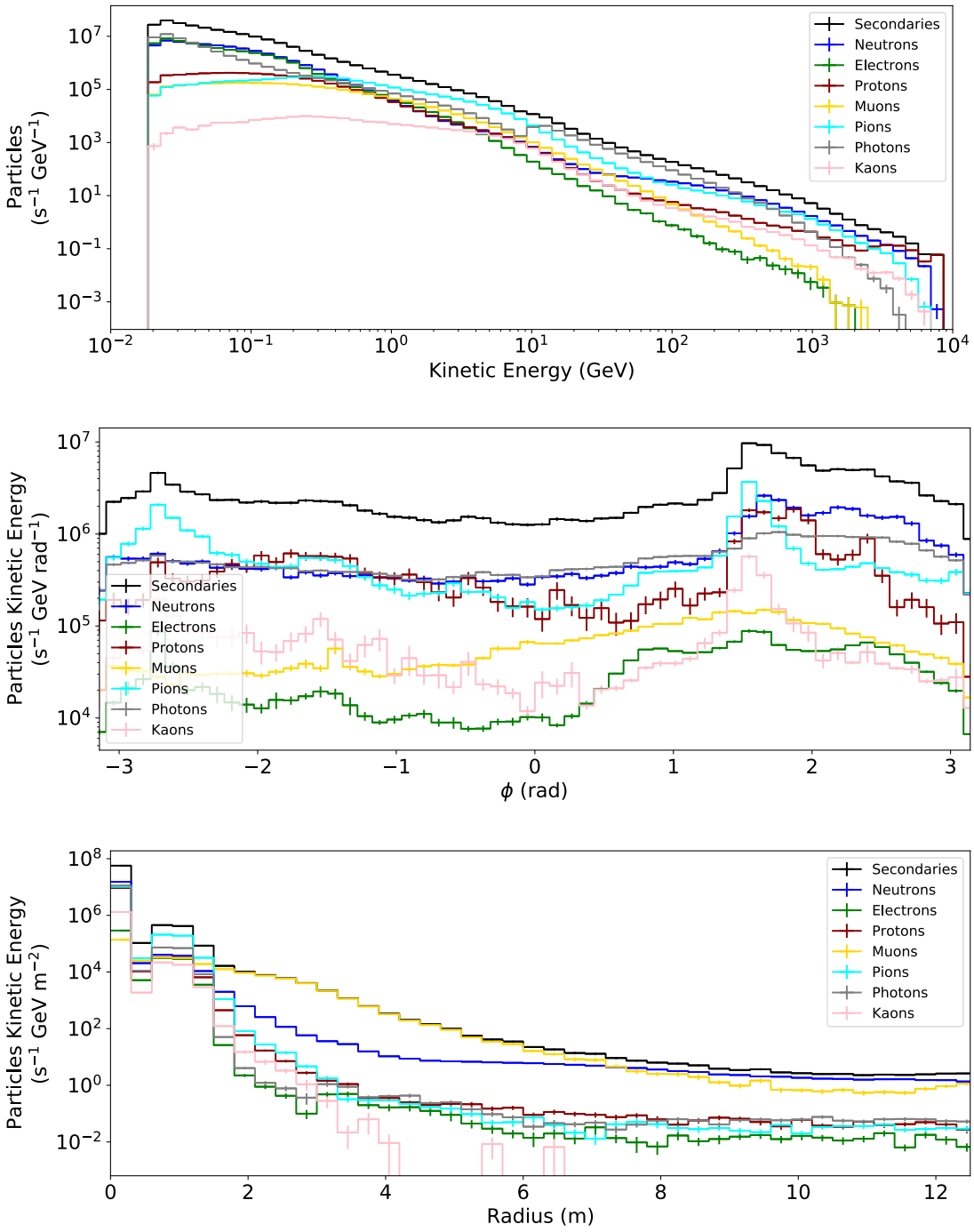

Figure 4.9: Energy (top), azimuthal (middle) and radial (bottom) distributions for secondary particles reaching the IP 5 interface plane from beam halo origin in beam 1 for HL-LHC v1.5 optics with $\beta^* = 15\,\text{cm}$.

in the beamline as a function of beam size. The beam 2 results are compared to the beam 1 beam halo background at the interface plane.

The point of origin of secondary particles and muons scaled by their kinetic energy

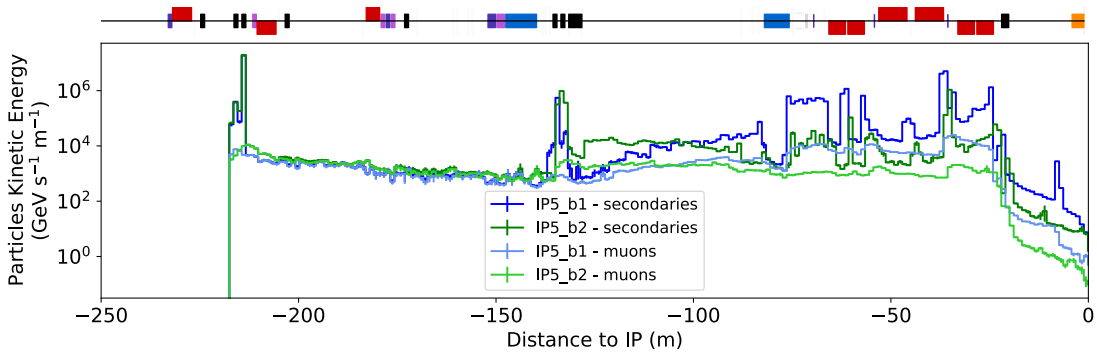

Figure 4.10: Origin of secondary particles and muons scaled by their kinetic energy due to beam halo background reaching the IP 5 interface plane from beam 1 and beam 2 for HL-LHC v1.5 optics with $\beta^* = 15\,\text{cm}$.

at the interface plane is shown in Fig. 4.10 for optics with $\beta^* = 15\,\text{cm}$. The distribution is almost identical to beam 1. The highest contribution for all particles comes from hitting the first TCTs at $-220\,\text{m}$. Additional peaks come from the location of the second set of collimators ($-130\,\text{m}$) and the triplet. Muons are not created directly at the collimators but uniformly through the secondary decay of halo particles.

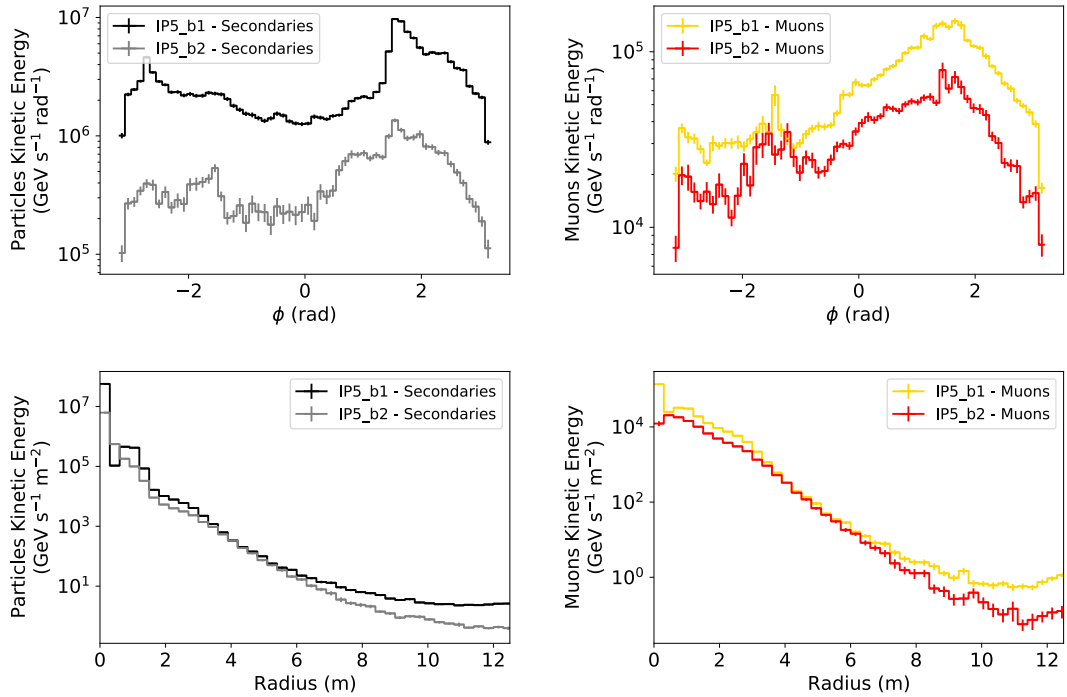

Figure 4.11: Azimuthal (top) and radial (bottom) distributions from beam halo background scaled by their kinetic energy for secondary particles (left) and muons (right) at the interface plane of CMS for beam 1 and beam 2 of the HL-LHC v1.5 optics with $\beta^* = 15\,\text{cm}$.

The azimuthal and radial spatial distributions scaled by energy for secondary particles and muons for both beams at the interface plane of CMS are shown in Fig. 4.11. All distributions have a similar shape. The azimuthal distributions for all secondaries show peaks at $\phi = \pm\pi/2$ in the vertical plane. The vertical plane distribution is caused by kicker magnets for beam positioning for collisions. The contribution from beam 1 is an order of magnitude higher than from beam 2. For muons, it is approximately a factor of 2. The additional energy is distributed mainly inside the beampipe R$<$ 0.5 m and at larger radii, R$>$ 7 m. In general, the kinetic energy of background particles decreases with the radius for all particle types, but most of the energy is concentrated inside the beampipe. Calculating the total secondary rate distribution integral, the background radiation frequency is 4.08×10^5 Hz.

In summary, the total background rate from the tertiary beam halo at the CMS interface plane from beam 2 scaled per unit time of nominal operation assuming a lifetime of 100 h is approximately ~ 0.5 MHz. Compared to beam 1 results in the previous subsection, it is around 1 order of magnitude lower (beam 1 background rate is ~ 3 MHz).

4.4 CMS beam background summary

The summary comparison of background effects at the interface plane of the CMS experiment for beams 1 and 2 from beam-gas and beam halo interactions is shown in Fig. 4.12. Beam halo contributions are offered for a beam lifetime of 100 h, which is the expected default operation estimate. For all secondaries, the energy delivered to the interface plane per second of regular operation for beam-gas interactions is higher by an order of magnitude than for the radiation induced by the beam halo background. The two background radiation sources are comparable in terms of particle fluence at the interface plane. Muons have a higher background level from beam halo origin from beam 1.

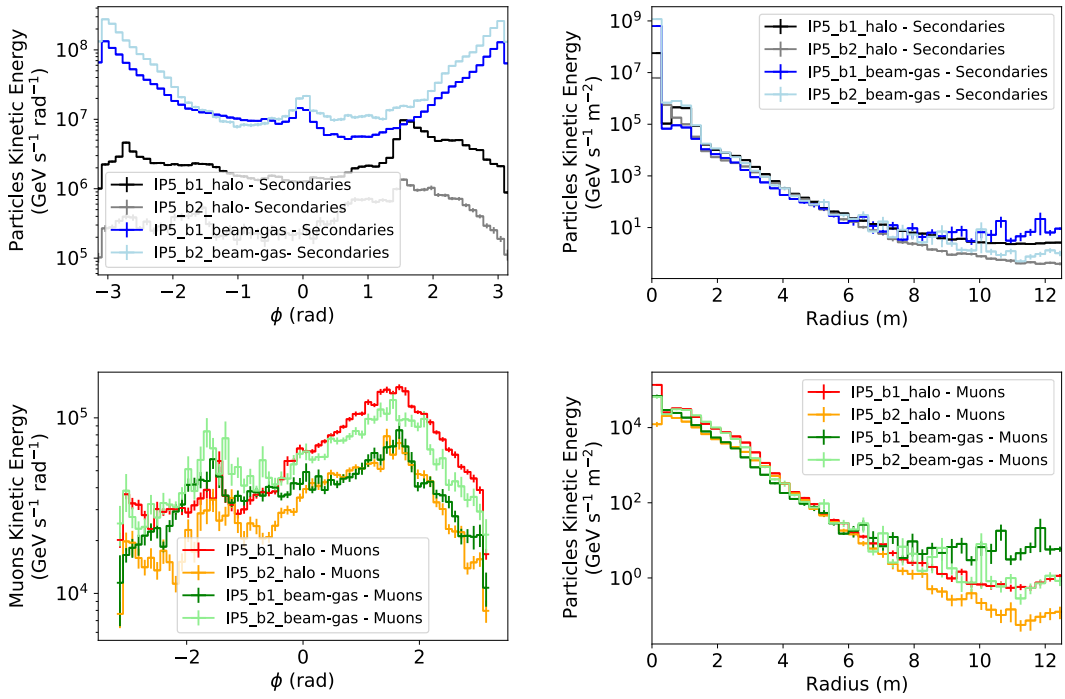

Figure 4.12: Azimuthal (left) and radial (right) spatial distributions for all secondaries (top) and muons (bottom) for different creation processes at the interface planes of CMS at the HL-LHC.

4.5 Comparisons between ATLAS and CMS

ATLAS and CMS are both high luminosity multi-purpose experiments of the HL-LHC. The accelerator sections where they are located have similar geometry and lattice elements. This section compares the radiation levels at the interface planes for both experiments for background from beam halo and beam-gas processes. Beam-gas events are scaled using the hydrogen gas interaction cross-section for the density of 10^{11} molecules / m^3. The beam halo is scaled using the tertiary per primary collimator impact ratio and the long beam lifetime of $\tau = 100\,\text{h}$. All simulations use the nominal HL-LHC parameters from optics v1.5 with $\beta^* = 15\,\text{cm}$.

4.5.1 Beam 1

The comparison of background effects at the interface planes of ATLAS and CMS for beam 1 from beam-gas and beam halo interactions is shown in Fig. 4.13.

The azimuthal spatial distribution of energy scaled secondary particles shows different distributions for beam halo background with peaks at $\phi = \pi/2$ for both interface

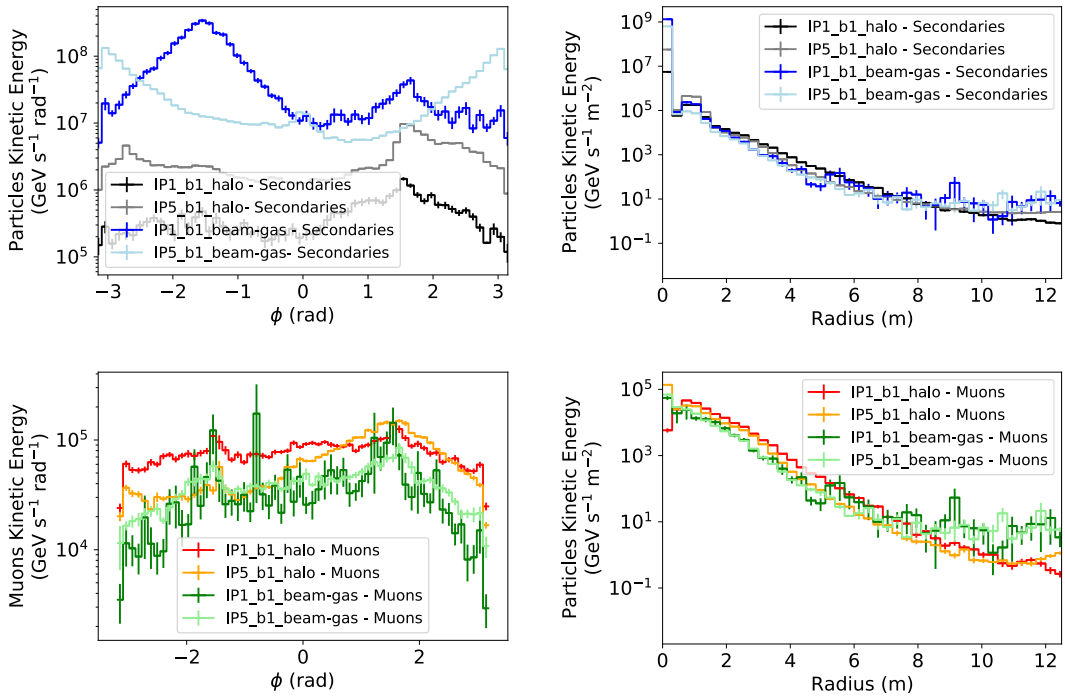

Figure 4.13: Azimuthal (left) and radial (right) spatial distributions for all secondaries (top) and muons (bottom) for different background origin for beam 1 at IP 1 and IP 5 of the HL-LHC.

planes and beam gas distribution with peaks at $\phi = \pm\pi/2$ at IP 1 and peaks at $\phi = \pm\pi$ and $\phi = 0$ at IP 5. The angular difference is due to the opposite orientation of the collision plane. Muon background has extremes in the azimuthal angle at $\phi = \pm\pi/2$ for all scenarios. Radial spatial distribution for all secondaries is similar for both IPs, with a maximum near the beam pipe and a sharp decrease in the background for a larger radii. The background radiation hit rate from beam-gas interactions and beam halo process are generally similar. The total energy these particles deliver is higher for beam-gas contribution by one order of magnitude. The summary of all the integrated rates from the different sources of background radiation is shown in Table 4.2.

4.5.2 Beam 2

The comparison of background effects at the interface planes of ATLAS and CMS for beam 2 from beam-gas and beam halo interactions is shown in Fig. 4.14.

The azimuthal spatial distributions show peaks at $\phi = \pm\pi/2$: muons in all scenarios, beam-gas at IP 1 and beam halo at IP 1 and IP 5. The beam-gas contribution at IP 5 has

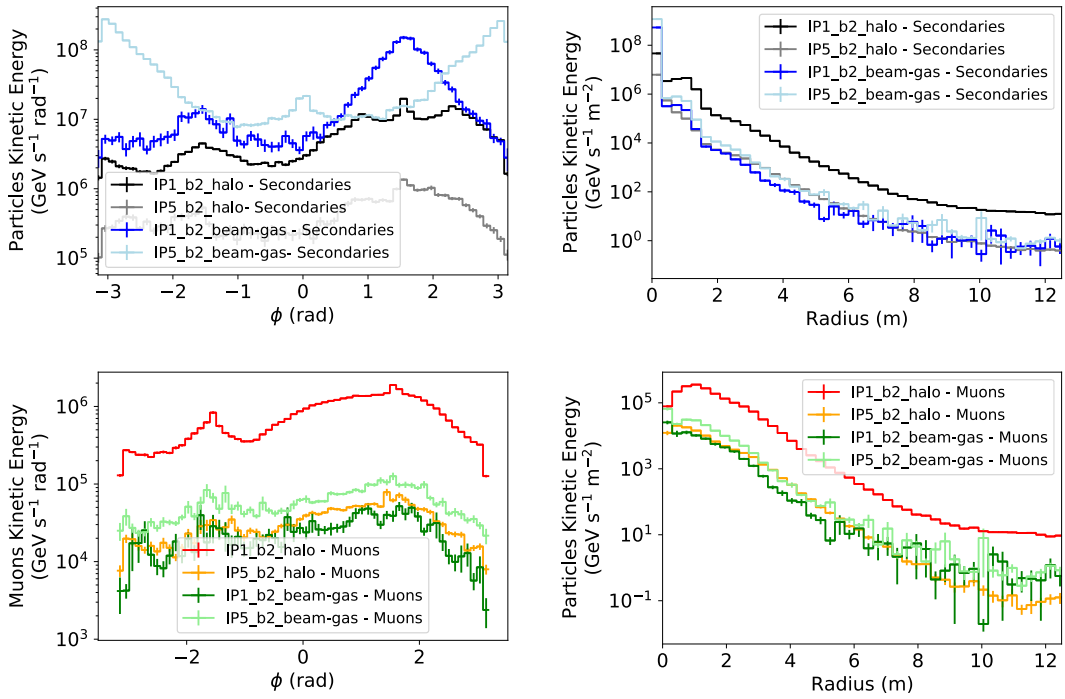

Figure 4.14: Azimuthal (left) and radial (right) spatial distributions for all secondaries (top) and muons (bottom) for different background origin for beam 2 at IP 1 and IP 5 of the HL-LHC.

the opposite distribution with peaks at $\phi = \pm\pi$ due to the flip in the crossing angle plane. The radial spatial distributions show maxima at R = 0 m for all secondaries and at R$\sim$ 1 m for muons only, all scenarios with an exponential decrease of background radiation for larger radii. Again, the integrated rates of background sources from beam 2 are presented in Table 4.2. The rate of beam background radiation induced from beam 2 is comparable for beam-gas and beam halo processes. The highest contribution comes from the IP 1 beam halo. The energy delivered to the interface plane by particles from beam-gas interactions is one to two orders of magnitude larger than from the beam halo background.

4.6 Summary

Table 4.2 shows the absolute rate of secondaries crossing the interface planes for each source of beam background as well as the rate of energy at the interface plane of IP 1 and IP 5. Each rate is counted at the 25 m diameter circular interface plane, using only particles with forward momentum. The rate of particles passing through the interface plane is of the order of 1 MHz for each beam-gas and beam halo contribute contributions. The energy

scaled rate from beam-gas is approximately 1×10^9 GeV Hz, two orders of magnitude larger than beam halo with a rate of 7×10^7 GeV Hz.

Table 4.2: Integrated rates of beam-gas (BG) and beam halo (BH) background sources for HL-LHC at IP 1 and IP 5 from beam 1 and beam 2 and their ratios divided by the smallest contribution. Ratio for total rate is divided by beam halo from beam 1 at IP 1 ($4.74 \times 10^5\,\mathrm{s}^{-1}$) and by beam halo from beam 2 at IP 5 ($2.88 \times 10^6\,\mathrm{GeV\,s}^{-1}$) for total energy rate.

IP	Beam direction	Source	Rate (s^{-1})	Ratio	Total Energy Rate (GeV s^{-1})	Ratio
IP 1	beam 1	BG	$(1.70 \pm 0.11) \times 10^6$	3.6	$(3.75 \pm 0.32) \times 10^8$	130.2
IP 1	beam 1	BH	$(4.74 \pm 0.13) \times 10^5$	1	$(1.80 \pm 0.05) \times 10^7$	6.3
IP 1	beam 2	BG	$(8.50 \pm 0.43) \times 10^5$	1.8	$(1.52 \pm 0.14) \times 10^8$	52.8
IP 1	beam 2	BH	$(8.95 \pm 0.01) \times 10^6$	18.9	$(3.80 \pm 0.09) \times 10^7$	13.2
IP 5	beam 1	BG	$(8.50 \pm 0.06) \times 10^5$	1.8	$(1.79 \pm 0.03) \times 10^8$	61.5
IP 5	beam 1	BH	$(3.16 \pm 0.01) \times 10^6$	6.7	$(1.80 \pm 0.05) \times 10^7$	6.3.
IP 5	beam 2	BG	$(1.70 \pm 0.01) \times 10^6$	3.6	$(3.35 \pm 0.07) \times 10^8$	116.3
IP 5	beam 2	BH	$(7.26 \pm 0.05) \times 10^5$	1.5	$(2.88 \pm 0.24) \times 10^6$	1

To conclude, the CMS experiment is expected to receive similar levels of background radiation compared to the ATLAS experiment from beam halo and beam-gas backgrounds in particle rate and energy delivered by these particles. For both CMS and ATLAS, the rates associated with beam-gas interactions are one to two orders of magnitude larger than for beam-halo processes for the energy rate, the particle rate is similar for both background sources. Looking at previous studies in [3], the previously simulated HL-LHC results are within one order of magnitude from the results presented in this chapter. Compared to Run 2 results, the beam halo background is at the same level as beam-gas. The results of IP 1 beam 2 beam halo are one order of magnitude higher than previously seen.

The following chapter demonstrates the propagation of non-collision background (NCB) between the interface plane and the ATLAS detector. It compares the level of the machine-induced background radiation to the output of the proton-proton collisions inside specific subdetectors.

5 | ATLAS detector response to beam background

Accelerator background radiation negatively affects the ATLAS detector. Elevated background rates can obscure physics signals and increase the detector occupancy resulting in an additional load to the trigger system and an overall decrease in the data acquisition efficiency of the detector. This chapter presents the ATLAS detector of the LHC and its future upgrade. Studies of beam background propagation between the ATLAS interface plane and its subdetectors are shown. The results include comparisons between different scenarios.

5.1 Propagation into the ATLAS detector

Previous publications of non-collision background (NCB) show that beam-gas induced background rates will remain at a similar level compared to Run 2 operations. At the same time, beam halo contribution should increase to reach the same rate as for beam-gas rates [3]. Possible implications on physics studies and detector occupancy must be understood. The effects of beam halo and beam-gas background on new sub-detectors, the inner tracker (ITk) [69] and the HGTD [70], and the currently used calorimeter system, and the possibility of using them as background identifiers are treated in this section.

The LHC accelerator contains two beams travelling in the opposite direction. Each beam includes bunches of protons in groups separated by a gap required for beam extraction. The bunches are set to collide with bunches from the second beam. A small fraction of bunches are non-colliding, *unpaired* bunches. Unpaired bunches have the nominal intensity as colliding bunches but do not collide with another bunch. As unpaired bunches traverse the interaction point, they generate beam-induced radiation not accompanied by proton-

collision radiation. As such, they provide an ideal probe for estimating the amplitude of beam-induced background.

The ITk is the upgrade of the central tracking system for the ATLAS detector, which contains two subsystems, the Pixel Detector (5 layers of silicon pixels) and the Strip Detector (4 barrel and 6 end-cap layers). The upgrade will ensure the detector can cope with the average of 200 pileup events and cover the pseudorapidity $|\eta| < 4$ while having excellent tracking performance during the HL-LHC operation. The HGTD is a new detector which will be installed in the gap between the LAr cryostats at $|z| = 3.5\,\mathrm{m}$ covering a rapidity region of $2.4 < |\eta| < 4.0$. The HGTD will improve the offline pileup rejection, measure the instantaneous luminosity and serve as a minimum bias trigger.

5.1.1 ATLAS trigger system

The ATLAS detector trigger and acquisition system (TDAQ) is responsible for whether or not to record an event from a proton-proton collision for later analysis. With the ATLAS instantaneous luminosity of up to $\mathcal{L} = 5 \times 10^{34}\,\mathrm{cm}^{-2}\,\mathrm{s}^{-1}$ (proposed operating scenario for HL-LHC), a robust trigger system is essential to filter the large amount of events available. With the LHC bunch-crossing rate of 40 MHz, the average recording rate is around 1 kHz (a factor of 0.0025%) [71]. The ATLAS trigger system is divided into a hardware Level-1 (L1) trigger and a software-based high-level trigger (HLT). The L1 trigger decreases the event rate from 40 MHz to 0.1 MHz, thanks to fast electronics capable of performing a coarse event reconstruction of the calorimeter and muon system. The HLT is a software trigger using offline algorithms. Events accepted by the HLT are written into different data streams to be used for various purposes (physics analysis, detector calibration and others), each stream storing only the necessary amount of information.

5.2 Simulation preparation

The simulation of beam background is done in two steps, propagation of the proton beam in the LHC beam pipes using the FLUKA and BDSIM software and transfer of the radiation information into the ATLAS detector software. Simulated hits in sensitive volumes are digitized and reconstructed into high-level physics objects. Beam behaviour within the beam pipe aperture, including background sources, is simulated with the SixTrack software. The beam loss distribution is then transferred to the FLUKA software, which contains the

whole geometry of the LHC tunnel and components and covers the particle transport and interactions with a matter for various accelerator applications. Results with specific settings of the LHC and HL-LHC (e.g. injection and collision settings) have been produced by the LHC collimation team and are available at [59]. The beam-induced backgrounds for HL-LHC include beam halo and beam-gas made with HL-LHC optics version 1.0 (made in 2013). A sample of beam halo events impacting on the TCTs was used for this study. BDSIM has the same capabilities and was used to simulate events not yet studied by FLUKA, including newer optics and accelerator hardware settings. BDSIM was used to create a sample of beam-gas induced background at the ATLAS interface plane using the optics version v1.5.

The results from both simulations are passed to the ATLAS Monte Carlo simulation chain at the interaction plane, $z = 22.6\,\mathrm{m}$ on either side of the interaction point. The process uses the following structure: event generation, detector simulation, digitisation and reconstruction. Event generation is done with Beam Halo Generator [72], created explicitly for the use with beam background. Afterwards, particles are propagated through the detector using the ATLAS Athena software using specific detector geometry configuration (version ATLAS-P2-ITK-20-02-00), and interactions with the sensitive material are recorded. Digitisation is specific to each sub-detector and mimics the electronic readout output. Finally, reconstruction includes pattern recognition and reconstruction of tracks, segments, vertices, cells and clusters in the different sub-detectors. Higher-level objects, such as missing energy estimation and jet identification, are also produced. The digitised events can be visualised in the ATLAS VP1 visualiser [73], a 3D interactive event display developed for use by the experiment. An example of a beam halo background hits in the Pixel detector is shown in Fig. 5.1.

The analysis of the ITk detector is achieved using the derivation framework explicitly created for the target background, the DAOD_IDNCB. It contains information about clusters in the ITk, separated into its Pixel and Strip parts. The HGTD detector is analysed using AOD samples with a custom hit timing simulation provided by the HGTD group. Each sample consists of 1×10^6 events. Each event represents one beam halo or beam-gas interaction. The beam halo samples are then overlaid with simulated physics collision with pileup $\mu = 200$ (200 minimum bias events per one bunch crossing).

The timing analysis of the HGTD provides hits information of beam halo events. The signal consists of many sources such as physics events, parasitic collisions, non-collision

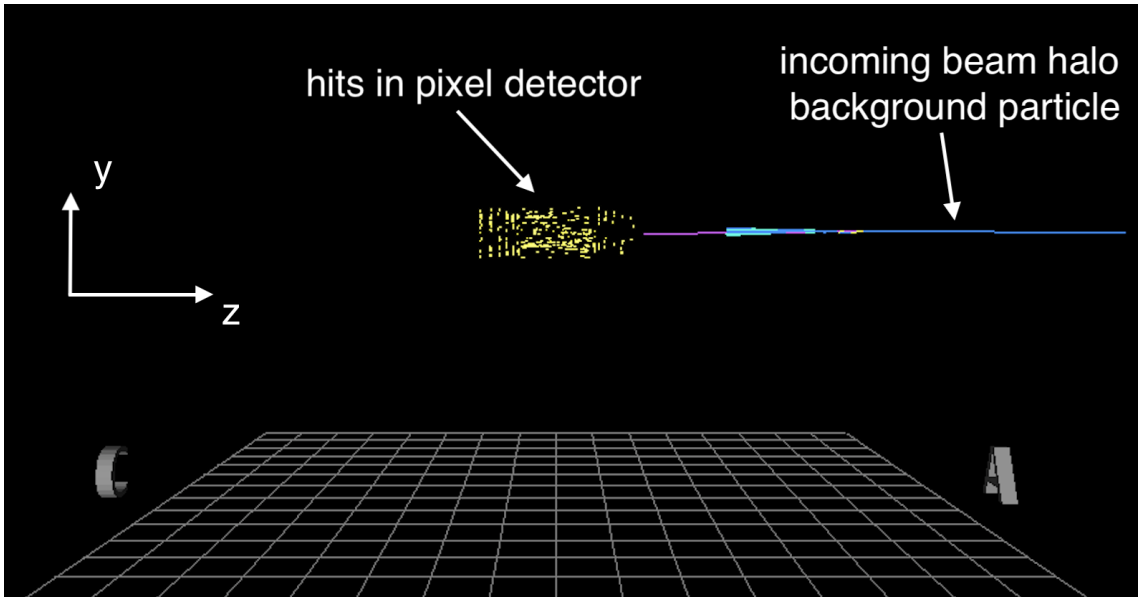

Figure 5.1: Event display of a beam halo background causing hits in the inner detector of ATLAS (yellow) using the VP1 visualiser.

background and other background events. Fig. 5.3 shows the origin of different events as they reach the HGTD. Parasitic collisions originate from a bunch after collision encountering the next bunch heading to the interaction point. As the bunch spacing is 25 ns, parasitic collisions are expected at 12 ns. The NCB events then enter the detector inside the beam pipe or outside and are expected from both sides.

The theoretical time of arrival based on the time-of-flight for various sources of hits is shown in Fig. 5.4. The origin of the time axis corresponds to the first hit of HGTD created by a collision signal. Non-collision events associated with a colliding bunch prior to interaction at IP 1 produce hits in the HGTD 23 ns earlier. A colliding bunch coming from the opposite side of ATLAS with its NCB particles are also a source of hits in the detector. Simultaneously, the next colliding bunch approaches the interaction point, and its non-collision background reaches the HGTD 1.6 ns after the collision events. The arrival time of the various events is in a short time window of 2 ns (except for the early bunch signal), which can be distinguished only by the excellent time resolution of the detector (30 ps). The collision signal and NCB coming with the collision bunch are indistinguishable from the point of arrival time at a small radius. However, the direction of the NCB events could provide a slight separation of the two signals at a high radius. The direction of arrival of NCB events is assumed uniform with respect to the radius of ATLAS. Still, in reality, only a few NCB events might appear at a larger radius.

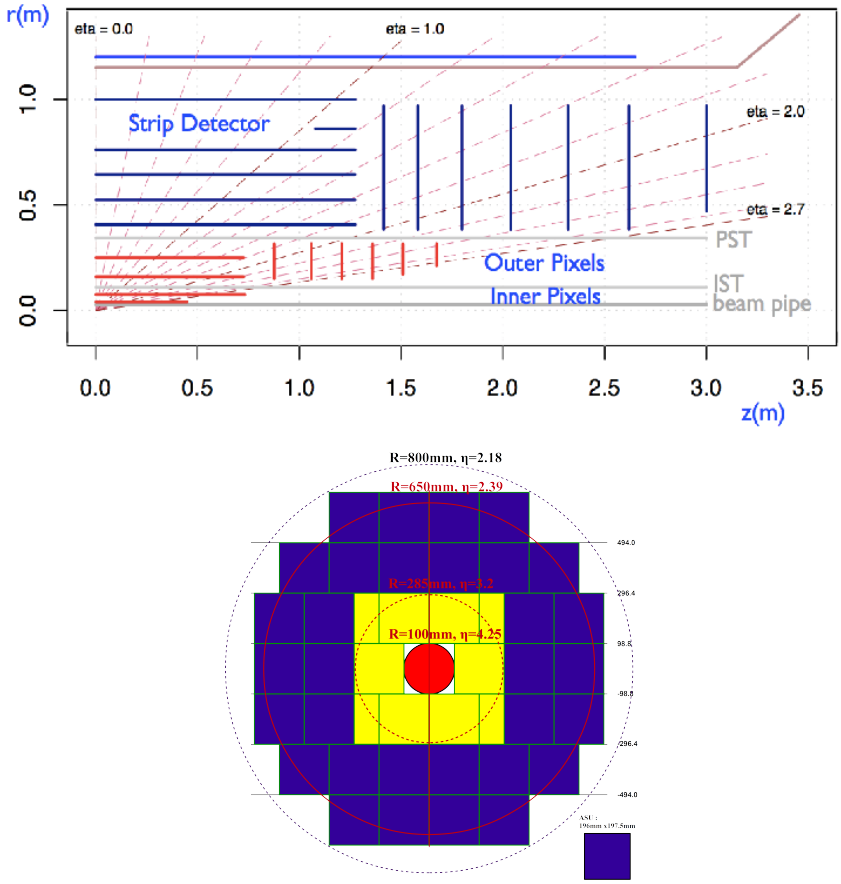

Figure 5.2: Geometry of the ITk with inclined duals (top) and layout of HGTD (bottom), both part of the ATLAS geometry version ATLAS-P2-ITK-20-02-00.

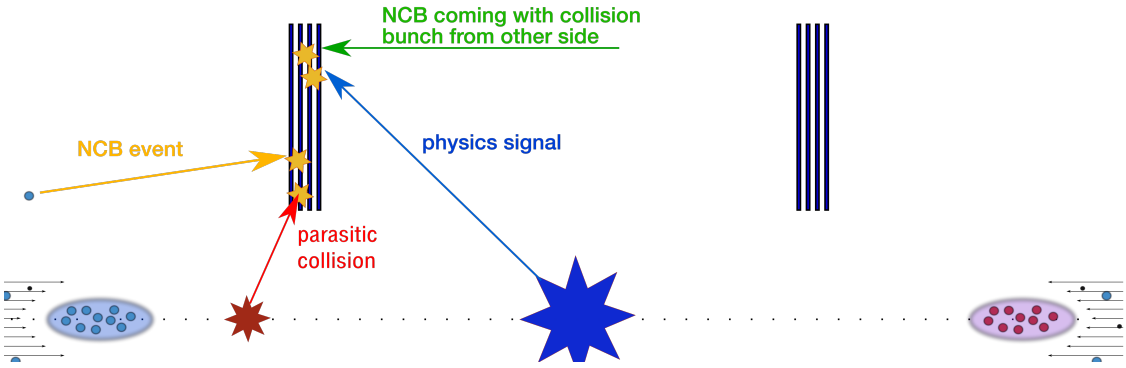

Figure 5.3: Events originating from NCB, parasitic collisions and physics collisions arriving at HGTD. The z position of the HGTD is such that signals from the collision point (blue and green lines) arrive almost at the same time as NCB events coming from opposite direction (yellow and red lines).

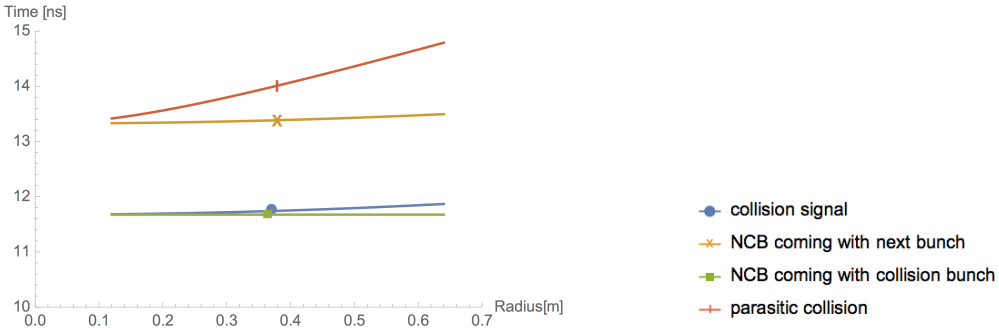

Figure 5.4: Theoretical time of arrival vs radius of the HGTD. The position of the detector is fixed at z = 3.5 m. Collision signal and NCB arriving with a collision bunch happen at 0 ns while NCB coming with next bunch and parasitic collision arrive 1.6 ns later. Colours are chosen to match Fig. 5.3 signal colours.

The simulated data were analysed to assess the impact of non-colliding particles on the ITk and HGTD detectors after the Phase-II upgrades. Beam halo study is done as a standalone background sample and overlaid with pileup. The ATLAS Geant4 detector geometry including the ITk (with inclined duals [69], Fig. 5.2) and the HGTD was used. The minimum kinetic energy for this simulation is set to 20 MeV to study all particles capable of propagating inside the detector. Beam-gas study uses the same geometry version of the ATLAS detector as the beam halo study but with a higher kinetic energy cut (20 GeV) to increase the number of background particles at a larger radius from the beamline and specifically muon background causing fake jets in the calorimeter.

5.3 Particles at the interface plane

An overview of the particles' spatial and energy distributions at the interface plane for the beam halo and beam-gas cases is presented to review the input before entering it into the ATLAS detector software. The particle kinematic characteristics, including the energy and spatial distributions, are shown in Figure 5.5. The first study is produced by the FLUKA software with the energy cut set to 20 MeV. In this case, the highest background contribution comes from low-energy particles with a small radius. The FLUKA azimuthal distribution has peaks at $\phi = \pm\pi/4$ and $3\pi/4$ which means most particles are uniformly distributed within the square tunnel aperture leading to the experimental hall. The second study uses the BDSIM software with an energy cut at 20 GeV. Pions are the most common secondaries up to 2 TeV, but they are only spaced up to a radius of 2 m. Most common particles with energy between 2 and 7 TeV are protons, which are concentrated even closer

to the beamline (radius $< 1\,\mathrm{m}$). Only muons are present for higher radii.

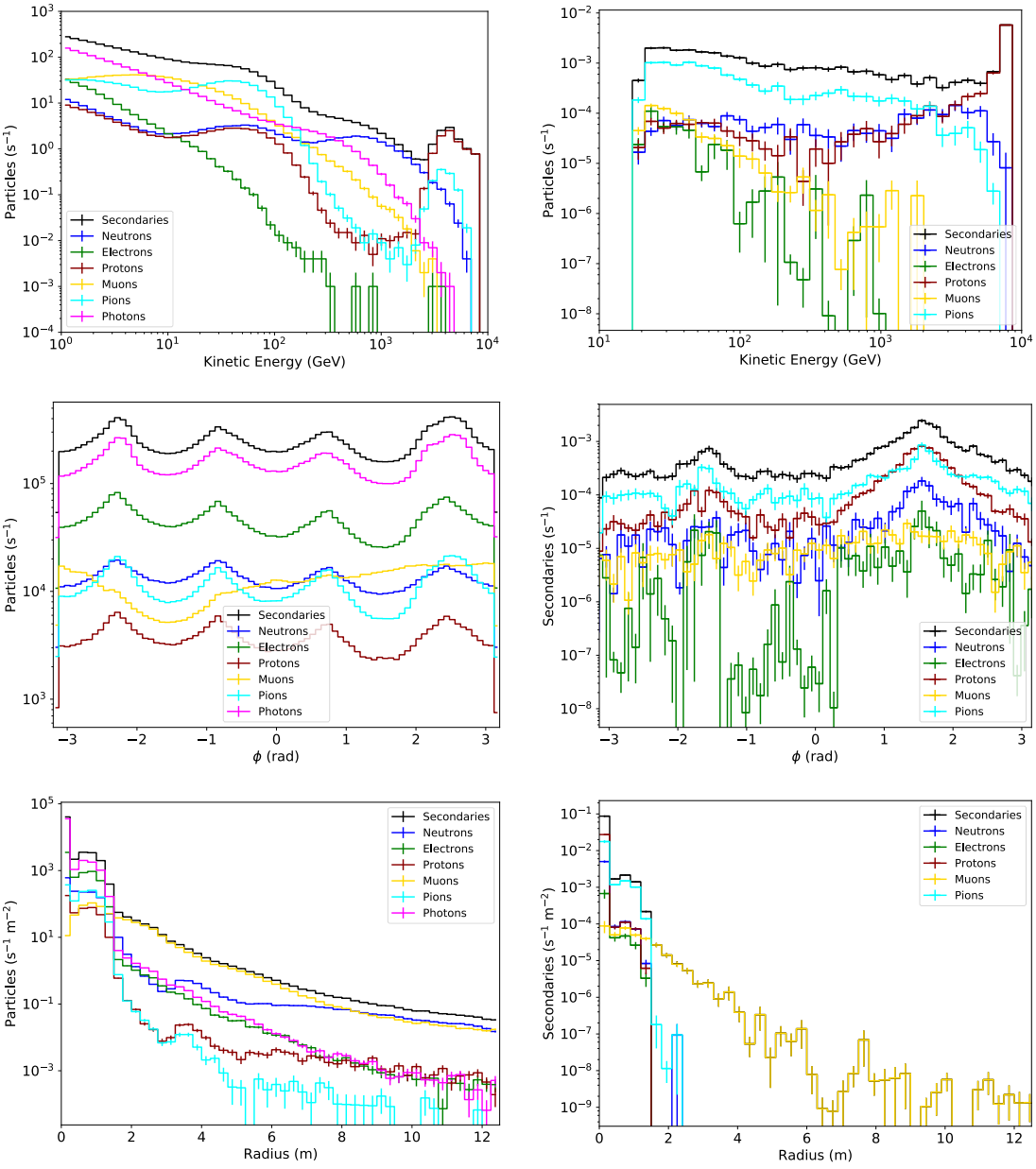

Figure 5.5: Particle distribution at the interface plane for FLUKA simulation (left, KE $> 20\,\mathrm{MeV}$) and BDSIM simulation (right, KE $> 20\,\mathrm{GeV}$) showing energy distributions (top), azimuthal spatial distributions (middle) and radial spatial distributions (bottom) for selected secondaries.

5.4 Particles inside the ATLAS detector

This section presents the results of the two studies, beam halo induced background prepared with FLUKA and beam-gas induced background prepared with BDSIM, and their effects

on the ATLAS detector.

5.4.1 Beam halo background

Beam halo events create clusters in the Pixel and silicon Strip detectors. A large concentration of hits is revealed in the outermost layer, as shown in the spatial distribution of background events shown in Fig 5.6 for Pixel and Strip elements. On the other hand, during high-pileup conditions, Pixel clusters are primarily in the innermost layer, and Strip clusters are distributed uniformly across their radius. Pileup events mainly originate at the IP while beam halo background contains fewer events closer to the IP and more travelling parallel to the beam pipe inside the detector. The Pixel detector pileup sample has 10^7 times more clusters than the no pileup sample. In the case of the Strip detector, the ratio is 10^5.

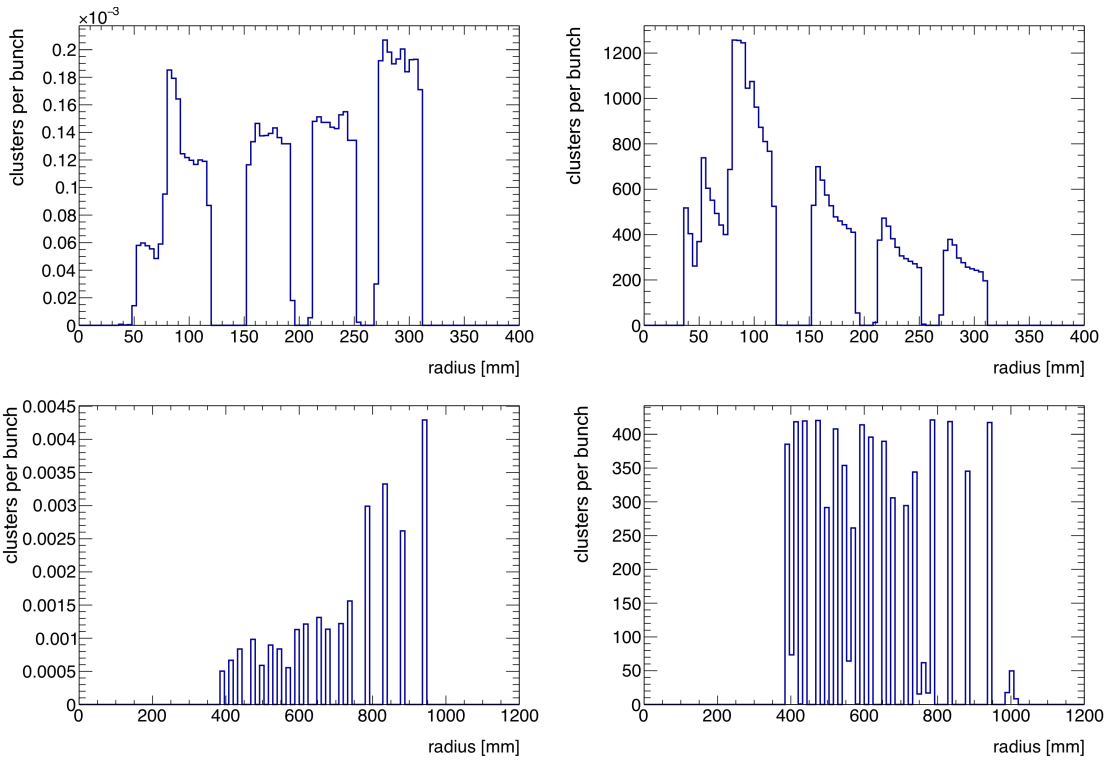

Figure 5.6: Pixel (top) and Strip (bottom) cluster radial spatial distribution without (left) and with (right) pileup.

The angular distribution in Fig. 5.7 shows a pattern in the background only sample with excess at $\phi = 0$. The pileup sample is distributed equally at all angles. The number of events from beam halo is negligible compared to the pileup sample.

The time of arrival to the HGTD as a function of the radial position around the beam

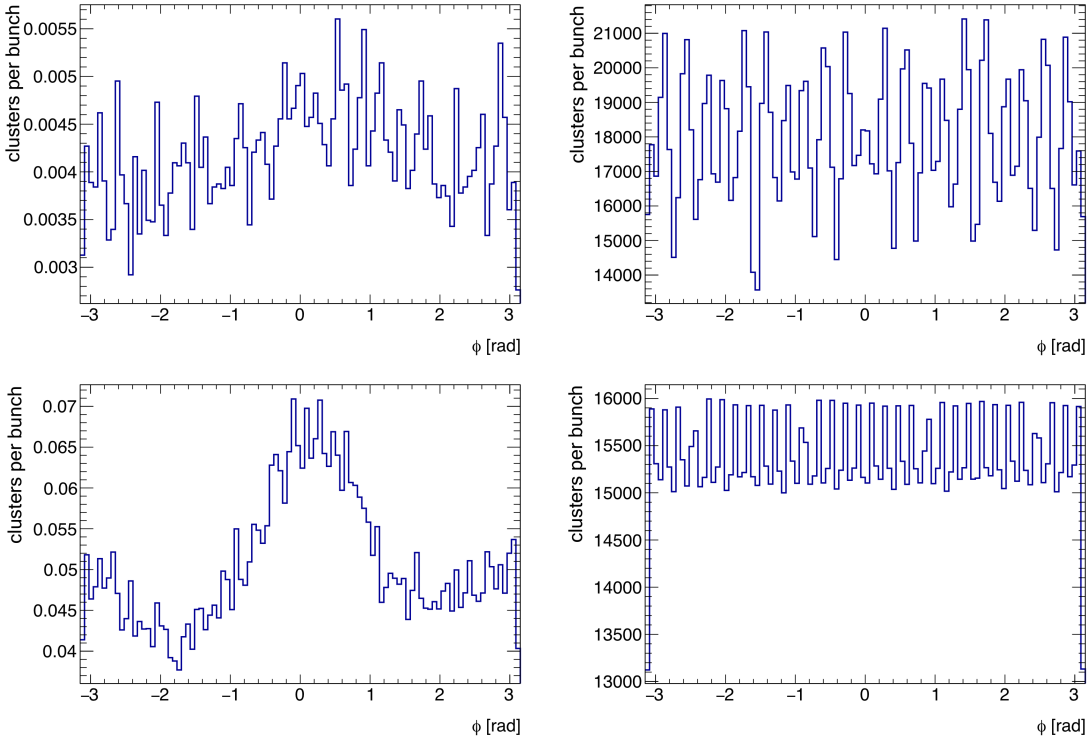

Figure 5.7: Pixel (top) and Strip (bottom) cluster angular distribution without (left) and with (right) pileup.

pipe is shown in Fig. 5.8 for no pileup and pileup samples. The first hit in the detector is centred at t = 0 ns. In this simulation, the beam background radiation is propagating into the detector from the positive z side, which is why hits at $z = 3.5$ m are shown at a negative time.

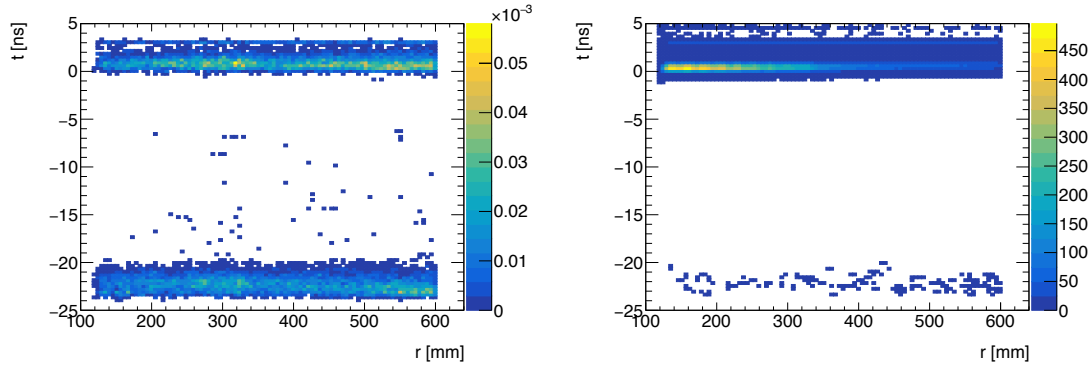

Figure 5.8: Time of arrival of beam halo hits in the HGTD detector as a function of radius for no pileup (left) and with pileup (right).

The beam halo particles produce hits in the thin layers of the HGTD in a time

window of about 3 ns and are distributed almost uniformly in radius with higher numbers of hits around 300 and 550 mm. The electronic readout time capabilities will limit the ability to record all of these hits in the actual detector. A longer readout time increases the size of the stored sample. However, the width of the time windows for the arrival time has not been determined at the moment of writing this thesis.

Compared to the beam halo only sample, the physics events with pileup $\mu = 200$ are mainly distributed around the origin of the r axis. Comparison between the radial distribution of hits for the pure sample and pileup sample is shown in Fig. 5.9 in which hits from the pure beam halo background sample increase radially until r = 300 mm and then again until r = 600 mm. The granularity of the HGTD pads is uniform across the detector (1.3 mm ×1.3 mm). However, each side of the HGTD detector has four layers of pads which are rotated in such a way that the region r < 320 mm averages about 3 hits per track and r > 320 mm averages only 2 hits per track [70]. The change of granularity is visible in the beam halo sample. The pileup sample hits are mainly located close to the beam pipe and decrease afterwards. The background sample without pileup increases with radius.

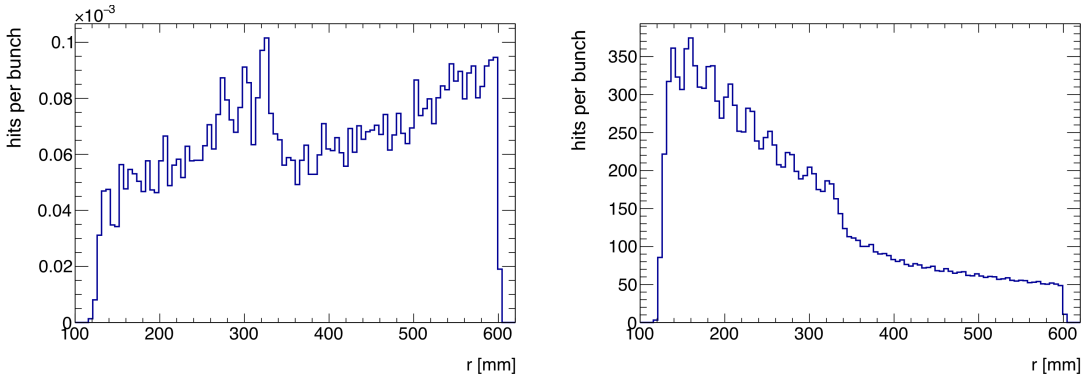

Figure 5.9: Radial distribution of HGTD hits for beam halo sample (left) and pileup sample (right) for $z < 0$ m.

The pileup sample produces $\sim 10^7$ more hits in the HGTD than the background sample, so during physics collisions, the beam halo background has a negligible contribution. Despite the significant difference between the pileup and background samples, it could be possible to discriminate for the non-collision background hits based on their time on arrival. Fig. 5.10 shows the pileup sample and the beam halo hits created by both beams. The background hits are indistinguishable within the pileup sample.

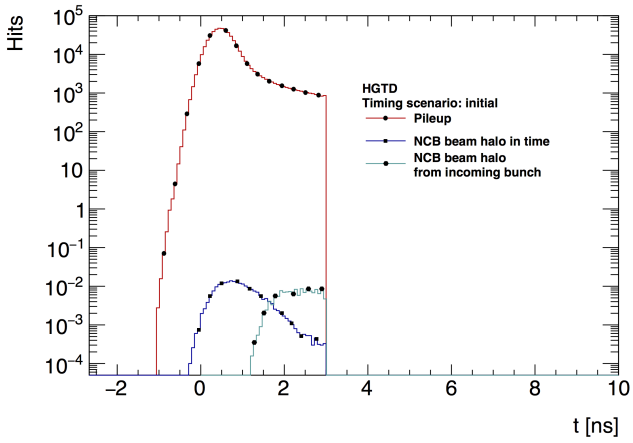

Figure 5.10: The time distribution, normalized per bunch, is shown for minimum bias pp pileup $\mu = 200$ (red with circles), the background halo samples of the colliding bunch (blue with squares) and the incoming next colliding bunch (cyan with hexagons). The distribution is cut at 3 ns to mimic the timing window of the electronics.

5.4.2 Beam-gas background

Beam-gas events also create clusters in the Pixel and silicon Strip detectors. The radial distribution of clusters shown in Fig. 5.11 reveals background radiation events concentrate in the innermost layer in the Pixel detector (opposite of beam halo background sample) and in the outermost layer in the Strips detector (similar to beam halo background sample). The azimuthal distribution of clusters in the Pixel detector shows a higher number of particles concentrated around $\phi = \pm\pi/2$, which is the opposite of the beam halo sample. This can be explained by the change of beam crossing angle between the different versions of the simulations: vertical plane in beam halo simulation and horizontal in beam-gas simulation. The clusters are uniformly distributed in the Strip detector.

The hits distribution in the HGTD detector is shown in Figure 5.12. The radial distribution shows a decrease of background radiation hits with radius, while the azimuthal distribution is uniform.

The time of arrival to the HGTD as a function of the radial distance from the beam pipe is shown in Figure 5.13. The first hits from beam background radiation arrive into the detector from the positive z-side, which is why hits at $z = 3.5$ m are shown at a negative time, time $t = 0$ ns is set with theoretical collision signal arrival. Both components are within the detector timing window, with in-time background arriving at approximately 1 ns before background radiation from the next incoming bunch.

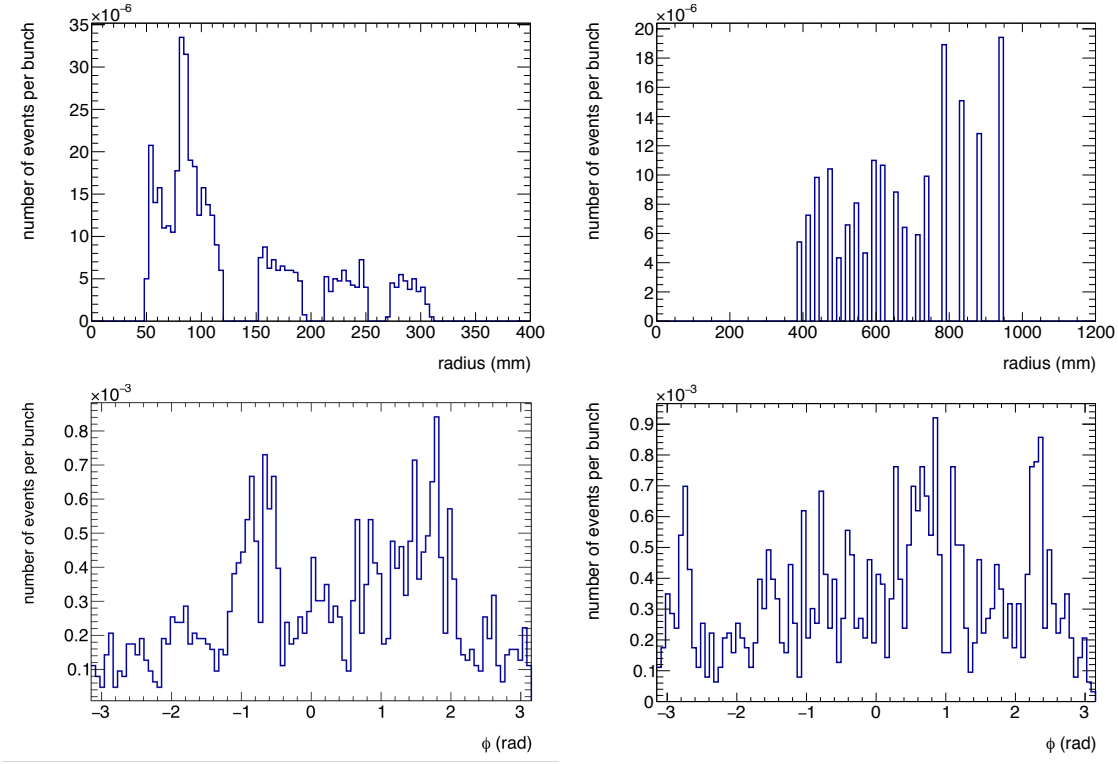

Figure 5.11: Pixel (left) and Strip (right) cluster radial (top) and azimuthal (bottom) distribution from beam-gas background.

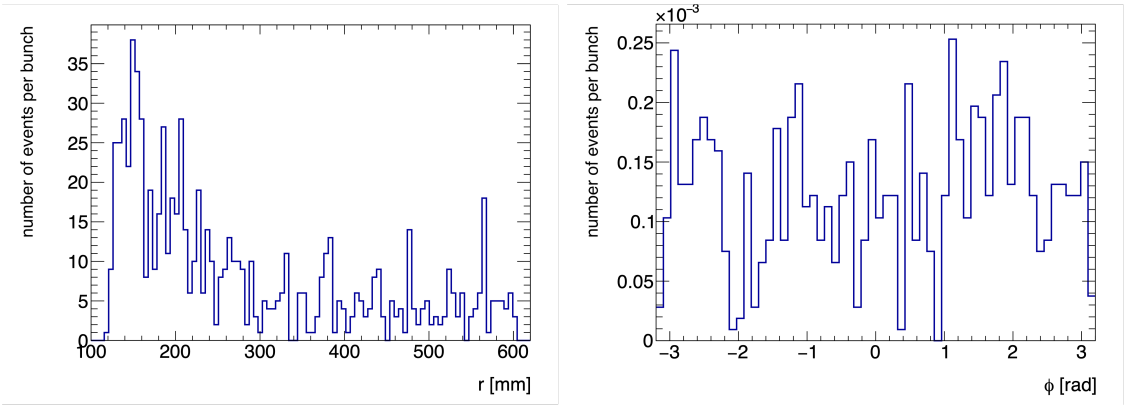

Figure 5.12: Radial (left) and azimuthal (right) distributions of hits in the HGTD for beam-gas background.

The number of hits in the HGTD from the beam-gas background is comparable within one order of magnitude to the beam halo results. Therefore, the beam-gas background also has a negligible effect on the physics analyses that use the inner detectors.

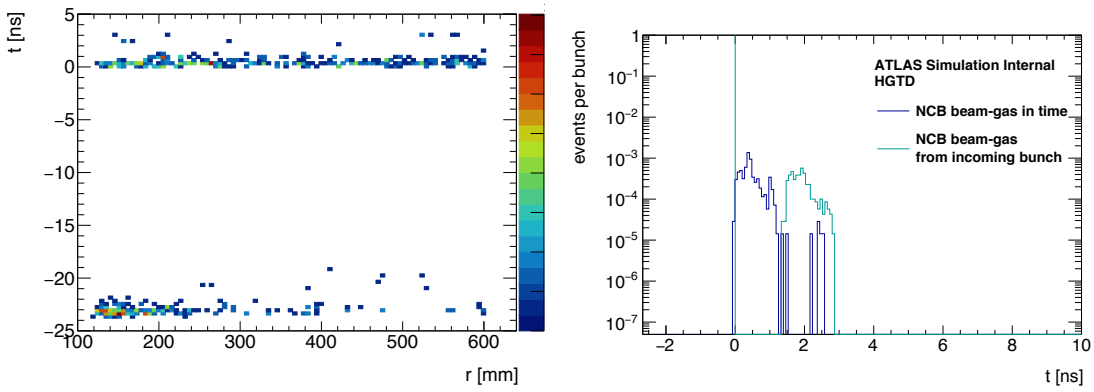

Figure 5.13: Time of beam-gas hits in the HGTD detector vs radius of the detector (left) and time distribution for beam-gas background from both sides of the ATLAS detector (right).

5.5 Summary

Beam halo and beam-gas events will produce negligible effect on the ITk and HGTD detectors during HL-LHC data taking for colliding bunches. However, the levels of NCB could be determined from unpaired bunches, which will provide background information without pileup. Unpaired bunches are extremely useful for establishing a baseline NCB rate. For example, the first bunch in a train can provide the information on NCB events coming from the outside of the ATLAS detector, while the last bunch in a train would supply the clean signal of NCB events coming from the direction of the collision point.

The timing structure of the NCB is not identical to the pileup time distribution. The impact of NCB on the ITk and HGTD will depend on the magnitude of its expected increase. The subdetectors will most likely only be able to contribute to the study of NCB for non-colliding bunches and during the commissioning phase of the HL-LHC before its nominal luminosity is reached.

Another experiment of the LHC, FASER, uses the product particles provided by proton-proton collisions at the ATLAS interaction point. However, as the detector is located 500 m from the collision point, a new particle transport simulation must be set up. This work is presented in the next chapter.

6 | Simulation of particle propagation to FASER detector

ForwArd Search ExpeRiment (FASER) is one of the many particle experiments at the LHC aimed at studying light and weakly coupled currently undiscovered particles and neutrino interactions. The proton-proton collisions at the ATLAS interaction point are the source of the signal. FASER is housed in a low background environment provided by approximately 100 m of rock and concrete, which only lets through weakly interacting particles. As the detector is located 500 m from the source of its signal, shown in Fig. 6.1, a particle transport simulation combining different tools must be set up. It must provide a proton-proton collision generator and particle transportation inside the LHC accelerator and the surrounding material. Particle event generators do not include undiscovered particles, so a Monte Carlo generator can only be used to estimate the number of neutrinos reaching the detector as well as any other particles which classify as background. To estimate the particle fluxes reaching the FASER detector, a detailed Geant4 model including magnetic fields, customised beam line elements, shielding and the accelerator tunnel geometry was prepared for use in BDSIM. Additionally, the contribution from the primary source of beam-induced background, the inelastic beam-gas interactions, throughout the beamline is presented. The simulation model is used to understand the propagation of the Standard Model particles, such as the point and process of origin. The simulated results will be compared to actual measured events in the future.

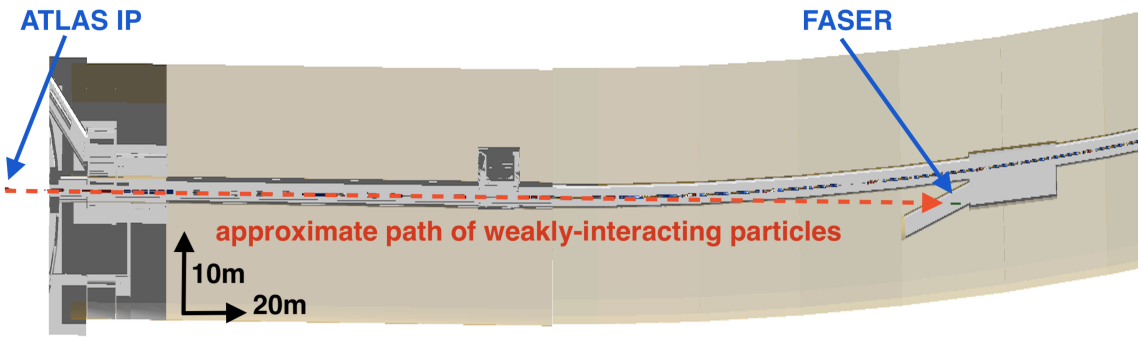

Figure 6.1: Model of the LHC tunnel section between ATLAS and FASER detectors with a sample path of a weakly-interacting particle.

6.1 Introduction

The physics goals of FASER are to search for Beyond Standard Model (BSM) particles, which are light and weakly coupled and also to study neutrinos at the LHC energy level. The cross-section for neutrino and hypothetical particle interactions is very small. Therefore, an accurate simulation is necessary to estimate the FASER sensitivity as a function of the integrated luminosity of ATLAS and the cross-section. BDSIM is used in this work because it can be supplied with custom geometries, use primary particles taken from an event generator and has options for tuning the physics and scoring. In particular, it allows for changing the production cuts and biasing, which is vital for studying particles with extremely low cross-sections. First, proton-proton collisions at the LHC generate a wide range of particles. These particles interact with the ATLAS detector and then the LHC tunnels and infrastructure. Of those, only high-energy muons and neutrinos remain and arrive at the FASER detector location. As FASER is interested in studying high-energy neutrinos, muons reaching FASER are considered as background. For the study of BSM particles, all SM particles, mainly neutrinos and muons, are considered background. The neutrino and muon fluences and interaction rates with the sensitive volumes of FASER must, therefore, be simulated to estimate the sensitivity of FASER to the detection of candidate BSM particles.

6.1.1 Simulation setup

The primary p-p collisions at the ATLAS IP are simulated using the SIBYLL model in the CRMC event generator. Generated particles are propagated from the IP towards FASER using BDSIM - tracking particles through an accelerator lattice and surrounding material.

Particles reaching the FASER interface plane (IFP) are passed to FASER detector software for reconstruction and analysis. The IFP is a virtual plane $25 \times 25\,\text{cm}$ in front of FASER detector. Another plane, called the FASER large sampler, is used to visualise and understand the general particle distributions at the FASER location. It uses a large plane of $20 \times 20\,\text{m}$. Events reaching the FASER detector from the direction of IP 8 (simulated beam-gas events) are collected by the background sampler, a plane of $20 \times 20\,\text{m}$ located behind the detector location. The locations of all samplers are shown in Fig. 6.2.

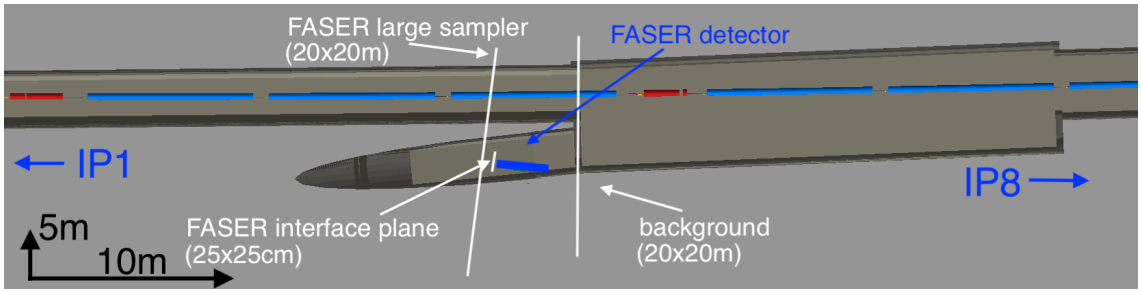

Figure 6.2: Locations of sampler planes (white) around the FASER detector.

The products of the event generator model are input into BDSIM simulation. The simulation uses the Geant4 reference physics (FTFP_BERT) list, a standard high-energy physics process list including electro-magnetic interactions, ion production and decay physics. Since neutrinos are one of the primary particles of interest, the default option of killing all neutrinos in Geant4 is turned off. Additional electro-magnetic interactions processes relevant to muons are added (GammaToMuons, PositronToMuons, PositronToHadrons, MuonNuclear, GammaNuclear). A kinetic energy cut of 10 GeV is used, keeping only particles that can be detected by the experiment.

While neutrinos propagate easily through matter for long distances, tunnel walls and soil material provide enough shielding for all other particles. Cross-section biasing ensures large enough statistics of muon background while keeping simulation time small. Specifically the decays of charged pions, which has decay modes with branching fraction larger than 0.1 ($\mu^+\nu_\mu$ and charge conjugate), and kaons with decay modes with branching fraction larger than 0.1 ($\mu^+\nu_\mu$, $\pi^+\pi^0$, $\pi^+\pi^+\pi^-$, $\pi^+\pi^0\pi^0$, $\pi^0 e^+\nu_e$, $\pi^0\mu^+\nu_\mu$ and charge conjugates) are biased.

An example of decay length for π^+ in different materials and for different energies and biasing factors is shown in Figure 6.3. The aim is to ensure all biased particles decay on the length-scale of the full model, $\sim 400\,\text{m}$ for vacuum and air materials and $\sim 100\,\text{m}$ for concrete and soil materials, while keeping the decay position more naturally spread out

throughout the section. In a vacuum, using the biasing factor of 50, 58% of pions interact within the first 100 m, while only 2% of pions decay with no biasing. Using only biasing factor of 50 in a vacuum and pion energies of 50, 100 and 500 GeV, the fraction of pions decaying within the 100 m are 83%, 58% and 16% respectively. In concrete, pion decay with biasing factors 10^4 and 10^3 cause all particles to decay within 2 and 20 m, respectively, while only 2% of unbiased particles decay within 100 m of concrete only due to the decay process. Using the biasing factor of 10^4, pions with energies $50 - 500$ GeV will all decay between $2 - 20$ m of concrete.

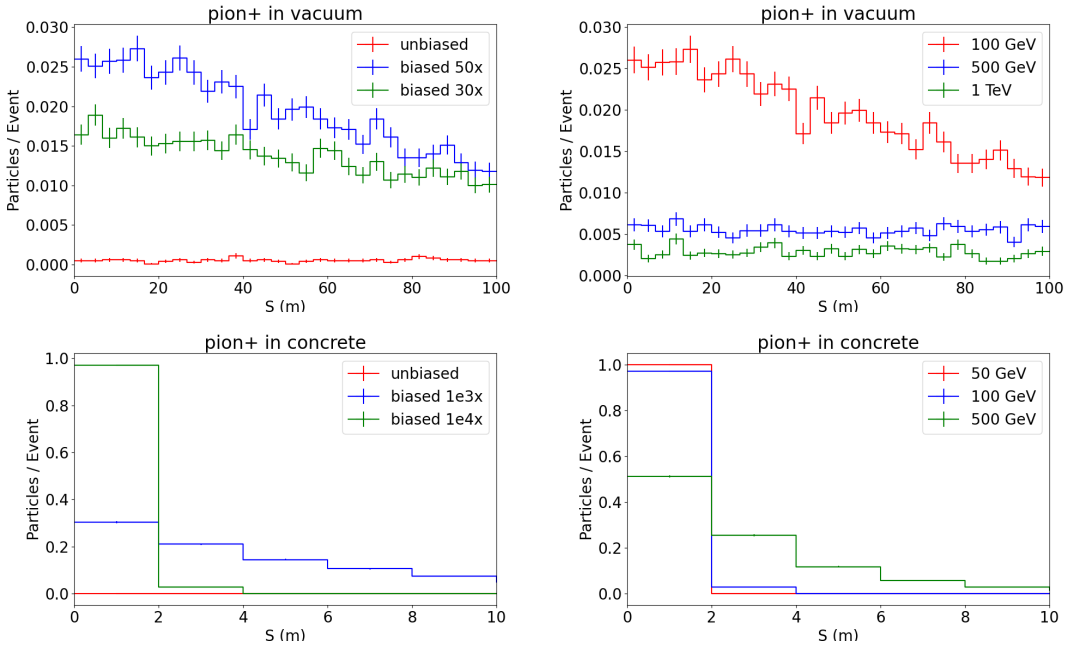

Figure 6.3: Number of pions per unit of length (S) in vacuum (top) and concrete (bottom) for different biasing factors (left) and different energies assuming biasing factor of 50 for vacuum and 10^4 for concrete (right). Only the decay process is allowed.

The biasing factors are summarized in Table 6.1. Both particle cross-sections in a vacuum are biased by a factor of 50 to ensure particles propagate further from the IP but decay before passing the FASER location. The vacuum in the accelerator beam pipes is not a pure vacuum and, therefore, has a non-zero cross-section. The particle cross-section in other materials is biased by a factor of 10^4 and 10^3 for charged pions and kaons, respectively, which ensures their decay within metres in soil or concrete.

More recently, muon splitting has been developed in BDSIM and can be used to study muon distributions and increase muon production in a specific region to accelerate the convergence of the simulation for estimators that involve muons. When a muon is

Table 6.1: Cross-section biasing factors for all biased particles in the FASER simulation.

particles	biasing factor in vacuum	biasing factor in material
$\pi^{\pm}$	50	10^4
$K^{\pm}$	50	10^3

produced during the simulation, the production process, decay or interaction is re-sampled several times. The splitting factor is the integer value which defines how many times the process is repeated. In this work, two groups of muons were defined, each having a different splitting factor. Muons with energies above 300 GeV are split by a factor of 50 and muons with energies between 50 and 300 GeV are split by a factor of 20. Lower energy muons (KE$<$ 50 GeV) cannot propagate through tens of metres of concrete and, therefore, are not used in this biasing method. When using cross-section biasing and muon splitting together in a simulation, the weights of each muon are compounded.

To cope with the sizeable BDSIM output, skimming was used to reduce the size of the simulation output to store only particles reaching the interface plane (IFP) of FASER. Then, the skimmed datasets were analysed to produce histograms of interest. The size and generation time of the raw and skimmed datasets are shown in Table 6.2.

Table 6.2: Event production overview.

simulation step	size	time for generation (5000 p-p collisions)	number of events stored
raw BDSIM file	1.5 GB	4732 s	5000
skimmed BDSIM file	55 MB	20 s	140
analysis histogram file	800 kB	146 s	-

6.1.2 Geometry model

The main model, presented in Chapter 2, which includes the geometry between the ATLAS detector and the FASER detector is used for particle tracking of primary proton-proton collisions with $\sqrt{s} = 13$ TeV. The complete model is shown in Fig. 2.2. The same model is used for beam-gas background studies for background originating from beam 2. Background radiation from beam 2 can possibly generate particles in the same direction as the expected signal particles at FASER. The geometry model used to simulate the background from beam 1 is shown in 2.6. The model starts at IP 8 and ends at the FASER location. Background radiation from beam 1 will produce particles coming from opposite directions,

possibly increasing the detector occupancy.

Photos from the location of FASER are shown in Figure 6.4 [1]. The photos show the status of the FASER detector at the beginning of LHC beam tests before Run 3. The experiment is now collecting data. After the end of the LHC operation, a new upgrade, FASER 2, is proposed to be installed for the HL-LHC program. FASER 2 will increase its sensitivity by four orders of magnitude by using a larger decay volume.

Figure 6.4: Location of FASER in the TI12 tunnel (top) and detail of the detector (bottom) before the start of Run 3.

[1] from the CERN Geographic Information System portal, taken on the 26th of January 2022

6.2 Particles reaching the FASER detector from the IP 1 collision point

The particle fluences for muons and neutrinos reaching the FASER interface plane are shown in Fig. 6.5 with outlines of the two tunnels drawn and looking towards IP 1. The muon flux has a minimum around the FASER detector location with peaks around the tunnel outlines and at the $y = 0\,\text{m}$ line, the line of the accelerator beamline. Neutrino flux peaks at the FASER detector, the line of sight from the IP 1 collision point. The IFP fluxes show a uniform distribution for both particle types. Neutrinos show only a large peak in distribution with fewer particles uniformly spaced around it, but muon distribution reveals the shadow of accelerator elements as well as tunnel walls.

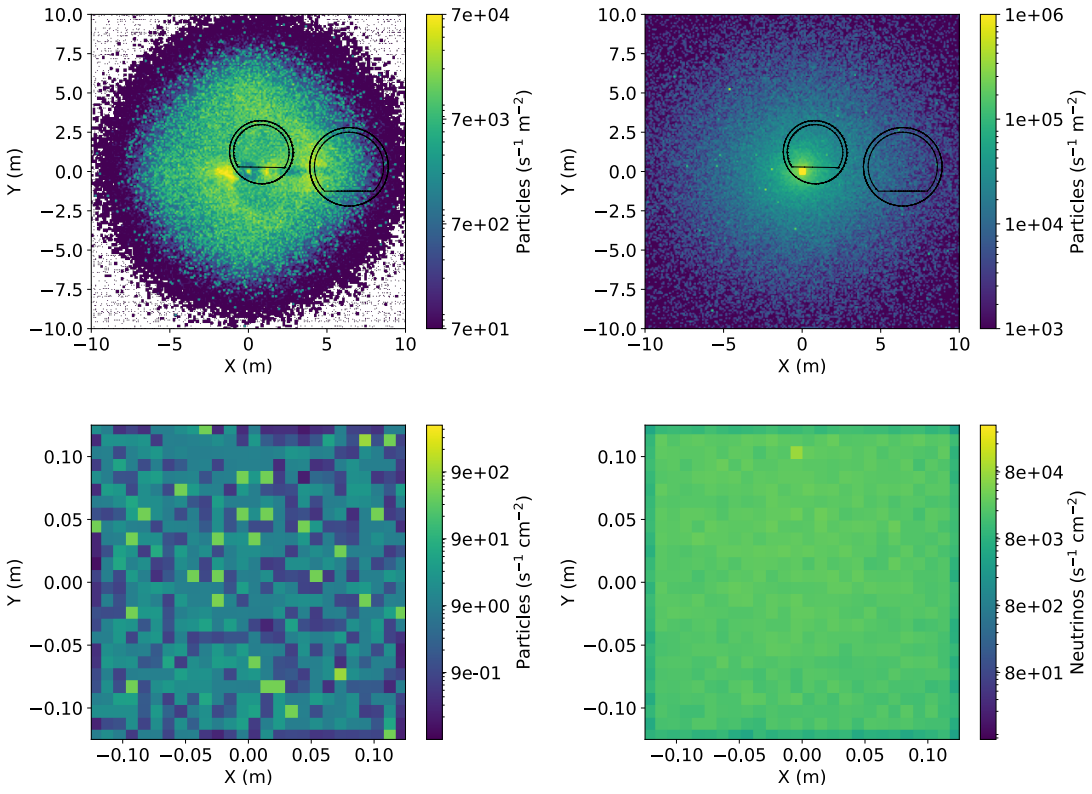

Figure 6.5: Particle fluxes at FASER created by proton-proton collisions at IP 1 at the large scoring plane (top) and the IFP (bottom) for muons (left) and neutrinos (right) using the luminosity of $2 \times 10^{34}\,\text{s}^{-1}\text{cm}^{-2}$.

The spectra of muons and neutrinos separated by charge and lepton generation at the FASER interface plane are shown in Fig. 6.6. Muon neutrinos make up the largest fraction of particle type (91%) reaching FASER.

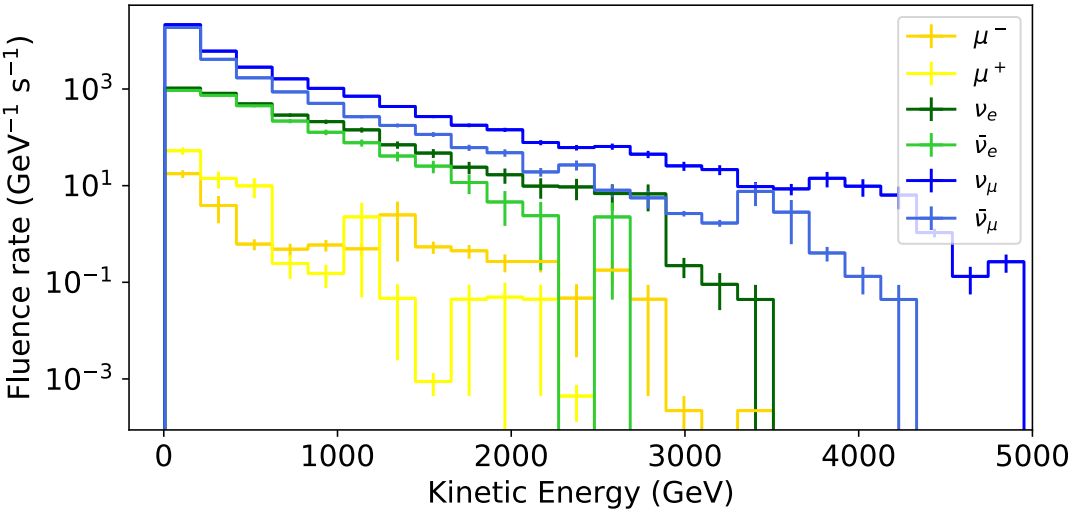

Figure 6.6: Particle spectra created by proton-proton collisions at IP 1 at the FASER IFP.

The spatial azimuthal distribution of muons and neutrinos at the FASER interface plane is shown in Fig. 6.7. The distribution is flat in ϕ, which shows that the particles are uniformly distributed in a cone centred at the line of sight. The radial spatial distribution is also uniform for neutrinos and muons. However, muons have a minimum at the centre of the detector.

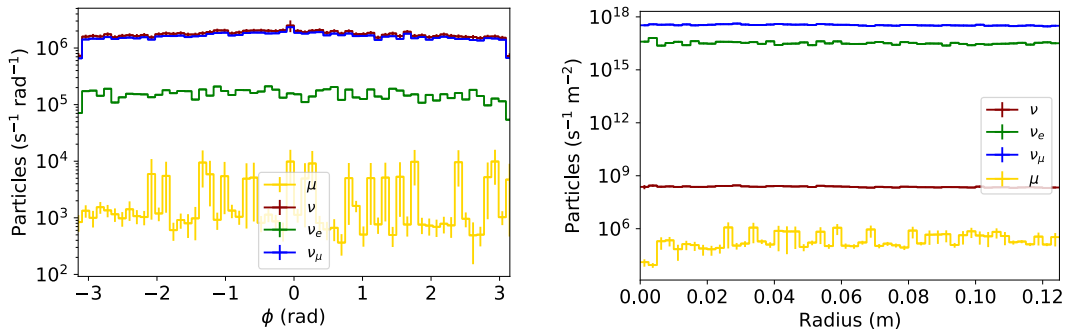

Figure 6.7: Azimuthal (left) and radial (right) spatial distributions of muons and neutrinos created by proton-proton collisions at IP 1 in front of the FASER detector.

The total flux at the FASER interface plane is $(2.23 \pm 0.04) \times 10^4\,\mathrm{s}^{-1}\,\mathrm{cm}^{-2}$ for the LHC operation with instantaneous luminosity of $2 \times 10^{34}\,\mathrm{s}^{-1}\,\mathrm{cm}^{-2}$. The error is the statistical error of the simulation. The systematic uncertainty is studied and evaluated in section 6.4.

6.3 Accelerator background radiation reaching the FASER detector

The beam-induced background is created everywhere around the LHC accelerator. The rate of background in the vicinity of the FASER detector is simulated and characterised in this section. The location of the FASER detector is far from collimators or aperture bottlenecks, so beam halo contribution is neglected.

For this simulation, two sources of background radiation were considered - background from beam 1 and beam 2. Both geometries were presented in detail in section 2.3.1. For beam 1, a simulation model of the 3 km long section between IP 8 and the TI12 tunnel entrance, written for the BDSIM software, was used. The background radiation is scored at the background sampler. For simulations of beam-gas interactions in beam 2, the main FASER model section between ATLAS and FASER was used, and the output is collected at the FASER large sampler. The output plane locations are shown in Fig. 6.2. The placements ensure all particles reaching the detector are scored, and background particles in the immediate area can also be estimated. In both scenarios, hydrogen gas with a uniform profile and density of 10^{13} molecules / m^3 with biasing of the proton inelastic cross-section was used. Neutrinos are not considered in these simulations. The results are scaled by the beam-gas interaction rate calculated using equation 1.42.

6.3.1 Beam-gas background radiation originating from beam 1

The FASER detector does not have the same amount of shielding downstream (direction from IP 1 to IP 8), so particles created in the UJ12 room could easily reach it. These particles impinge FASER with a considerable divergence and are, therefore, very unlikely to intercept all the tracking planes, a necessary condition for the readout trigger. Nevertheless, hits from these background particles could significantly increase the detector occupancy. All sections of the LHC tunnel for which a significant contribution to the FASER background is expected are included.

The location of beam-gas interaction producing secondary particles reaching the background sampler omitting the LHC tunnel (only using 2×2 m cutout of the background sampler) is shown in Fig. 6.8. Particles created within ~ 400 m upstream of FASER are capable of reaching the detector. For muons, this distance is even smaller (~ 200 m). The distance is limited by the curvature of the LHC tunnel. Secondary particles with rigidity

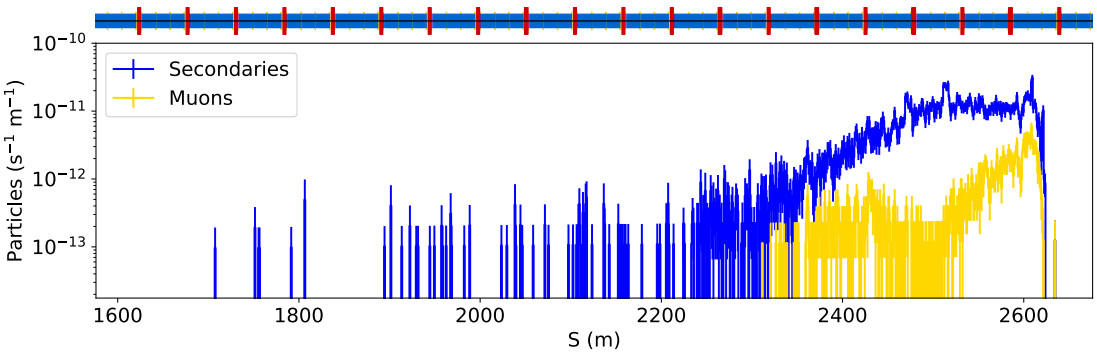

Figure 6.8: Distribution of the beam-gas interaction vertex position. S = 0 m is at IP 8, FASER is located at S = 2640 m.

close to the beam rigidity stay within the beam pipe or spread out slowly; the others will be absorbed by the beamline elements or the tunnel wall.

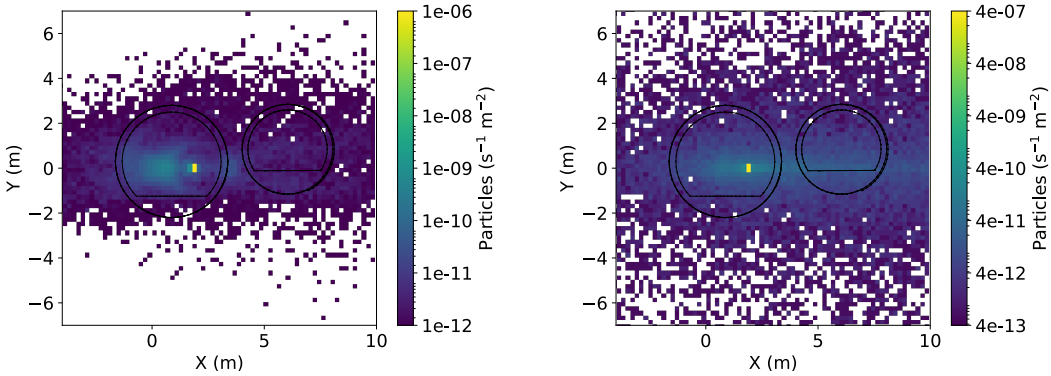

Figure 6.9: Particle fluxes at the background sampler produced by beam-gas interactions between IP 8 and FASER for charged (left) and neutral (right) particles.

The flux of particles at the background sampler is shown in Fig. 6.9. The highest intensities of background radiation are scored inside or near the beam pipe with a large spread of few and lower energy particles in the horizontal plane. Charged particles are mainly concentrated within the LHC tunnel. Neutral particles are spread in the horizontal plane also inside the TI12 tunnel. The approximate rate of beam-gas radiation at the FASER location is $10^{-11}\,\mathrm{s}^{-1}\,\mathrm{m}^{-2}$ for the LHC Run 3 conditions, which is negligible compared to the signal rate. Particles present in the background sampler are not filtered by their momentum vector. The fraction of particles actually reaching the detector will be much smaller.

6.3.2 Beam-gas background radiation originating from beam 2

The FASER detector has natural shielding provided by tens of metres of soil and metres of concrete between IP 1 and the TI12 location of FASER. However, we perform a simulation to estimate the beam-gas background rate from beam 2 reaching FASER despite the thick shielding.

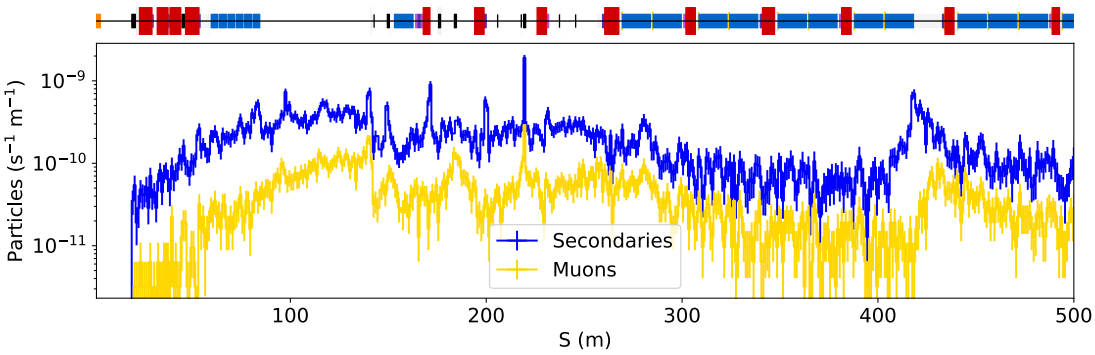

Figure 6.10: Location of beam-gas interaction of all secondaries and only muons reaching the FASER interface plane from beam 2.

The location of beam-gas interaction producing secondary particles and muons reaching the large sampler plane near the FASER detector is shown in Fig. 6.10. The figure shows that the few particles reaching FASER are generated uniformly between IP 1 and FASER with a slight increase between 400 and 450 m, at the border between the dispersion suppression section and the arc. This location contains an accelerator cell with a long drift space, so fewer particles are stopped by the magnet material.

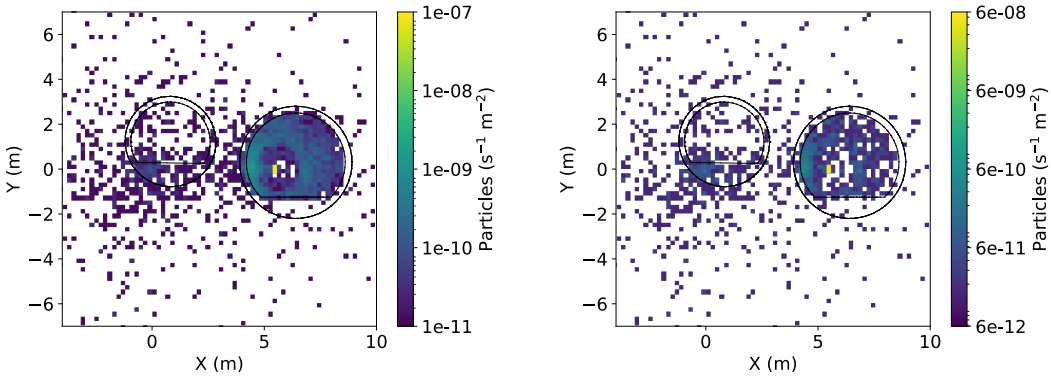

Figure 6.11: Particle fluxes at the background sampler produced by beam-gas interactions between IP 1 and FASER for charged (left) and neutral (right) particles.

The fluxes of secondary charged and neutral particles from the beam 2 and hydrogen

gas interaction locations are shown in Fig. 6.11 at the large sampler plane. Most background particles are concentrated inside the LHC beam pipe, and fewer are inside the LHC tunnel. At the location of FASER while using the LHC Run 3 operation parameters, the approximate rate of beam-gas radiation is $10^{-9}\,\mathrm{s}^{-1}\,\mathrm{m}^{-2}$. This rate is negligible compared to the signal rate from proton-proton collisions (presented in section 6.2).

6.4 Systematic uncertainties models

Different models were created to study the effects of varying parameters such as event generator, crossing angle of the colliding protons or geometry effects on the number of particles reaching the FASER detector. These parameters are either varying as intended by the LHC accelerator (crossing angle) or include possible uncertainties in the geometry (yoke fields and soil density) or not precisely defined for the specific used case and giving significant errors (event generator models). Reasonable values of the parameters are selected to estimate the error. The impact of the uncertainties of the parameters is then assessed from the simulations presented in this section. All simulations use the primary model of particle propagation between IP 1 and the FASER IFP.

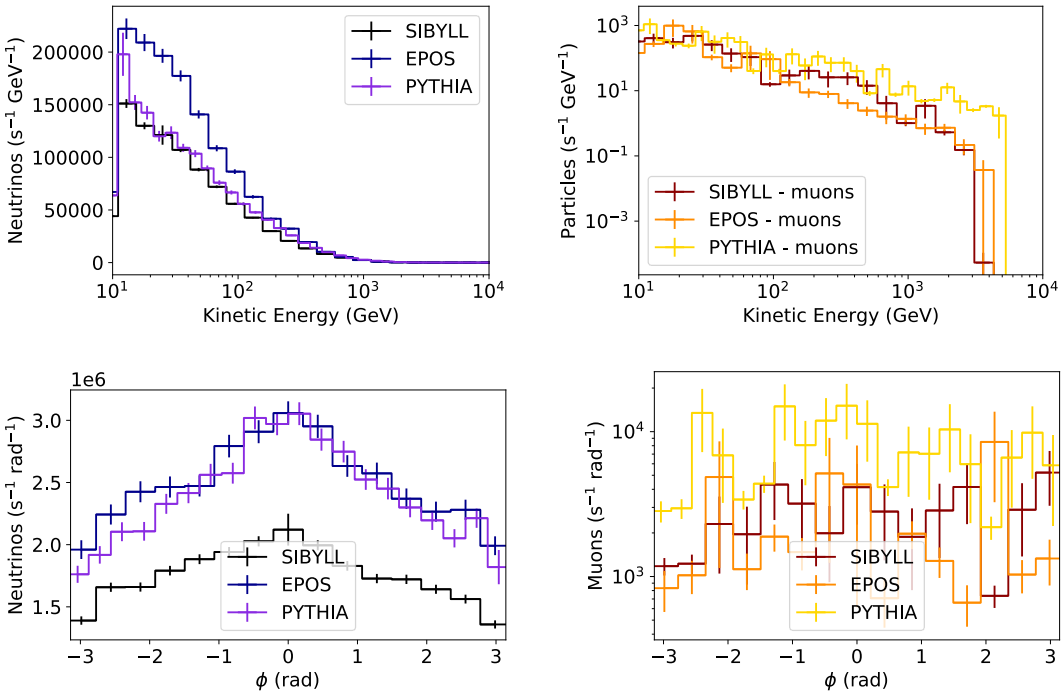

Figure 6.12: Energy (top) and azimuthal spatial (bottom) distributions for neutrinos (left) and muons (right) at the FASER interface plane for SIBYLL, EPOS and PYTHIA event generator models.

The effects of using a particular event generator for simulation studies at FASER detector were studied using the SIBYLL, EPOS and PYTHIA models of the CRMC event generator. All previously shown results used the SIBYLL model. All models include hadronic interaction models applicable at the LHC energy scale. Particle spectra from simulations using different event generators are shown in Fig. 6.12. EPOS produces more neutrinos at FASER compared to PYTHIA and SIBYLL, while PYTHIA produces almost double the muons compared to EPOS and SIBYLL. The number of particles decreases exponentially with energy with a maximum at $\sim 200\,\text{GeV}$. The azimuthal spatial distribution peaks at $\phi = 0\,\text{rad}$, which is expected as the FASER detector is at the line of sight from IP 1 collision point. The muons are uniformly distributed in azimuthal angle.

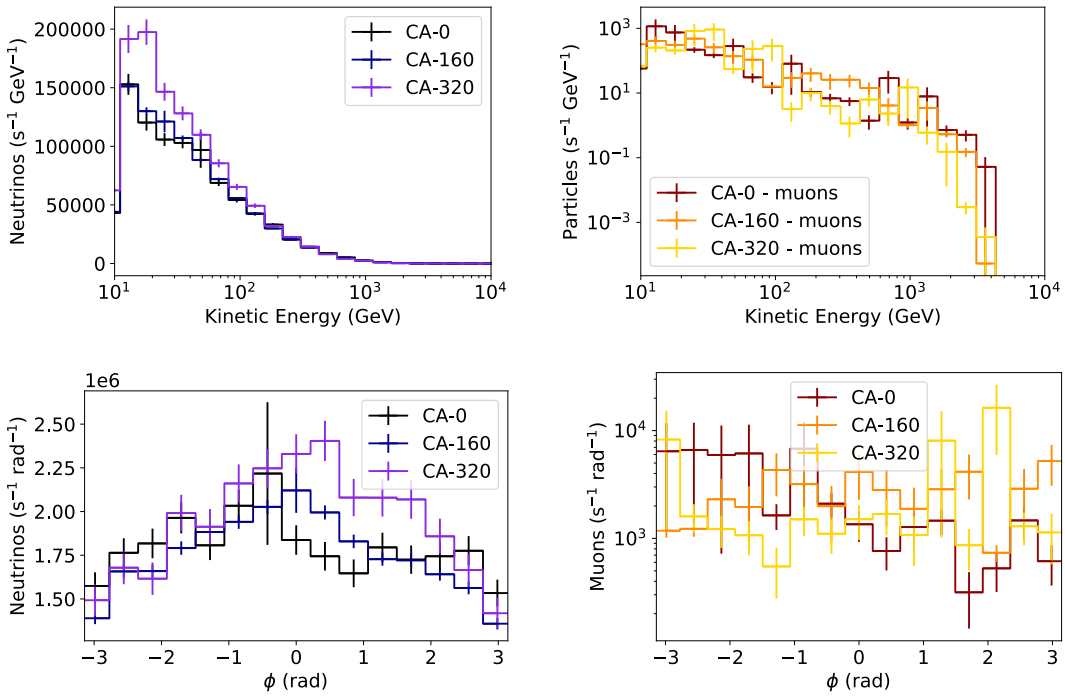

Figure 6.13: Energy (top) and azimuthal spatial (bottom) distributions for neutrinos (left) and muons (right) at the FASER interface plane for crossing angle 0, 160 and 320 μrad.

A study of the effects of varying the crossing angle at the IP 1 on particles near the FASER detector was performed since the crossing angle is regularly changed during LHC operations as a way to stabilise the luminosity. The comparison of the effects of crossing angle on particle spectra are shown in Fig. 6.13 using the crossing angle values of 0, 160 and 320 μrad. 160 μrad is the default crossing angle during LHC operation and for all simulations. The crossing angle changes the spatial distribution of neutrinos, and the peak shifts to $\phi > 0$ for crossing angle 320 μrad and to $\phi < 0$ for crossing angle

0 μrad. The collision plane at ATLAS is in the vertical plane, so as the angle increases, the centre of the neutrino distribution shifts in the positive y direction. A similar shift is also observed for muons with larger angle variations. The integrated number of neutrinos and muons reaching the scoring plane does not change within the simulation errors. The systematic error associated with changes in the crossing angle on the number of particles reaching FASER is taken as the standard deviation of the variations of that number for different crossing angles, giving $1.026 \times 10^3\,\mathrm{s}^{-1}\,\mathrm{cm}^{-2}$. The results of simulations using the crossing angle values of 0, 80, 160, 240 and 320 μrad are included in the standard deviation calculation.

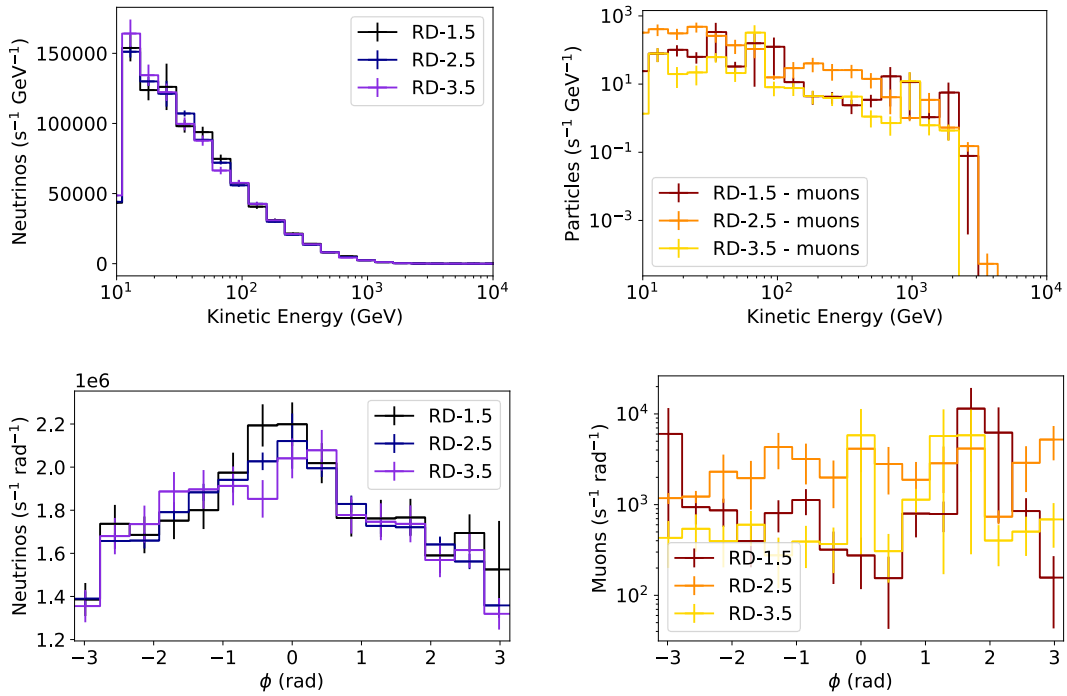

Figure 6.14: Energy (top) and azimuthal spatial (bottom) distributions for neutrinos (left) and muons (right) at the FASER interface plane for rock density of 1.5, 2.5 and 3.5 t / m^3.

Geometry models with different density of the soil material were used to evaluate systematic uncertainty since particles reaching FASER detector travel through approximately 100 m of soil. The density of the soil material is determined through geotechnical scans. A rock density of 2.5 t / m^3 is the average density value in the region around ATLAS and is the default for all simulations [60]. A uniform density of the material was assumed. To explore a range of possible densities, the values of 1.5, 2.0, 3.0 and 3.5 t / m^3 were chosen in addition to the default density of 2.5 t / m^3. A comparison of the effects of rock density on the particle spectra is shown in Fig. 6.14. The results show equal neutrino and

muon numbers within the simulation errors, only the largest density of $3.5\,\mathrm{t}\,/\,\mathrm{m}^3$ leads to an increased number of muons at FASER. The component of the systematic uncertainty due to the rock density variation for all particles reaching FASER is taken as the standard deviation of the variations on the number of particles, giving $3.24 \times 10^2\,\mathrm{s}^{-1}\,\mathrm{cm}^{-2}$.

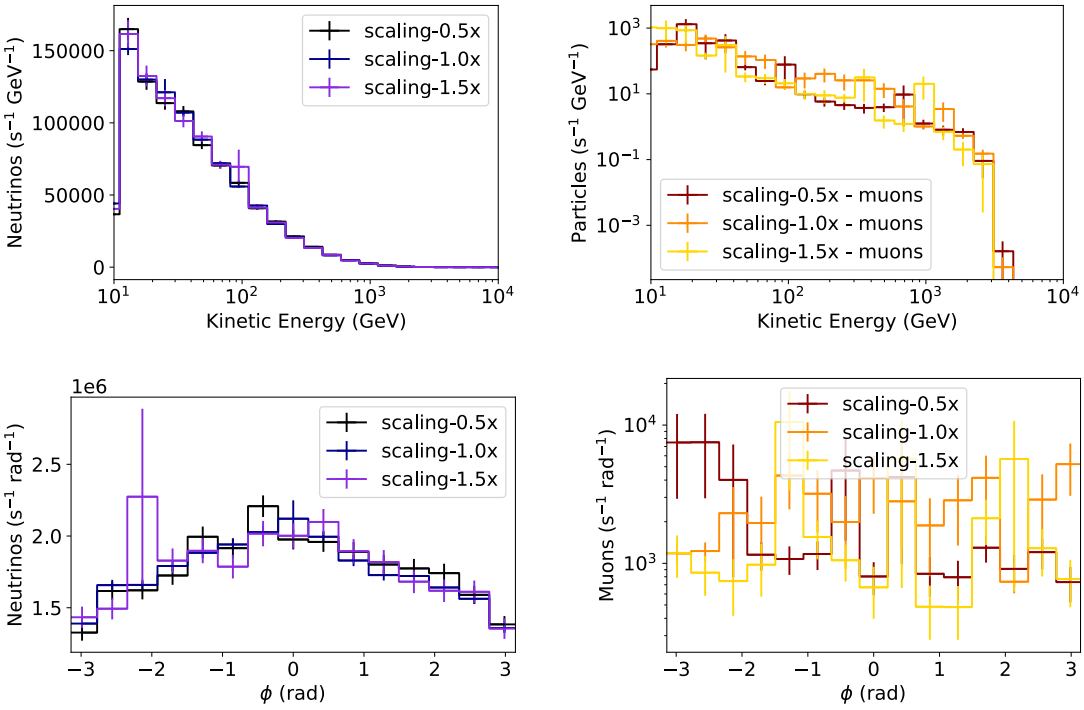

Figure 6.15: Energy (top) and azimuthal spatial (bottom) distributions of neutrinos (left) and muons (right) at the FASER interface plane for yoke field strength scales of 0.5, 1.0 and 2.0.

Finally, different strengths of yoke fields were used to investigate the systematic uncertainty of the model. Throughout the accelerator, the yoke field strength value for dipoles and quadrupoles was multiplied by a scaling parameter, using 0.5, 0.75, 1.0, 1.25, and 1.5. The default yoke field, corresponding to the scaling parameter of 1.0, was created using an LHC-specific field map. The energy and azimuthal distributions in Fig. 6.15 show the effects of yoke field strength on neutrino and muon spectra at the FASER IFP. The number of neutrinos and muons is within 2 sigmas for all scaling parameters. The spatial spectra show differences in muon azimuthal distribution but without a clear trend. The component of the systematic uncertainty due to yoke field scaling for all particles reaching the FASER detector calculated using the standard deviation is $2.73 \times 10^2\,\mathrm{s}^{-1}\,\mathrm{cm}^{-2}$.

Results of the parameter scan are summarized in Table 6.3. The total systematic uncertainty is equal to $1.11 \times 10^3\,\mathrm{s}^{-1}\,\mathrm{cm}^{-2}$, the same order of magnitude as the statistical

uncertainty. The systematic uncertainty is within one order of magnitude of the statistical uncertainty and, as such, can be considered negligible. The only studied case where the systematic uncertainty is more significant than the systematic is the crossing angle and specifically with value $320\,\mu$rad. An updated simulation with a larger event size should be performed.

Table 6.3: Parameters and particle fluxes with statistical error for different models used for estimating systematic uncertainties of the FASER model.

event generator model	crossing angle (μrad)	rock density (t / m^3)	yoke fields factor	μ flux (s^{-1} cm^{-2})	ν_e flux (s^{-1} cm^{-2})	ν_μ flux (s^{-1} cm^{-2})
SIBYLL	160	2.5	1	$(3.55 \pm 1.29) \times 10^1$	$(1.91 \pm 0.20) \times 10^3$	$(2.04 \pm 0.06) \times 10^4$
EPOS	160	2.5	1	$(2.93 \pm 0.95) \times 10^1$	$(2.08 \pm 0.33) \times 10^3$	$(2.98 \pm 0.11) \times 10^4$
PYTHIA	160	2.5	1	$(1.04 \pm 0.47) \times 10^2$	$(2.14 \pm 0.35) \times 10^3$	$(2.79 \pm 0.10) \times 10^4$
SIBYLL	0	2.5	1	$(4.08 \pm 2.56) \times 10^1$	$(1.96 \pm 0.45) \times 10^3$	$(2.09 \pm 0.13) \times 10^4$
SIBYLL	80	2.5	1	$(3.34 \pm 1.62) \times 10^1$	$(1.93 \pm 0.43) \times 10^3$	$(2.06 \pm 0.11) \times 10^4$
SIBYLL	240	2.5	1	$(2.90 \pm 1.65) \times 10^1$	$(1.87 \pm 0.44) \times 10^3$	$(2.08 \pm 0.12) \times 10^4$
SIBYLL	320	2.5	1	$(4.89 \pm 2.44) \times 10^1$	$(2.07 \pm 0.48) \times 10^3$	$(2.28 \pm 0.13) \times 10^4$
SIBYLL	160	1.5	1	$(3.06 \pm 2.51) \times 10^1$	$(2.02 \pm 0.46) \times 10^3$	$(2.06 \pm 0.12) \times 10^4$
SIBYLL	160	2.0	1	$(3.09 \pm 1.29) \times 10^1$	$(1.89 \pm 0.38) \times 10^3$	$(2.03 \pm 0.09) \times 10^4$
SIBYLL	160	3.0	1	$(2.80 \pm 1.98) \times 10^1$	$(1.93 \pm 0.42) \times 10^3$	$(2.10 \pm 0.11) \times 10^4$
SIBYLL	160	3.5	1	$(1.75 \pm 1.34) \times 10^1$	$(1.91 \pm 0.42) \times 10^3$	$(2.03 \pm 0.11) \times 10^4$
SIBYLL	160	2.5	0.5	$(3.05 \pm 1.23) \times 10^1$	$(1.99 \pm 0.34) \times 10^3$	$(2.06 \pm 0.09) \times 10^4$
SIBYLL	160	2.5	0.75	$(3.39 \pm 1.63) \times 10^1$	$(1.93 \pm 0.40) \times 10^3$	$(2.04 \pm 0.11) \times 10^4$
SIBYLL	160	2.5	1.25	$(3.64 \pm 2.02) \times 10^1$	$(1.76 \pm 0.39) \times 10^3$	$(2.09 \pm 0.14) \times 10^4$
SIBYLL	160	2.5	1.5	$(3.04 \pm 1.82) \times 10^1$	$(1.85 \pm 0.39) \times 10^3$	$(2.11 \pm 0.11) \times 10^4$

6.5 Sweeper magnet study

Muons are considered background for the FASER experiment (as it focuses on BSM particles and neutrinos). It is considered to add a permanent magnet to filter part of the muons and thereby reduce the background. Simulation studies are necessary to assess the effectiveness of this measure. The magnet would be placed at about 350 m downstream from the ATLAS interaction point and would bend the trajectory of muons and other charged particles heading directly for FASER from IP 1. The magnet would be 7 m long with 20 cm diameter and have a 1 T magnetic field. It will be made of SmCo surrounded by an iron yoke. The sweeper magnet is considered for use during the running of the HL-LHC. The magnet would be commissioned in time for HL-LHC operations during the Long Shutdown 3. The sweeper magnet geometry was added in the BDSIM model with a detailed dipole field to study the effects on the FASER background.

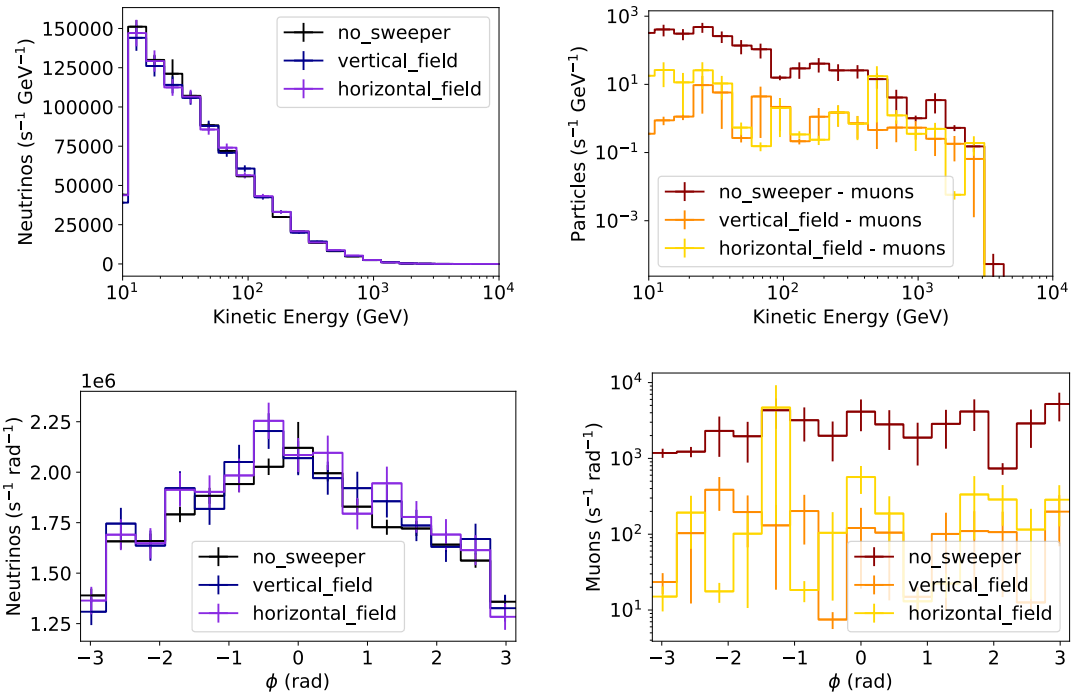

Figure 6.16: Energy (top) and azimuthal spatial (bottom) distributions of neutrinos (left) and muons (right) at the FASER interface plane for the default model (without sweeper magnet) and the model that includes the sweeper magnet with vertical and horizontal magnetic field lines.

The energy distributions of neutrinos and muons comparing the default model and the model with a sweeper magnet ON are shown in Fig. 6.16. The neutrino energy spectra are not affected by the added magnet as was expected, while the number of muons

decreases for either magnetic field orientation. The decrease is the desired effect as the muon background at FASER would be reduced by approximately 90%.

6.6 Summary

A simulation model for the propagation of muons and neutrinos created at the ATLAS IP travelling towards the FASER detector was created for use in BDSIM. It is a model capable of generating particles at the FASER detector location for various input parameters specific to the operation of the LHC during Run 3. Particle input is taken from the CRMC event generator simulating the proton-proton collisions at IP 1 but can also be supplied from other event generators. The particle fluxes are estimated at predefined scoring planes in front of the FASER detector.

The yield of muons at the FASER detector is very small; only 10 muons reach the detector for every million events simulated. It becomes computationally expensive to obtain a statistically meaningful sample. Therefore, biasing is necessary. We use a combination of cross-section biasing and muon splitting, both offered by BDSIM.

The accelerator induced background originating from beam-gas interactions in the LHC tunnel is negligible and is of the order of $10^{-10}\,\mathrm{s}^{-1}\,\mathrm{m}^{-2}$. Background radiation from beam 1 is very infrequent and either composed of neutral particles (neutrinos were excluded from the study) and thus wouldn't register in the detector tracking stations or charged particles which have much lower energy than the energy cut of the detector. In either case, background particles would not propagate through the whole detector and, therefore, not register as a track. Background radiation from beam 2 is shielded by metres of soil and is also negligible.

The total flux in front of FASER crossing the $25 \times 25\,\mathrm{cm}$ sampler plane is $2.233 \times 10^4 \pm 4.4 \times 10^2$ (stat.) $\pm 1.11 \times 10^3$ (syst.) $\mathrm{s}^{-1}\,\mathrm{cm}^{-2}$ for the LHC Run 3 operation with instantaneous luminosity of $2 \times 10^{34}\,\mathrm{s}^{-1}\,\mathrm{cm}^{-2}$. This result is found using the SIBYLL event generator model, crossing angle of $160\,\mu\mathrm{rad}$, rock density $2.5\,\mathrm{t}\,/\,\mathrm{m}^3$ and sample size of 10^6 events. The results are consistent within statistical error when compared to the EPOS and PYTHIA generator models. The fluence rates at the FASER detector have matching distributions but are higher by one order of magnitude compared to the similar study performed with FLUKA presented in the FASER technical proposal [74]. As the simulations have many varying input parameters such as event generator, material density

and others, we can assume they are not identical. The correct fluence rates will therefore be verified by measurements.

7 | Conclusion

Monte Carlo simulations of particle propagation to estimate background radiation levels were performed for the LHC and its future upgrade projects. The studies aimed to assess the beam-induced background levels affecting the ATLAS, CMS and FASER experiments. These studies are carried out by accounting for the latest accelerator optics and design configurations, thereby supplanting previous similar studies. The main scenarios studied in this thesis are the beam-gas and beam halo radiation. Both are types of beam-induced background and are the primary source of ATLAS and CMS non-collision background.

The geometry and accelerator optics settings provide the baseline for any particle accelerator transport simulation. However, another crucial part of beam-induced background simulations is the setup of geometry not only of the accelerator but also of the surroundings within a few meters where background radiation still propagates. A simulation model was created for particle propagation inside the accelerator, modelling the impact of the beam with the collimator jaws or the aperture extents and propagation inside beam line elements and their surroundings. This LHC and the HL-LHC model includes a high level of detail near the ATLAS and FASER detectors, the IP 1 straight tunnel section, and accelerator components. The straight tunnel geometry was converted from a previous FLUKA file, and the elements inside the tunnel and the remainder of the tunnel sections were created from scratch. The BDSIM toolkit is a Geant4-based software used for this work. It is a very versatile tool suitable for simulations of particle propagation inside or near an accelerator. Additional software tools were used in the model preparation, such as MADX, pyg4ometry, CRMC and SixTrack. Another multi-purpose accelerator simulation package, FLUKA, was used for results validation.

The NCB was evaluated at the interface plane of the ATLAS detector for different optics parameters foreseen during HL-LHC and HE-LHC operations. The interface plane corresponds to the outermost wall of the ATLAS experimental hall. Background levels cor-

responding to this configuration were evaluated for beam-gas and beam halo background for the nominal optics. Particularly of interest are particle and energy rates. Particle rate represents the total number of particles, while energy rate is defined as the total kinetic energy of the particle rate. Simulation results for different optics versions and β^* configurations were compared. The same studies were performed for background radiation reaching the CMS detector and compared to the ATLAS results. Based on the simulation results, the ATLAS experiment is expected to receive similar rates of background radiation hits as CMS for background originating from beam-gas and beam halo processes. For energy rate, the beam-gas background will exceed beam halo contribution by two orders of magnitude for both experiments. Such rates at the interface plane were expected and are deemed acceptable for HL-LHC operations and quality data taking by the experiments. The detector response must be simulated to evaluate the actual effect of these backgrounds. The HL-LHC and HE-LHC will require more simulation work in the future when actual machine parameters are determined. Up-to-date estimations for the beam-induced radiation levels should be available to ensure the safe operation of the accelerator complex. Simulation efforts drive the design of a safer and more efficient accelerator since reducing the radiation background results in less activation.

The effects of NCB on ATLAS data taking were estimated using the ATLAS software for HL-LHC operation parameters. The propagation of background radiation was studied inside the ITk, HGTD and the calorimeters. The results show that the impact of NCB on these subdetectors is small. These subdetectors will only be able to contribute to the study of NCB for non-colliding bunches and in the startup of the HL-LHC before nominal luminosity levels are reached. During standard collision operations, the physics signal overcomes the NCB by approximately six orders of magnitude. However, for rare physics searches, spurious hits could sometimes be interpreted offline as physics signal by the experiments. To verify that the amount of non-collision background stays within acceptable range, the levels of background need to be reviewed for each new optics settings and especially for future runs with different filling schemes with fewer non-colliding bunches. The design of the ATLAS subdetectors for HL-LHC is still evolving as they are being produced and tested so the newest geometry version should be reviewed for impacts from NCB. However, small size or material changes of the subdetectors are unlikely to alter their received radiation level. On the other hand, varying their detection time window could make them available for identification of the background radiation extent and propagation

and provide useful feedback to accelerator operators.

The FASER experiment intends to study neutrinos and other weakly-interacting, rare or new particles while suppressing background from Standard Model particles such as muons. A simulation of particle propagation of signal and background to the FASER detector, located in the arc section between IP 1 and IP 8, from the ATLAS experimental hall up to IP 8, was created and used in BDSIM. The signal consisting of neutrinos and background of muons comes from proton-proton collisions in IP 1. The simulation uses a Monte Carlo generator of the collisions, whose products are scored at the FASER detector location. The study considered many input parameters for running during the LHC Run 3, such as different crossing angles, particle generator models, and others. The neutrino and muon fluences were presented. The background radiation originating from beam-gas interactions in the LHC tunnel was also studied and was found negligible compared to FASER occupancy. The FASER simulation model developed for the study will be used for all collaboration simulation work in the future. The model can be improved by employing additional biasing methods which would decrease the overall simulation time such as by using cross-section biasing of specific physics process. The event generator and physics lists should also be reconsidered to allow for the production of tau neutrinos.

High energy particle accelerators have been in development for about one century. Since the beginning, they have pushed the frontier of fundamental particle and nuclear research. The LHC with a centre-of-mass (CoM) of 14 TeV is the world's largest, most powerful collider, but it can be complemented or exceeded by a few proposed projects. These projects include the Super Proton–Proton Collider (SPPC) with 75 TeV CoM, the Future Circular Collider (FCC-hh) with 100 TeV CoM or the $\mu^+\mu^-$ collider in the LHC tunnel with 14 TeV CoM. These accelerators would allow us to push the frontiers of physics and significantly advance technology. Significant research and development efforts must be made in superconducting magnet technology and RF technology. Since background radiation is expected to increase due to higher intensity and energy operation modes, progress must also be made in radiation hardened beam instrumentation and radiation protection. The development of advanced accelerator simulation tools is crucial in achieving these goals. These advances propagate beyond fundamental research into the industry (e.g. the Knowledge Transfer group at CERN) as research, and business collaborations are crucial for accelerator function.

The simulation packages mentioned in this thesis are used in beam simulations but

also in other scientific applications. BDSIM is also used in the hadron therapy medical accelerator design process, and FLUKA is widely used in radiation protection simulations and dosimetry. However, for a simulation tool to be relevant in the future, it must react and answer to scientific advances. BDSIM keeps updating based on the input of the developers and users, and a list of proposed features is being maintained. One current update focus is to supply symplectic tracking. With the increasing complexity of accelerators, it is likely, that BDSIM will still be relevant in the foreseeable future.

Acronyms and initialisms

ATLAS A Toroidal LHC Apparatus.

BCM Beam Conditions Monitor.

BDSIM Beam Delivery Simulation.

BIB beam-induced background.

BSM Beyond Standard Model.

CERN European Organization for Nuclear Research.

CMS Compact Muon Solenoid.

CoM centre-of-mass.

CRMC Cosmic Ray Monte Carlo.

DS dispersion suppressor.

FASER ForwArd Search ExpeRiment.

FCC Future Circular Collider.

FLUKA FLUktuierende KAskade.

GDML Geometry Description Markup Language.

HE-LHC High-Energy Large Hadron Collider.

HGTD High Granularity Timing Detector.

HL-LHC High-Luminosity Large Hadron Collider.

IFP interface plane.

IP interaction point.

IR interaction region.

ITk inner tracker.

LEP Large Electron-Positron Collider.

LHC Large Hadron Collider.

LHCb Large Hadron Collider beauty.

NCB non-collision background.

RF radio-frequency.

SM Standard Model.

SPS Super Proton Synchrotron.

TAN Target Absorber Neutral.

TAS Target Absorber Secondary.

TCP Target Collimator Primary.

TCT Target Collimator Tertiary.

A | Distribution of hits on TCTs in IR 1 and IR 5

All hits distributions and their energy spread on TCTs in IR 1 (beams 1 and 2 for $\beta^* = 15, 20\,\text{cm}$ and beam 1 for $\beta^* = 64, 100\,\text{cm}$) and IR 5 (beams 1 and 2 with $\beta^* = 15, 20\,\text{cm}$) produced by SixTrack simulation, used by BDSIM simulations in this thesis, are shown in this section.

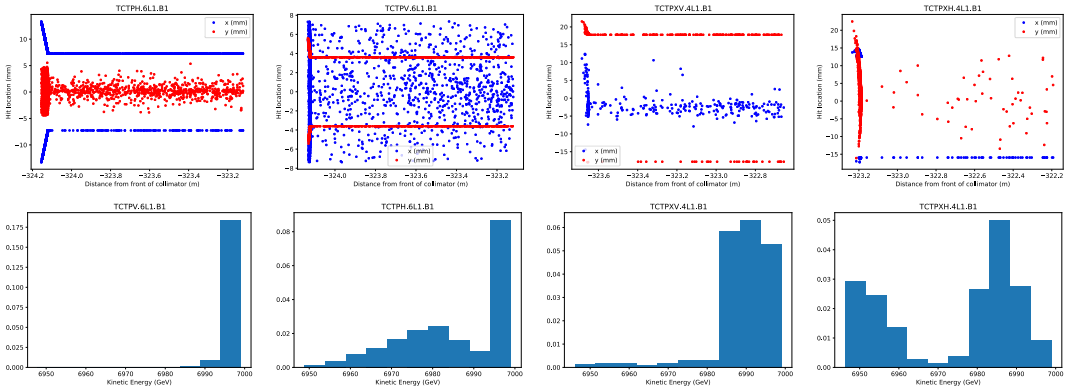

Figure A.1: Distribution of hits (top) and their kinetic energy (bottom) for TCTs in IP 1 for optics with $\beta^* = 15\,\text{cm}$, beam 1.

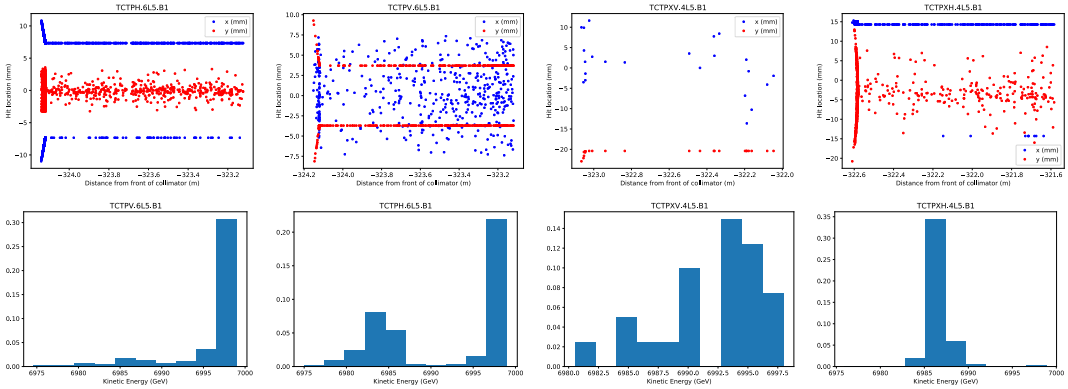

Figure A.2: Distribution of hits (top) and their kinetic energy (bottom) for TCTs in IP 5 for optics with $\beta^* = 15\,\text{cm}$, beam 1.

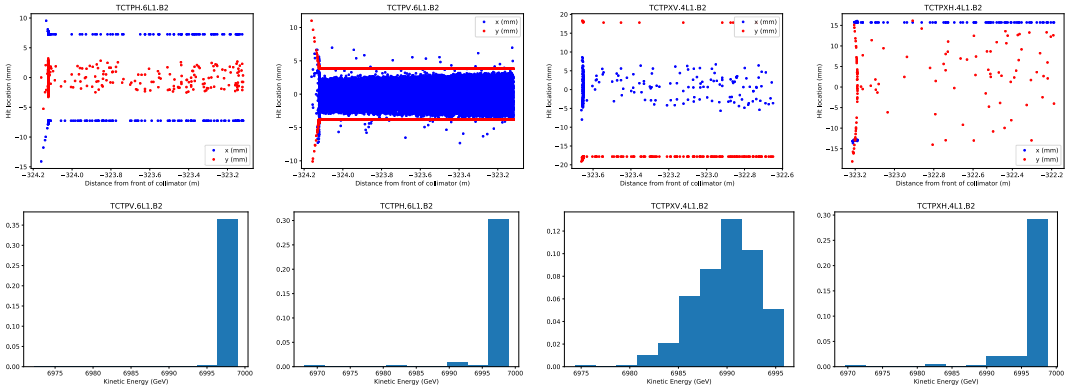

Figure A.3: Distribution of hits (top) and their kinetic energy (bottom) for TCTs in IP 1 for optics with $\beta^* = 15\,\text{cm}$, beam 2.

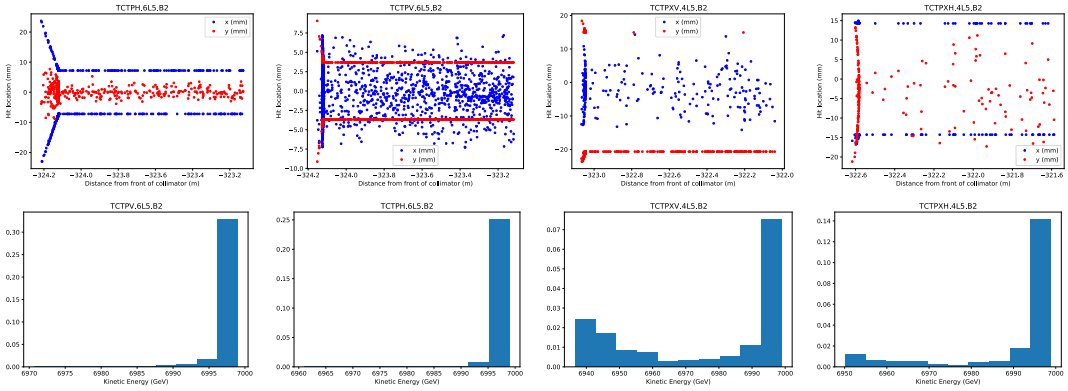

Figure A.4: Distribution of hits (top) and their kinetic energy (bottom) for TCTs in IP 5 for optics with $\beta^* = 15\,\text{cm}$, beam 2.

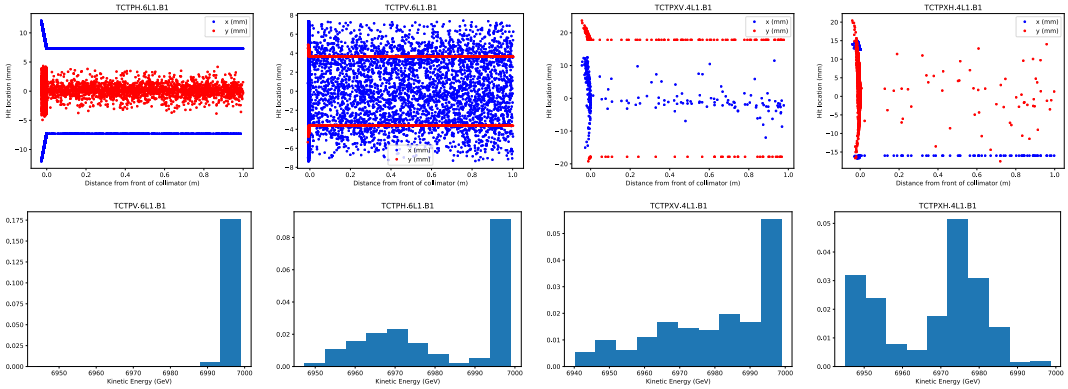

Figure A.5: Distribution of hits (top) and their kinetic energy (bottom) for TCTs in IP 1 for optics with $\beta^* = 20\,\text{cm}$, beam 1.

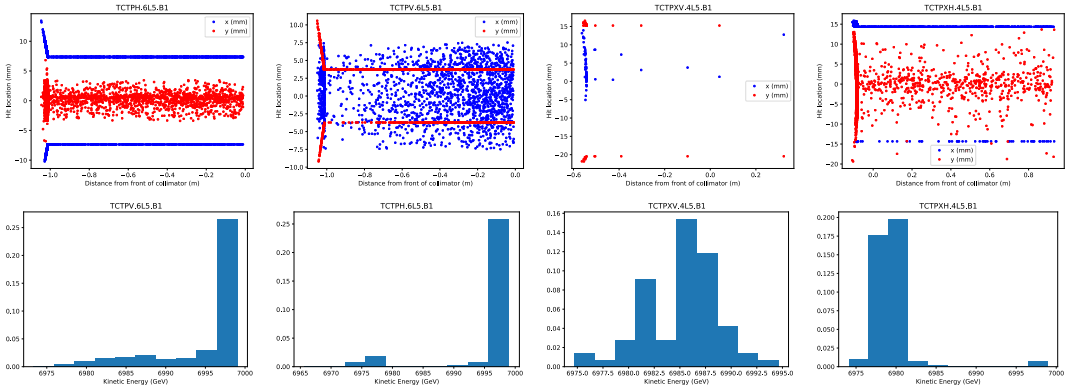

Figure A.6: Distribution of hits (top) and their kinetic energy (bottom) for TCTs in IP 5 for optics with $\beta^* = 20\,\text{cm}$, beam 1.

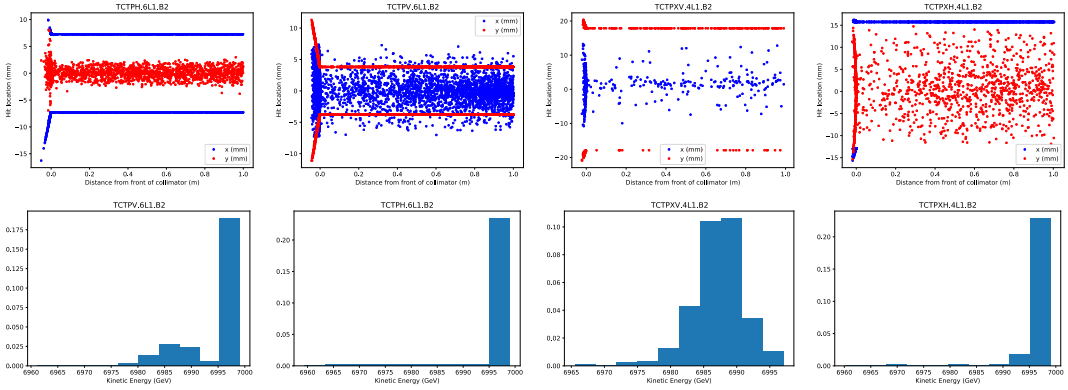

Figure A.7: Distribution of hits (top) and their kinetic energy (bottom) for TCTs in IP 1 for optics with $\beta^* = 20\,\text{cm}$, beam 2.

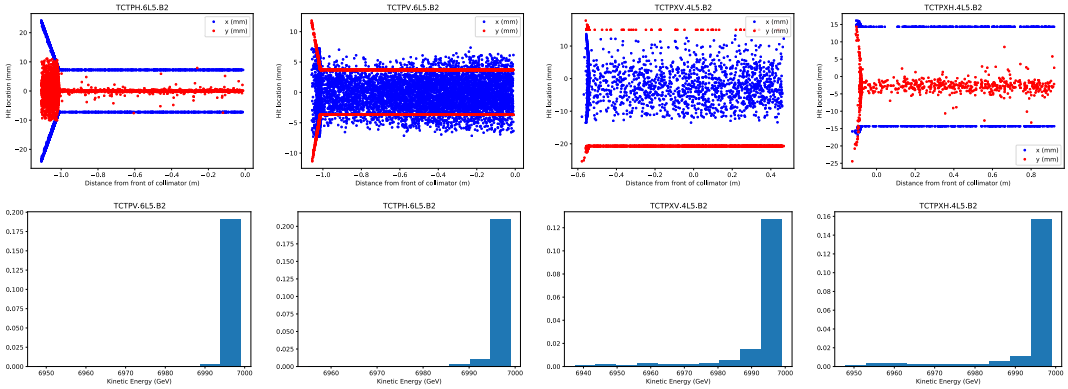

Figure A.8: Distribution of hits (top) and their kinetic energy (bottom) for TCTs in IP 5 for optics with $\beta^* = 20\,\text{cm}$, beam 2.

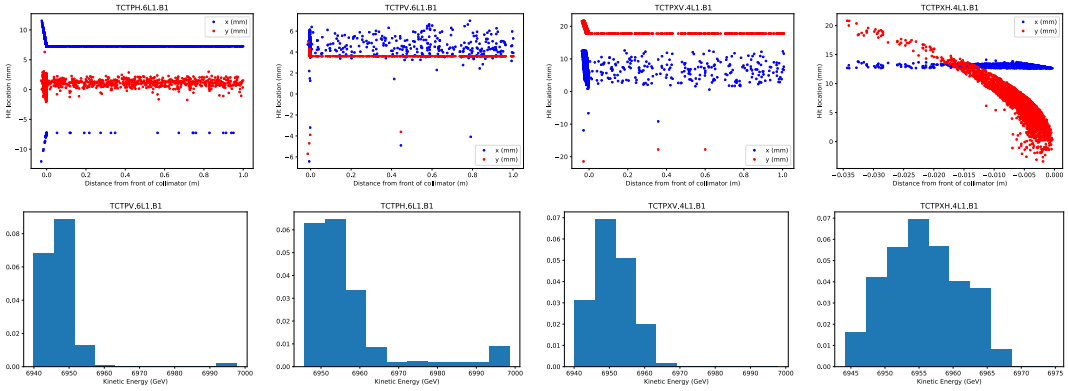

Figure A.9: Distribution of hits (top) and their kinetic energy (bottom) for TCTs for optics with $\beta^* = 64\,\text{cm}$.

Figure A.10: Distribution of hits (top) and their kinetic energy (bottom) for TCTs for optics with $\beta^* = 100\,\text{cm}$.

Bibliography

[1] R. Kwee-Hinzmann et al., *First Beam Background Simulation Studies at IR1 for High Luminosity LHC*, *Proc. 5th International Particle Accelerator Conference (IPAC'14), Dresden, Germany, June 15-20, 2014*, no. 5 in International Particle Accelerator Conference, (Geneva, Switzerland), pp. 1074–1077, JACoW, July, 2014, DOI.

[2] ATLAS Collaboration, *The ATLAS experiment at the CERN large hadron collider*, Journal of Instrumentation **3** (2008) S08003.

[3] R. Kwee-Hinzmann, G. Bregliozzi, R. Bruce, F. Cerutti, L. S. Esposito, S. Gibson et al., *Machine-induced Background Simulation Studies for LHC Run 1, Run 2 and HL-LHC*, CERN-ACC-2017-0025, CERN, Geneva, Apr, 2017, URL: https://cds.cern.ch/record/2261862.

[4] J. L. Feng, I. Galon, F. Kling and S. Trojanowski, *ForwArd Search ExpeRiment at the LHC*, Phys. Rev. D **97** (2018) 035001.

[5] J. D. Cockcroft and E. T. S. Walton, *Experiments with High Velocity Positive Ions. - (II) The Disintegration of Elements by High Velocity Protons*, Proceedings of the Royal Society A **137** (1932) 229.

[6] K. Codling, *Applications of synchrotron radiation (ultraviolet spectral light source)*, Reports on Progress in Physics **36** (1973) 541.

[7] N. Ban, P. Nissen, J. Hansen, P. B. Moore and T. A. Steitz, *The Complete Atomic Structure of the Large Ribosomal Subunit at 2.4 ÅResolution*, Science **289** (2000) 905 `https://www.science.org/doi/pdf/10.1126/science.289.5481.905`.

[8] O. Jäkel, *State of the art in hadron therapy*, AIP Conference Proceedings **958** (2007) 70 `https://aip.scitation.org/doi/pdf/10.1063/1.2825836`.

[9] M. G. Mustafa, *Quark–gluon plasma and heavy-ion phenomenology*, The European Physical Journal Special Topics **230** (2021) 603.

[10] Darsono, *Application of electron accelerator for flue gas treatment of coal power plant to support green technology*, IOP Conference Series: Earth and Environmental Science **456** (2020) 012002.

[11] R. J. Van de Graaff, K. T. Compton and L. C. Van Atta, *The Electrostatic Production of High Voltage for Nuclear Investigations*, Phys. Rev. **43** (1933) 149.

[12] J. D. Cockcroft and E. T. S. Walton, *Experiments with high velocity positive ions.—(I) Further developments in the method of obtaining high velocity positive ions*, Proceedings of the Royal Society A **136** (1932) 619.

[13] R. Wideröe, *Über ein neues prinzip zur herstellung hoher spannungen*, Archiv für Elektrotechnik **21** (1928) 387.

[14] R. B. Neal, ed., *The Stanford Two-Mile Accelerator*. W.A. Benjamin Inc., Nov, 1968.

[15] D. W. KERST, *Historical Development Of The Betatron*, Nature (1946) 90.

[16] E. O. Lawrence and M. S. Livingston, *The Production of High Speed Light Ions Without the Use of High Voltages*, Phys. Rev. **40** (1932) 19.

[17] O. Kamigaito, S. Arai, T. Dantsuka, M. Fujimaki, T. Fujinawa, H. Fujisawa et al., *Status of RIBF accelerators at RIKEN*, CYCLOTRONS 2010 - 19th International Conference on Cyclotrons and Their Applications (2010) 286.

[18] E. McMillan, *Synchro-Cyclotron*, UNITED STATES PATENT OFFICE (1952) 2615129.

[19] CERN Public Information Office, *CERN Synchro-cyclotron working at full energy*, Aug, 1957, URL: http://cds.cern.ch/record/839880/files/CM-P00053829.pdf.

[20] V. I. Veksler, *A new method of accelerating relativistic particles*, Comptes Rendus de l'Académie des Sciences de l'URSS **48** (1944) 346.

[21] L. Evans and P. Bryant, *LHC Machine*, Journal of Instrumentation **3** (2008) S08001.

[22] CERN website, *Radiofrequency cavities*, Sep, 2012, URL: https://cds.cern.ch/record/1997424.

[23] O. S. Bruning, P. Collier, P. Lebrun, S. Myers, R. Ostojic, J. Poole et al., *LHC Design Report Vol.1: The LHC Main Ring*, CERN-2004-003-V-1.

[24] P. Jenni and T. Virdee, *The Discovery of the Higgs Boson at the LHC*, pp. 263–309. Springer, 09, 2020. http://dx.doi.org/10.1007/978-3-030-38207-0_6.

[25] A. Filipčič, *ATLAS Distributed Computing Experience and Performance During the LHC Run-2*, Journal of Physics: Conference Series **898** (2017) 052015.

[26] LHC Study Group, *The Large Hadron Collider: conceptual design*, CERN-AC-95-05-LHC.

[27] G. Apollinari, I. Béjar Alonso, O. Brüning, P. Fessia, M. Lamont, L. Rossi et al., *High-Luminosity Large Hadron Collider (HL-LHC): Technical Design Report V. 0.1*, CERN Yellow Reports: Monographs. CERN, Geneva, 2017.

[28] B. Schmidt, *The High-Luminosity upgrade of the LHC: Physics and Technology Challenges for the Accelerator and the Experiments*, Journal of Physics: Conference Series **706** (2016) 022002.

[29] M. Benedikt, M. Capeans Garrido, F. Cerutti, B. Goddard, J. Gutleber, J. M. Jimenez et al., *FCC-hh: The Hadron Collider: Future Circular Collider Conceptual Design Report Volume 3. Future Circular Collider*, CERN-ACC-2018-0058.

[30] F. Zimmermann, M. Benedikt, M. Capeans Garrido, F. Cerutti, B. Goddard, J. Gutleber et al., *HE-LHC: The High-Energy Large Hadron Collider: Future Circular Collider Conceptual Design Report Volume 4. Future Circular Collider*, CERN-ACC-2018-0059.

[31] ATLAS experiment, *ATLAS detector*, 2022, URL: https://atlas.cern/.

[32] ATLAS Collaboration, *ATLAS Insertable B-Layer Technical Design Report*, CERN-LHCC-2010-013, ATLAS-TDR-19.

[33] F. Kling and S. Trojanowski, *Heavy neutral leptons at faser*, Phys. Rev. D **97** (2018) 095016.

[34] J. L. Feng, I. Galon, F. Kling and S. Trojanowski, *Axionlike particles at faser: The lhc as a photon beam dump*, Phys. Rev. D **98** (2018) 055021.

[35] J. Wenninger and R. Schmidt, *Protection against Accidental Beam Losses at the LHC*, LHC-Project-Report-820, CERN-LHC-Project-Report-820.

[36] B. Dehning, E. Effinger, J. Emery, G. Ferioli, G. Guaglio, E. B. Holzer et al., *The LHC Beam Loss Measurement System*, LHC-PROJECT-Report-1025, CERN-LHC-PROJECT-Report-1025.

[37] G. Azzopardi, B. Salvachua and G. Valentino, *Data-driven cross-talk modeling of beam losses in LHC collimators*, Phys. Rev. Accel. Beams **22** (2019) 083002. 11 p 8.

[38] S. Redaelli, *LHC Collimation Project*, 2013, URL: http://lhc-collimation-project.web.cern.ch/.

[39] M. Varasteh, R. Bruce, F. Cerutti, M. Crouch and F. Zimmermann, *Impact of betatron collimation losses in the High-Energy Large Hadron Collider*, Phys. Rev. Accel. Beams **24** (2021) 041601.

[40] C. Boscolo Meneguolo, A. Abramov, R. Bruce, F. Cerutti, M. Ferro-Luzzi, M. Giovannozzi et al., *Study of beam-gas interactions at the LHC for the Physics Beyond Colliders fixed-target study*, CERN-ACC-2019-088, CERN-PBC-CONF-2021-018.

[41] K. Eggert, K. Honkavaara and A. Morsch, *Luminosity considerations for the LHC*, CERN-AT-94-04-DI, CERN-LHC-Note-263, LHC-NOTE-263.

[42] M. Lamont, *Estimates of Annual Proton Doses in the LHC*, LHC-Project-Note-375, CERN-LHC-Project-Note-375.

[43] L. Nevay, S. Boogert, J. Snuverink, A. Abramov, L. Deacon, H. Garcia-Morales et al., *BDSIM: An accelerator tracking code with particle–matter interactions*, Computer Physics Communications **252** (2020) 107200.

[44] GEANT4, *GEANT4–a simulation toolkit*, Nucl. Instrum. Meth. A **506** (2003) 250 SLAC-PUB-9350, FERMILAB-PUB-03-339, CERN-IT-2002-003.

[45] W. Herr and F. Schmidt, *A MAD-X Primer*, CERN-AB-2004-027-ABP.

[46] C. Runge, *Über die numerische auflösung von differentialgleichungen*, Mathematische Annalen **46** (1895) 167.

[47] F. Rademakers, P. Canal, A. Naumann, O. Couet, L. Moneta, V. Vassilev et al., *ROOT - An Object Oriented Data Analysis Framework: First release of the v6-16 series.*, Feb., 2019, URL: https://doi.org/10.5281/zenodo.2557526. 10.5281/zenodo.2557526.

[48] C. Ahdida, D. Bozzato, D. Calzolari, F. Cerutti, N. Charitonidis, A. Cimmino et al., *New Capabilities of the FLUKA Multi-Purpose Code*, Frontiers in Physics **9** (2022) .

[49] G. Battistoni, T. Boehlen, F. Cerutti, P. Chin, L. Esposito, A. F. A. Fassò et al., *Overview of the FLUKA code*, Annals of Nuclear Energy **82** (2015) .

[50] V. Vlachoudis, *Flair: A powerful but user friendly graphical interface for fluka*, 04, 2009.

[51] R. D. Maria et al., *SixTrack Version 5: Status and New Developments*, *Proc. 10th International Particle Accelerator Conference (IPAC'19), Melbourne, Australia, 19-24 May 2019*, no. 10 in International Particle Accelerator Conference, (Geneva, Switzerland), pp. 3200–3203, JACoW Publishing, Jun., 2019, DOI.

[52] R. Ulrich, T. Pierog and C. Baus, *Cosmic Ray Monte Carlo Package, CRMC*, Aug., 2021, URL: https://doi.org/10.5281/zenodo.5270381. 10.5281/zenodo.5270381.

[53] F. Riehn, R. Engel, A. Fedynitch, T. K. Gaisser and T. Stanev, *Hadronic interaction model sibyll 2.3d and extensive air showers*, Phys. Rev. D **102** (2020) 063002.

[54] E.-J. Ahn, R. Engel, T. K. Gaisser, P. Lipari and T. Stanev, *Cosmic ray interaction event generator SIBYLL 2.1*, Phys. Rev. D **80** (2009) 094003.

[55] T. Pierog, I. Karpenko, J. M. Katzy, E. Yatsenko and K. Werner, *EPOS LHC: Test of collective hadronization with data measured at the CERN Large Hadron Collider*, Phys. Rev. C **92** (2015) 034906.

[56] S. Playfer, The LHCb Collaboration, M. Needham, F. Muheim, P. Clarke, Y. Xie et al., *Measurement of the forward energy flow in pp collisions at* $\sqrt{s} = 7\ TeV$, European Physical Journal C **C73** (2013) 2421.

[57] T. Sjöstrand, S. Mrenna and P. Skands, *PYTHIA 6.4 physics and manual*, Journal of High Energy Physics **2006** (2006) 026.

[58] S. Boogert et al., *Pyg4ometry : A Tool to Create Geometries for Geant4, BDSIM, G4Beamline and FLUKA for Particle Loss and Energy Deposit Studies*, *Proc. 10th International Particle Accelerator Conference (IPAC'19), Melbourne, Australia, 19-24 May 2019*, no. 10 in International Particle Accelerator Conference, (Geneva, Switzerland), pp. 3244–3247, JACoW Publishing, Jun., 2019, DOI.

[59] W. H. Bell, *Beam Background Generator*, 2010, URL: http://bbgen.web.cern.ch/bbgen/.

[60] E. J. Fern, V. Di Murro, K. Soga, Z. Li, L. Scibile and J. A. Osborne, *Geotechnical characterisation of a weak sedimentary rock mass at CERN, Geneva*, Tunnelling and Underground Space Technology **77** (2018) 249.

[61] ATLAS Collaboration, *Comparison between simulated and observed LHC beam backgrounds in the ATLAS experiment at* $E_{\text{beam}} = 4$ *TeV*, JINST **13** (2018) P12006. 44 p CERN-EP-2018-240, arXiv: 1810.04450.

[62] G. Aad et al., *Beam-induced and cosmic-ray backgrounds observed in the ATLAS detector during the LHC 2012 proton-proton running period*, Journal of Instrumentation **11** (2016) P05013.

[63] S. Baranov, M. Bosman, I. Dawson, V. Hedberg, A. Nisati and M. Shupe, *Estimation of Radiation Background, Impact on Detectors, Activation and Shielding Optimization in ATLAS*, ATL-GEN-2005-001, ATL-COM-GEN-2005-001, CERN-ATL-GEN-2005-001.

[64] ATLAS Collaboration, "Non-Collision Background Public Results: Public Plots approved in Spring of 2017." URL: twiki.cern.ch/twiki/bin/view/AtlasPublic/NonCollisionBackgroundPublicResults.

[65] ATLAS Collaboration, *Characterisation and mitigation of beam-induced backgrounds observed in the ATLAS detector during the 2011 proton-proton run*, Journal of Instrumentation **8** (2013) P07004.

[66] M. Varasteh, R. Bruce, F. Cerutti, M. Crouch and F. Zimmermann, *Impact of betatron collimation losses in the High-Energy Large Hadron Collider*, Phys. Rev. Accel. Beams **24** (2021) 041601.

[67] M. Patecki, A. Mereghetti, D. Mirarchi and S. Redaelli, *Conceptual design of an off-momentum collimation system in the CERN Super Proton Synchrotron for High-Luminosity Large Hadron Collider proton beams*, Phys. Rev. Accel. Beams **24** (2021) 093002.

[68] R. Kwee-Hinzmann, R. Bruce, F. Cerutti, L. Esposito, S. Gibson and A. Lechner, *Beam Induced Background Simulation Studies at IR1 with New High Luminosity LHC Layout*, *Proc. 6th International Particle Accelerator Conference (IPAC'15), Richmond, VA, USA, May 3-8, 2015*, no. 6 in International Particle Accelerator Conference, (Geneva, Switzerland), pp. 2184–2187, JACoW, June, 2015, DOI.

[69] ATLAS Collaboration, *The Phase-2 ATLAS ITk Pixel Upgrade*, ATL-ITK-PROC-2018-003.

[70] A. Collaboration, *Technical Design Report: A High-Granularity Timing Detector for the ATLAS Phase-II Upgrade*, CERN-LHCC-2020-007, ATLAS-TDR-031.

[71] ATLAS Collaboration, *The Run-2 ATLAS Trigger System: Design, Performance and Plan*, ATL-DAQ-PROC-2016-039.

[72] V. Drollinger, *Simulation of Beam Halo and Cosmic Muons*, CMS-NOTE-2005-012.

[73] T. Kittelmann, V. Tsulaia, J. Boudreau and E. Moyse, *The virtual point 1 event display for the atlas experiment*, Journal of Physics: Conference Series **219** (2010) 032012.

[74] FASER, *Technical Proposal for FASER: ForwArd Search ExpeRiment at the LHC*, arXiv : `1812.09139[physics.ins-det]` CERN-LHCC-2018-036, LHCC-P-013, UCI-TR-2018-22, KYUSHU-RCAPP-2018-07, arXiv: `1812.09139[physics.ins-det]`.